UNIVERSITY OF CALIFORNIA,
IRVINE

Characterization of Energy Dissipation Mechanisms in Building Structures

DISSERTATION

submitted in partial satisfaction of the requirements
for the degree of

DOCTOR OF PHILOSOPHY

in Civil and Environmental Engineering

by

Yijun Xiang

Dissertation Committee:
Associate Professor Farzin Zareian, Chair
Adjunct Professor Farzad Naeim
Associate Professor Anne Lemnitzer

2020

DEDICATION

To

my parents and friends

TABLE OF CONTENTS

LIST OF FIGURES

LIST OF TABLES

ACKNOWLEDGEMENTS

I would like to express the deepest appreciation to my committee chair, Professor Farzin Zareian, for continuously educating me and supporting me regarding research and scholarship during my Ph.D. at UC Irvine. Without his wisdom, persistent guidance, and supervision, this dissertation could not have been accomplished. I would like to express my gratitude to my committee members, Prof. Farzad Naeim for his keen insight and rich experience that has helped me throughout my research work, and Prof. Anne Lemnitzer for her consistent support, strong mentorship, encouragement and advice during my Ph.D. studies.

I would like to extend my appreciation to my former and current colleagues, including Dr. Bahareh Mobasher, Dr. Peng Zhong, Angie Harris, Marta De Bortoli, Shayan Sheikhakbari, Shima Ebrahimi, Dr. Pablo Torres, Dr. Huda Munjy, Preetish Kakoty. To Rachelle Habchi and Jawad Fayaz, I thank you for inspiring me and motivating me during my Ph.D. journey.

Finally, I would like to thank my family from the bottom of my heart for all the support throughout my educational journey. Thank you.

CURRICULUM VITAE

Yijun Xiang

EDUCATION

2020 University of California, Irvine, CA

Doctor of Philosophy (Ph.D), Earthquake/Structural Engineering

2013 Southwest Jiaotong University, China

Bachelor's in Engineering, Civil/Structural Engineering

RELEVANT EXPERIENCE

Teaching Assistant at University of California, Irvine:

- CEE155: Steel Design, September 2016 – December 2016, 1 discussion session weekly
- CEE150: Mechanics of Materials, September 2017 – December 2017 & September 2019 – December 2019, 4 discussion sessions weekly
- CEE150L: Mechanics of Materials Laboratory Instructor, September 2018 – December 2018, 8 laboratory sessions weekly
- CEE151B: Timber Design, January 2019 – March 2019, 1 discussion session weekly

---

PUBLICATIONS

Journal Articles:

- Yijun Xiang, Farzad Naeim, and Farzin Zareian. "Evaluation of Natural Periods and Modal Damping Ratios for Seismic Design of Building Structure." Earthquake Spectra, Accepted, DOI: 10.1177/8755293019900776
- Yijun Xiang, Farzad Naeim, and Farzin Zareian. "Critical Assessment of Accidental Torsion in Buildings with Symmetric Plans.", Earthquake Spectra, Second round of review. (under review)
- Jawad Fayaz, Yijun Xiang, and Farzin Zareian. "Probabilistic Performance Assessment of Ordinary Bridges Under A Sequence of Seismic Excitations." (in progress)
- Jawad Fayaz, Yijun Xiang, and Farzin Zareian. "Generalized Ground Motion Prediction Model (GGMPM) Using Hybrid Recurrent Neural Networks.", Earthquake Engineering & Structural Dynamics. (under review)
- Yijun Xiang, and Farzin Zareian. "A Damping Element Model for Energy Dissipation Characterization in Building Structures." (in progress/preparation)

Conference Proceedings:

- Yijun Xiang, and Farzin Zareian. "A Damping Element Model for Energy Dissipation Characterization in Building Structures." 17th World Conference on Earthquake Engineering (17WCEE), Sendai, Japan, September 2020.
- Jawad Fayaz, Yijun Xiang, and Farzin Zareian. "Ground Motion Spectral using Recurrent Neural Networks (RNN)." 17th World Conference on Earthquake Engineering (17WCEE), Sendai, Japan, September 2020.
- Jawad Fayaz, Yijun Xiang, and Farzin Zareian. "Performance Assessment of Bridges Under A Sequence of Seismic Excitations." Computational Methods in Structural Dynamics & Earthquake Engineering (COMPDYN 2019), Crete Island, Greece, June 2019.
- Yijun Xiang, and Farzin Zareian. "A Damping Element Model for Energy Dissipation Characterization in Building Structures." 11th National Conference on Earthquake Engineering (11NCEE), Los Angeles, California, June 2018.
- Yijun Xiang, Farzad Naeim, and Farzin Zareian. "Assessment of ASCE 7 Accidental Torsion Provisions." Annual Meeting of Los Angeles Tall Buildings Structural Design Council (LATBSDC), Los Angeles, California, May 2018.
- Yijun Xiang, Angie Harris, Farzad Naeim, and Farzin Zareian. "Identification and Validation of Natural Periods and Modal Damping Ratios for Seismic Design and Building Code." Annual Meeting of Los Angeles Tall Buildings Structural Design Council (LATBSDC), Los Angeles, California, May 2017.

Technical Reports:

- "Validation of Caltrans Ordinary Bridge Modeling Approach using Bayesian State and Parameter Estimation Method." California Strong Motion Instrumentation Program (CSMIP) Agreement No. 1018-568 (2019)
- "Critical Assessment of Code Torsional Provisions Using CSMIP Database of Instrumented Buildings." California Strong Motion Instrumentation Program (CSMIP) Agreement No. 1016-986 (2018)
- "Identification and Validation of Natural Periods and Modal Damping Ratios for Steel and Reinforced Concrete Buildings in California." California Strong Motion Instrumentation Program (CSMIP) Agreement No. 1016-986 (2017)

ABSTRACT OF THE DISSERTATION

Characterization of Energy Dissipation Mechanisms in Building Structures

by

Yijun Xiang

Doctor of Philosophy in Civil and Environmental Engineering

University of California, Irvine, 2020

Professor Farzin Zareian, Chair

This research intends to contribute to a deeper understanding and more accurate characterization of structural damping using real-life building and earthquake data and provide suggestions and updates regarding the design and modeling of structures. The accurate characterization and modeling of structural damping have been overlooked in the current methods for estimation of response of structural systems, which traditionally utilizes linear viscous damping to model the structures exposed to dynamic excitation. Rayleigh damping (the most used damping model) provides convenience in structure modeling and design. However, it leads to unconservative response estimation, especially in nonlinear time history analysis with stiffness softening of the structural components. Given that a realistic structural damping model exhibits both velocity-dependent and amplitude-dependent energy dissipation characteristics, this dissertation focuses on the structural damping behavior and energy dissipation mechanism, which is a combination of various sources such as linear viscous damping and amplitude-dependent friction-based damping. The significant sources of damping present in a structural system, such as slippage of joints, breakage of nonstructural elements and friction between structural and nonstructural components, are accounted for in the proposed damping element model. A generic

building structure model which can be widely used for a large database of buildings with various height, dimension and material is built in OpenSees with damping elements implemented. Optimization methods are adopted to match the response of the generic model with that from the California Strong Motion Instrumentation Program (CSMIP) instrumented buildings subject to the same earthquake ground motion excitations. The damping element properties, such as the viscous damping coefficient, the stiffness of the frictional damper, and the yielding point of the frictional damper, are calibrated for each selected building subject to multiple earthquake excitations. Statistical analysis is conducted to further study the effect of ground motion intensity, building height, and building dimension on these damping element parameters.

CHAPTER 1: INTRODUCTION

1.1 PROBLEM STATEMENT

Unlike properties such as mass and stiffness, a structure's damping cannot be easily estimated (or measured) and modeled. The considerable uncertainty in estimation and damping modeling can be traced back to the complex nature of energy dissipation mechanisms in structures. This research is commenced to shed light on this important aspect for accurate building seismic response assessment.

Structural damping accounts for the energy dissipation mechanisms in building and, plays an important role in assessing its performance. Represented usually in form of a damping ratio, it has a direct effect on the results of response history analysis; having a deep understanding of the physical source of energy dissipation can assist in accurately modeling the damping phenomena. Except for seismic design methods that are explicitly based on equivalent linearization, such as the Capacity Spectrum Method contained in ATC-40 (Applied Technology Council, 1996), where the equivalent damping accounts for the effects of hysteretic and material damping, or the Direct Displacement-Based Seismic Design, where the effective viscous damping is defined as a function of displacement ductility demand (Priestly, Calvi and Kowalski, 2007), the use of equivalent damping in seismic design has been at best ambiguous and not well defined. This is a major issue for seismic design of new buildings and retrofit of existing structures alike because no matter what design method is implemented, an estimate of equivalent modal viscous damping is necessary for the structural design process. In the code-based structural design approach, the reduction in design forces attributable to expected nonlinear behavior of the structure and the structural system's assumed ductility is primarily considered using the Response Modification Coefficient (i.e., *R*). In modern performance-based design (PBD), which relies on explicit nonlinear analyses of structures, the energy dissipated in the structure due to the nonlinear hysteretic behavior of structural components is explicitly modeled. In the PBD context, the term structural damping refers not to the energy dissipated in the structure due to its nonlinear response but refers to sources of energy dissipation that are not explicitly considered in the structural model. There is an extensive body of research currently available on the characterization and modeling of structural damping. A detailed literature review is presented in Spence & Kareem (2014) and ATC (2010).

Current practical purposes (ASCE 2010, ASCE 2017, ATC 2010) entail structural damping being modeled as equivalent linear viscous damping. Although conventionally and widely used to represent the energy dissipated in the structure during seismic excitations, this implementation of linear viscous damping is mainly due to the modeling convenience where damping is expressed as a percentage of the critical damping in modes of vibration in the structural systems, for instance, Rayleigh Damping makes use of the damping ratio in two modes of vibrations, and Caughey Damping deals with higher modes of vibrations. Therefore, this approach is nothing but an expedient by which the system governed by the equation of motion (a second-order differential equation) can be solved.

It is generally recommended to use an equivalent viscous damping ratio between 2% and 5% for the first vibration mode. Efforts have been made to provide guidelines of proper damping estimations; for example, The Minimum Design Loads for Buildings and Other Structures (ASCE/SEI 7-10, 7-16) requires the use of 5% damping; FEMA P-58-1 requires the use of 1% to 5% of the critical damping for the predominant modes of vibration; the Los Angeles Tall Buildings Structural Design Council (LATBSDC) and Tall Building Initiative Guidelines suggest that the modal damping should not exceed 2.5% of the critical damping for predominant modes. There are also guidelines for appropriate assignment of damping ratio depending on different building construction materials, building types and building heights. For example, in most reinforced concrete or steel structures, the damping ratio is limited to be 5%, while building structures of wood frames typically use a damping ratio as high as 10%. Tall buildings usually adopt a lesser damping ratio, and the value can be as low as 2%. Although a seemingly constant damping ratio is usually adopted in seismic design and modeling, the use of equivalent viscous damping is by no means well-defined, and the inherent uncertainty of damping is evident (Bernal 2012).

Several factors that control the behavior of energy dissipation in structures need to be considered explicitly in the modeling of structural damping, including building heights, building materials, type of lateral force resisting system, nonstructural components such as exterior cladding and interior partition walls, effects of soil-structure interaction, and intensity measures such as the amplitude of ground motion excitations (Jeary 1997). Damping is a combination of various physical phenomena following distinct physical laws that has many sources of complexity, including material damping that considers molecular interaction and is velocity dependent, Coulomb friction between structural members and connections which is amplitude-dependent, etc. The complex nature of damping makes it especially complicated to be identified and almost impossible to develop a damping model that refers to all these sources.

Even though it is widely understood that structural damping is of high complexity, in practice, modeling of structural damping is restricted to equivalent viscous damping forces, which are assumed to be proportional to velocities but not dependent on the amplitude of excitation. This modeling approach lacks an explainable physical meaning. Rayleigh damping (the most commonly used method to model viscous damping) is proven to be unrealistic and unconservative, producing inaccurate estimates of displacements and internal forces in members. For example, it could lead to an underestimation of peak displacement as well as an overestimation of internal forces in the elements, especially in nonlinear analysis with stiffness softening (Bernal 1994, Zareian and Medina 2010, Hall 2005). These inaccurate estimates of internal forces are related to responses in which static equilibrium is not satisfied.

Experimental data shows that under certain circumstances, damping is primarily a function of displacement rather than velocity. Several studies have shown amplitude dependency of damping. A 'Stick-Friction' model is introduced by the concept of stick-slip elements, where the nonlinear increase of energy dissipation is correlated to the imperfections of material (Wyatt 1977). It was found that at a low amplitude plateau, damping remains constant and as amplitude increases in the nonlinear region, the imperfections in the material are mobilized when the structure is excited, dissipating energy and increasing the structural damping. Other studies subsequently elaborated on the 'imperfection theory,' provided a myriad of equations for damping expressed as functions of amplitude after examining response data of seismic excitations (Davenport and Hill-Caroll 1986, Jeary 1997, Fang et al. 1999, Li et al. 2000). These researches demonstrated that damping increases with amplitude since more imperfections are activated until it arrives at the high amplitude plateau where all material imperfections are activated so that damping becomes eventually constant. In contrast, some researches have shown that the increase of damping occurs before the amplitude corresponding to the critical tip ratio is reached. This idea corresponds to the assumption that as the amplitude of excitation increases, friction between members and connections builds up until it reaches the critical point, where all contact surfaces have eventually slipped, and the friction is saturated. Total friction force remains constant and the increase of amplitude causes a decrease of damping. The critical tip ratio from where damping begins to decrease is introduced in an amplitude-dependent damping model by Tamura (2008). Others have studied the relationship between damping and natural periods. An analysis of building periods and damping ratios obtained from full-scale data of buildings in Japan (137 steel-framed buildings, 25 reinforced concrete buildings, and 43 steel-framed reinforced concrete buildings) concludes that damping is amplitude-dependent, increasing with mode number, and the first mode damping ratio in the small amplitude region increases linearly with natural frequency and the amplitude of vibration (Stake 2003). Similarly, a pattern of increasing damping ratios with natural periods is observed (Bernal 2012), and the increment of modal damping ratios depends on the building type, whether it is dominated by shear or flexural behavior. This theory explores damping and its dependence on the dominant building response characteristics. Bentz and Kijewski-Correa (2008) discussed the prediction of damping based on the dominance of structural systems deformation mechanisms, shear or flexural action. Shear deformation takes precedence in frames where they deform from its generally square nature. Flexural deformation usually occurs in shear wall systems and other systems where the structure behaves similarly to a continuous cantilever and the aspect ratio of the structure aids in the determination of the level of cantilever action. In the research conducted, it was determined that damping values are more scattered for intermediate systems (between the shear and flexural behavior). As systems become further dominated by flexural mode of vibration, damping values decrease.

Given the inappropriateness of the use of viscous damping and the evidence of amplitude-dependent damping from data-driven research studies, frictional damping is taken into account to avoid false structural responses. This dissertation aims to develop a nonstructural damping element model to investigate the energy dissipation mechanisms in structures. It is postulated that those nonstructural damping elements implemented in the model are able to account for three energy dissipation mechanisms: velocity-dependent energy dissipation in the form of viscous damping, displacement dependent energy dissipation in the form of frictions between element surfaces, and displacement dependent energy dissipation by the breakage of the elements. With this assumption, an increase in displacement amplitude leads to higher energy dissipation (i.e., larger equivalent viscous damping) and simultaneously a reduction in natural frequency due to stiffness loss in nonstructural elements. The amplitude-dependent energy dissipation model and the amplitude-dependent stiffness reduction model where damping ratio and natural frequency are functions of displacement amplitudes are tested by nonlinear regression analysis after System Identification Techniques are applied to recorded earthquake ground motions and floor accelerations from (CSMIP) and dynamic properties at different levels of amplitude are obtained. Therefore, despite these implications of misuse of viscous damping, the benefits of using a simple, applied, and practical equivalent viscous damping in structural systems seem to outweigh its shortcomings as it provides an overall estimate of equivalent damping and thus serves as one of the essential tasks of this research. Nonlinear regression analysis provides an estimation of a set of parameters from hysteretic models of the nonstructural elements for each mode. Finite element models with story-based nonstructural elements are built in OpenSees (McKenna et al. 2010) and gone through several updating iterations until finite element model results return to similar modal parameters estimated from the statistical regression analysis. The result provides estimations for distributions of slip amplitude, frictional force, and cyclic deteriorations from the hysteretic model of the nonstructural damping elements in each individual building as well as for various groups of buildings with the same building materials, building occupancies, and building lateral force resisting systems. The research is in contrast with previous efforts in that it aims to use the vast data available from the network of CSMIP instrumented buildings to identify meaningful and practical structural period and damping coefficients to improve both the seismic design provisions of the building codes and the practice of performance-based design and retrofit of structures.

The prerequisite to perform an experimental estimation of damping is the collection of full-scale data. After the data has been collected, an appropriate damping estimation technique can be applied. The database used in this study is obtained from the California Strong Motion Instrumentation Program (CSMIP), where the input ground motion excitation as well as the output building structural response was measured during the seismic event. Appropriate System Identification techniques are applied to evaluate modal properties, including natural periods and damping ratios. The problem is dissected in two steps: one is to estimate the modal properties including nature period and modal damping values through the methodology of linear system control, which utilizes time-series modeling of the recorded input and output accelerations; second is to physically model the building structure, and obtain optimal damping values by minimization of an objective function giving a measure of the difference between the analytical response when ground motion excitation is applied to the physical building model and the recorded responses obtained from the sensor locations.

The data used in this dissertation from the CSMIP database of instrumented buildings contains structural records from more than 166 events (including mainshocks and aftershocks) ranging in date from 1979 to 2019. Due to the recent move to digital recording, the data is skewed towards more recent earthquakes resulting in a sharp increase in the number of records obtained from more recent events. Ninety-four buildings, with a total of 1045 distinct seismic event and building direction records, are selected from the CSMIP database to identify modal quantities (i.e., natural periods and equivalent viscous damping ratios). The selected buildings include steel and reinforced concrete moment resisting frames (i.e., SMRF, and RCMRF), reinforced concrete walls

(RCW), concentrically braced frames (CBF), eccentrically braced frames (EBF), masonry walls (MAW), precast concrete walls (PCW), reinforced concrete tilt-up bearing walls (RCTUW), unreinforced masonry (URM) and WOOD. Variation of modal quantities to structural system types, building height, the amplitude of excitation, and system identification technique is studied. Among the 94 buildings used in this study, there are 25 SMRF, 11 RCMRF, 30 RCW, 11 CBF, 3 EBF, 6 MAW, 3 PCW, 2 RCTUW, 1 URM, 2 WOOD buildings with 214, 123, 380, 145, 34, 74, 40, 9, 8 and 18 distinct seismic event and building direction records.

1.2 OBJECTIVES OF RESEARCH

This study fills the gap in our knowledge for proper modeling of damping in building structures. The objectives of this study are to:

1. Present a detailed background of the current state-of-art on damping modeling in building structures.
2. Quantify structural damping in the form of a set of meaningful and rational equivalent damping ratios using a novel system identification method combing time and frequency domain methods.
3. Develop simplified and practical equations based on structural system types, building height and other factors that may prove to be significant such as ground motion intensity measures for damping ratios of buildings.
4. Propose a novel damping element model in building structures using generic building frames to effectively capture the structure's response to ground motion excitations.
5. Calibrate the damping element models to match the time history recordings of the real-life structures with different building height, dimension, material

6. Summarize the findings by statistical analysis, suggest simplified and practical equations to estimate damping elements' properties in building structures useful for practicing engineers and design code developers.

1.3 DISSERTATION OUTLINE

Chapter 2 proposes a comprehensive system identification technique that combines time domain and frequency domain modal identification methods. The database of this section is collected from the California Strong Motion Instrumentation Program (CSMIP), where building structures located in California are instrumented with sensors that measure the response of the structures subject to earthquake ground motion excitations. The input and output of the system are processed and utilized to identify the model properties of the building structures by time history signals. Modal properties of 80 buildings with different construction materials are identified and prediction of modal properties is suggested via a comprehensive statistical analysis including model selection, feature deduction, nonlinear regression, etc.

Chapter 3 extends the methodology of system identification and signal processing adopted in Chapter 2 from 2-dimensional frames to 3-dimensional building models. This chapter also explores other uses of the CSMIP database, such as validation of the effects of accidental torsion in building structures. Analytical rigid diaphragm building models with uncertainty in stiffness of the vertical lateral load resisting systems are built to study the amplification in displacement at each story level. Important factors controlling the performance of building structures such as building number of stories, building plan aspect ratio, the ratio of fundamental translational period to fundamental rotational period, hazard level and building location are investigated as random variables. Building information (height, dimension, etc.) and response subject to ground motions obtained from the CSMIP database are used to estimate the displacement amplification as well as the controlling factors. The effect of accidental torsion is finally compared with that of analytical results.

Chapter 4 describes a damping element model implemented on a continuum model where a flexural cantilever beam is connected to a shear cantilever beam. The damper between every two adjacent stories is modeled by zero-length springs using paralleled materials of linear viscous damper and coulomb frictional damper instead of assigning modal damping proportional to the mass and the stiffness matrices in a traditional way. This is a generic building model suitable for a wide range of real-life building structures with different building construction materials, different building lateral force resisting systems, different building heights and dimensions in the CSMIP database. Optimization methods are applied to match the analytical response from the generic model and the recorded response from the CSMIP database. Equations are suggested to predict the damping element via hierarchical mixed-effect statistical models.

Chapter 5 summarizes the ultimate findings of this dissertation. The limitation of this dissertation is discussed. Recommendations for further study is provided.

1.4 MATHEMATICAL BACKGROUND AND METHOD

1.4.1 System Realization Using Information Matrix (SRIM)

The SRIM method utilizes the information regarding the correlation of the input, output, state vectors determined through the state-space model in order to determine the system matrices A, B, C, and D. From the state-space model we have the following:

$$x(k+1) = Ax(k) + Bu(k) \qquad \text{(Eq. 1-1)}$$

$$y(k) = Cx(k) + Du(k)$$

There is an integer *p* chosen such that *p≥(n/m)+1* where n is the desired order of the system and *m* is the number of output values. The *x(k+1)* can be substituted into *y(k)* where you obtain the following equation:

$$\begin{bmatrix} y(k) \\ y(k+1) \\ y(k+2) \\ \vdots \\ y(k+p-1) \end{bmatrix} = \begin{bmatrix} C \\ CA \\ CA^2 \\ \vdots \\ CA^{p-1} \end{bmatrix} x(k) + \begin{bmatrix} D & & & & \\ CB & D & & & \\ CAB & CB & D & & \\ \vdots & \vdots & \vdots & \ddots & \\ CA^{p-2}B & CA^{p-3}B & CA^{p-4}B & \cdots & D \end{bmatrix} \begin{bmatrix} u(k) \\ u(k+1) \\ u(k+2) \\ \\ u(k+p-1) \end{bmatrix} \qquad \text{(Eq. 1-2)}$$

Where:

$$y_p(k) = \begin{bmatrix} y(k) \\ y(k+1) \\ y(k+2) \\ \vdots \\ y(k+p-1) \end{bmatrix} \qquad O_p = \begin{bmatrix} C \\ CA \\ CA^2 \\ \vdots \\ CA^{p-1} \end{bmatrix}$$

$$T_p = \begin{bmatrix} D & & & & \\ CB & D & & & \\ CAB & CB & D & & \\ \vdots & \vdots & \vdots & \ddots & \\ CA^{p-2}B & CA^{p-3}B & CA^{p-4}B & \cdots & D \end{bmatrix} \qquad u_p(k) = \begin{bmatrix} u(k) \\ u(k+1) \\ u(k+2) \\ \\ u(k+p-1) \end{bmatrix}$$

Where we can obtain the following equation:

$$y_p(k) = O_p x(k) + T_p u_p(k) \qquad \text{(Eq. 1-3)}$$

The O_p matrix is the observability matrix and the T_p matrix is the Toeplitz matrix. In order to determine O_p and T_p, the Eq. 1-3 must be expanded as the following:

$$Y_p(k) = O_p X(k) + T_p U_p(k) \qquad \text{(Eq. 1-4)}$$

Where:

$$X(k) = \begin{bmatrix} x(k) & x(k+1) & \cdots & x(k+N-1) \end{bmatrix}$$

$$Y_p(k) = \lfloor y_p(k) \quad y_p(k+1) \quad \cdots \quad y_p(k+N-1) \rfloor$$
$$Y_p(k) = \begin{bmatrix} y(k) & y(k+1) & \cdots & y(k+N-1) \\ y(k+1) & y(k+2) & \cdots & y(k+N) \\ \vdots & \vdots & \ddots & \vdots \\ y(k+p+1) & y(k+p) & \cdots & y(k+N-2) \end{bmatrix}$$

$$U_p(k) = \lfloor u_p(k) \quad u_p(k+1) \quad \cdots \quad u_p(k+N-1) \rfloor$$
$$U_p(k) = \begin{bmatrix} u(k) & u(k+1) & \cdots & u(k+N-1) \\ u(k+1) & u(k+2) & \cdots & u(k+N) \\ \vdots & \vdots & \ddots & \vdots \\ u(k+p+1) & u(k+p) & \cdots & u(k+N-2) \end{bmatrix}$$

Where the integer N must be large, whereas the rank of $U_p(k)$ and $Y_p(k)$ is at least that of O_p. From $U_p(k)$, $Y_p(k)$, and $x(k)$, correlation matrices can be developed for the creation of the information matrix, R. The correlations are calculated as follows:

$$\begin{aligned} R_{yy} &= (1/N) Y_p(k) Y_p^T(k) & R_{yu} &= (1/N) Y_p(k) U_p^T(k) \\ R_{uu} &= (1/N) U_p(k) U_p^T(k) & R_{xu} &= (1/N) X_p(k) U_p^T(k) \\ R_{xx} &= (1/N) X_p(k) X_p^T(k) & R_{yx} &= (1/N) Y_p(k) X_p^T(k) \end{aligned} \qquad \text{(Eq. 1-5)}$$

Eq. 1-4 can be postmultiplied by $U_p^T(k)$ and divided by N to produce:

$$R_{yu} = O_p R_{xu} + T_p R_{uu} \qquad \text{(Eq. 1-6)}$$

If R_{uu}^{-1} exists, then:

$$T_p = [R_{yu} - O_p R_{xu}] R_{uu}^{-1} \qquad \text{(Eq. 1-7)}$$

Similarly, Eq. 1-4 be postmultiplied by $Y_p^T(k)$ and divided by N to produce:

$$R_{yy} = O_p R_{yx}^T + T_p R_{yu}^T \qquad \text{(Eq. 1-8)}$$

and postmultiplying Eq. 1-4 by $X_p^T(k)$ and divided by N to produce:

$$R_{yx} = O_p R_{xx} + T_p R_{xu}^T \qquad \text{(Eq. 1-9)}$$

If Eq. 1-7 is substituted into Eq. 1-8 and Eq. 1-9, for R_{yx} then Eq. 3-8 produces:

$$R_{yy} - R_{yu} R_{uu}^{-1} R_{yu}^T = O_p R_{xx} O_p^T - O_p R_{xu} R_{uu}^{-1} R_{xu}^T O_p^T \qquad \text{(Eq. 1-10)}$$

If the following are defined as:

$$R_{hh} = R_{yy} - R_{yu} R_{uu}^{-1} R_{yu}^T \qquad \text{(Eq. 1-11)}$$

And

$$\tilde{R}_{xx} = R_{xx} - R_{xu} R_{uu}^{-1} R_{xu}^T \qquad \text{(Eq. 1-12)}$$

Then Eq. 1-11 is:

$$R_{hh} = O_p \tilde{R}_{xx} O_p^T \qquad \text{(Eq. 1-13)}$$

Matrices A and C can then be computed using the SVD of R_{hh} where:

$$R_{hh} = U\Sigma^2 U^T = \begin{bmatrix} U_n & U_0 \end{bmatrix} \begin{bmatrix} \Sigma_n^2 & 0 \\ 0 & 0 \end{bmatrix} \begin{bmatrix} U_n^T \\ U_0^T \end{bmatrix} = U_n \Sigma^2 U_n^T \qquad \text{(Eq. 1-14)}$$

If Eq. 1-13 is combined with Eq. 1-14, the following is produced:

$$R_{hh} = O_p \tilde{R}_{xx} O_p^T = U_n \Sigma_n^2 U_n, \qquad \text{(Eq. 1-15)}$$

Where:

$O_p = U_n$

If the case arises where there are not any singular values that become zero due to noise and uncertainties in Σ, a partial decomposition method must be utilized, where $R_{hh}[;,1:(p\text{-}1)m]$ is decomposed. The O_p can be shifted into the following form:

$$O_p(m+1 : pm,:) = \begin{bmatrix} CA \\ CA^2 \\ CA^3 \\ \\ CA^{p-1} \end{bmatrix} = \begin{bmatrix} C \\ CA \\ CA^2 \\ \\ CA^{p-2} \end{bmatrix} A = O_p[1 : (p-1)m,:]A \qquad \text{(Eq. 1-16)}$$

Thus, A can be calculated by:

$$A = O_p[1 : (p-1)m,:] O_p^{\dagger}[1 : (p-1)m,:] \qquad \text{(Eq. 1-17)}$$

Where $O_p^{\dagger}$ is the pseudoinverse of O_p. Matrix A and C can then be computed from O_p where C is the first m rows. A similar partition of the T_p matrix can also be done for the first r columns of the T_p, which is determined as:

$$T[m+1;(p-1)m,1:r] = \begin{bmatrix} CB \\ CAB \\ \vdots \\ CA^{p-2}B \end{bmatrix} = \begin{bmatrix} C \\ CA \\ \vdots \\ CA^{p-2} \end{bmatrix} B = Op[1:(p-1)m,:]B \quad \text{(Eq. 1-18)}$$

Matrix B can then be calculated as

$$B = O_p^{\dagger}[1:(p-1)m,:]T[m+1;(p-1)m,1:r] \quad \text{(Eq. 1-19)}$$

Matrices B and D can be determined through the partitioning of T_p, where B and D is determined through

$$U_{0T} = U_{0n}\begin{bmatrix} D \\ B \end{bmatrix} \quad \text{(Eq. 1-20)}$$

or

$$O_{p\Gamma} = O_{pA}\begin{bmatrix} D \\ B \end{bmatrix} \quad \text{(Eq. 1-21)}$$

In addition, another method is useful where the output error is minimized from the following equation

$$y_N(0) = \Phi\Theta \quad \text{(Eq. 1-22)}$$

Where:

$$\Phi = \begin{bmatrix} C & U_m(0) & 0 \\ CA & U_m(1) & CU_n(0) \\ CA^2 & U_m(2) & CAU_n(0) + CU_n(1) \\ \vdots & \vdots & \vdots \\ CA^{N-1} & U_m(N-1) & \sum_{k=0}^{N-2} CA^{N-k-2}U_n(0) \end{bmatrix}$$

$$\Theta = \begin{bmatrix} x(0) \\ d \\ b \end{bmatrix}$$

From the realization of [*A*,*B*,*C*,*D*], the eigenvalues and eigenvectors are transformed into the modal coordinate space to determine the frequencies and damping ratios of the system.

1.4.2 Eigensystem Realization Algorithm with Observer/Kalman Identification (ERA-OKID)

The ERA-OKID methodology is based on the approximation of the modal parameters based on the state-space model of a structural system. Within the general ERA methodology, the system can then be represented by the relationship between the current state (*x*), input (*u*), and output (*y*) of the system at each time step (*k*), where *k* is an integer (>0) in the following equations:

$$x_{k+1} = Ax_k + Bu_k$$

$$y_k = Cx_k + Du_k \qquad \text{(Eq. 1-23)}$$

Constant matrices *A*, *B*, *C*, and *D* are constructed such that the measurement, y_k, is reproduced based on the input, u_k, and state, x_k, of the system. From these matrices, a Hankel matrix can be compiled of the system pulse response parameters, known as Markov parameters.

$$H(k) = \begin{bmatrix} Y_k & Y_{k+1} & \cdots & Y_{k+i-1} \\ Y_{k+1} & Y_{k+2} & \cdots & Y_{k+i} \\ \vdots & \vdots & \ddots & \vdots \\ Y_{k+j-1} & u(k+p) & \cdots & Y_{k+j+i-2} \end{bmatrix} = \begin{bmatrix} CA^kB & CA^{k+1}B & \cdots & CA^{k+i-1}B \\ CA^{k+1}B & CA^{k+2}B & \cdots & CA^{k+i}B \\ \vdots & \vdots & \ddots & \vdots \\ CA^{k+j-1}B & CA^{k+j}B & \cdots & CA^{k+j+i-1}B \end{bmatrix} \qquad \text{(Eq. 1-24)}$$

Where *i* and *j* are integers that determine the size of the Hankel Matrix. Through the use of the singular value decomposition (SVD)

$$H(0) = U\Sigma V^T = \begin{bmatrix} U_1 & U_2 \end{bmatrix} \begin{bmatrix} S & 0 \\ 0 & 0 \end{bmatrix} \begin{bmatrix} V_1^T \\ V_2^T \end{bmatrix} = U_1 S V_1^T \qquad \text{(Eq. 1-25)}$$

Where *U* and *V* are the unitary matrices, and *Σ* contains the singular values of *H(0)*. The number of non-zero singular values provides the order of the system. From the SVD, the system matrices are determined as:

$$A = S^{-1/2} U_1^T H(1) V_1 S^{-1/2}, \qquad \text{(Eq. 1-26)}$$

$$B = S^{1/2} V_1^T E_r, \qquad \text{(Eq. 1-27)}$$

$$C = E_m^T U_1 S^{1/2} \qquad \text{(Eq. 1-28)}$$

Where $E_r = \begin{bmatrix} I_{rxr} & 0 & 0 & \cdots & 0 \end{bmatrix}_{rxn_2}^T$ and E_m are defined analogously. The modal parameters can then be determined based on the matrices *A*, *B*, *C*, and *D*. With an understanding of the general ERA method, we can appreciate how the OKID modifies the ERA methodology. The ERA-OKID method involves the use of an observer to stabilize the system and increase its accuracy. The original state-space equation equations are rewritten to determine the so-called observer parameters using the previously stated process. The observer equations are written by adding and subtracting My_k in the state equation, where the following system is formulated:

$$x_{k+1} = \hat{A} x_k + \hat{B} u_k \qquad \text{(Eq. 1-29)}$$

$$y_k = C x_k + D u_k$$

Where $\hat{A} = (A + MC)$, $\hat{B} = \begin{bmatrix} (B + MD), & (-M) \end{bmatrix}$, and *M* is an arbitrary matrix that allows the system to become as stable as possible. Matrix *M* is chosen so that $\hat{A}^k \approx C\hat{A}^k \hat{B} \approx 0$ for $k \geq p$, where

p is chosen such that is sufficiently large enough for the stabilization to occur. For the condition that the initial condition is zero, it is possible to write the solution to the observer system as follows:

$$y_{q\times l} \approx \hat{Y}_{q\times[(q+m)(l-1)+m]} V_{[(q+m)(l-1)+m]\times l} \qquad \text{(Eq. 1-30)}$$

Where:

$$y = \begin{bmatrix} y(0) & \cdots & y(p) & \cdots & y(\ell-1) \end{bmatrix}$$

$$\hat{Y} = \begin{bmatrix} D & C\hat{A} & C\hat{A}\hat{B} & \cdots & C\hat{A}^{p-1}\hat{B} \end{bmatrix}$$

And the matrix V is comprised of the input and output data:

$$V = \begin{bmatrix} u(0) & u(1) & u(2) & \cdots & u(p) & \cdots & u(l) \\ & v(0) & v(1) & \cdots & v(p-1) & \cdots & v(l-1) \\ & & v(0) & \cdots & v(p-2) & \cdots & v(l-2) \\ & & & \ddots & \vdots & \cdots & \vdots \\ & & & & v(0) & \cdots & v(l-p-1) \end{bmatrix} \qquad \text{(Eq. 1-31)}$$

The observer Markov parameters are the block partitions of matrix $\hat{Y}$. And they are obtained by determining the least-squares solution to Eq. 1-30, $\hat{M} = YV^{\dagger}$ (where $V^{\dagger}$ is the pseudoinverse of V). Once the observer Markov parameters are determined, the system Markov parameters can be written in terms of the observer Markov parameters. The sequences are determined for:

$$Y_k = CA^k B \qquad \text{(Eq. 1-32)}$$

$$Y_k^o = CA^k M \qquad \text{(Eq. 1-33)}$$

The combined Markov parameter is formulated as:

$$P_k = \begin{bmatrix} Y_k & Y_k^o \end{bmatrix} \quad \text{(Eq. 1-34)}$$

Where the Hankel Matrix is then created. The general ERA method can then be utilized to determine the matrices *A*, *B*, *M*, *C*, and *D*, and ultimately, the modal parameters of the system.

1.4.3 Numerical Algorithm for Subspace State Space System Identification (N4SID)

The subspace identification methods are based on the use of the projections where the state sequences are determined based on the Kalman filter and are then minimized through the use of a least-squares approximation, which is the opposite of most classical system identification methods. The N4SID method views the problem of system identification as both a deterministic and stochastic system. The combined system equations are formulated as the following:

$$x_{k+1} = Ax_k + Bu_k + w_k$$

$$y_k = Cx_k + Du_k + v_k \quad \text{(Eq. 1-35)}$$

Where $x_k = x_k^d + x_k^s$ and $y_k = y_k^d + y_k^s$. The superscripts *d* and *s* represent the contribution of the deterministic and stochastic system to the state and output variables, respectively. The sequence w_k is the zero mean, white process noise and the sequence v_k is the zero mean, white measurement noise. Both sequences are independent random variables and the following equation is true:

$$E\left[\begin{pmatrix} w_k \\ v_k \end{pmatrix}\begin{pmatrix} w_l^t & v_l^t \end{pmatrix}\right] = \begin{bmatrix} Q^s & S^s \\ (S^s)^t & R^s \end{bmatrix}\delta_{kl} \geq 0 \quad \text{(Eq. 1-36)}$$

The deterministic subsystem is represented by the following equations:

$$x_{k+1}^d = Ax_k^d + Bu_k \quad \text{(Eq. 1-37)}$$

$$y_k^d = Cx_k^d + Du_k$$

The x_{k+1} can be substituted into y_k where you obtain the following equations:

$$Y_i(k) = \Gamma_i X_i + H_i^d U_i$$

$$X_i = A^i X_i^d + \Delta_i^d U_i \qquad \text{(Eq. 1-38)}$$

Where:

$$\Gamma_i = \begin{bmatrix} C \\ CA \\ CA^2 \\ \vdots \\ CA^{i-1} \end{bmatrix} \quad , \quad \Delta_i^d = \begin{bmatrix} A^{i-1}B & \cdots & A^iB & B \end{bmatrix}$$

$$H_i^d = \begin{bmatrix} D & & & & \\ CB & D & & & \\ CAB & CB & D & & \\ \vdots & \vdots & \vdots & \ddots & \\ CA^{i-2}B & CA^{i-3}B & CA^{i-4}B & \cdots & D \end{bmatrix} \quad , \quad X_i^d(k) = \begin{bmatrix} x_i^d & x_{i+1}^d & \cdots & x_{i+j-1}^d \end{bmatrix}$$

$$U_{0/i-1} = \begin{bmatrix} u_0 & u_1 & u_2 & \cdots & u_{j-1} \\ u_1 & u_2 & u_3 & \cdots & u_{j-2} \\ u_2 & u_3 & u_4 & \cdots & u_{j-3} \\ \vdots & \vdots & \vdots & \ddots & \vdots \\ u_{i-1} & u_i & u_{i-1} & \cdots & u_{i+j-1} \end{bmatrix} \quad Y_{0/i-1} = \begin{bmatrix} y_0 & y_1 & y_2 & \cdots & y_{j-1} \\ y_1 & y_2 & y_3 & \cdots & y_{j-2} \\ y_2 & y_3 & y_4 & \cdots & y_{j-3} \\ \vdots & \vdots & \vdots & \ddots & \vdots \\ y_{i-1} & y_i & y_{i-1} & \cdots & y_{i+j-1} \end{bmatrix}$$

The stochastic subsystem is represented by the following equations:

$$x_{k+1}^s = Ax_k^s + w_k$$

$$y_k^s = Cx_k^s + v_k \qquad \text{(Eq. 1-39)}$$

The covariance between the input and output data from Eq. 1-39 is shown with the following formulas:

$$P^s = E\left[x_k^s (x_k^s)^t\right] = AP^s A^t + Q^s \qquad \text{(Eq. 1-40)}$$

$$G^s = E\left[x_k^s (y_k^s)^t\right] = AP^s C^t + S^s \qquad \text{(Eq. 1-41)}$$

$$\Lambda = E\left[y_k^s (y_k^s)^t\right] = CP^s C^t + R^s \qquad \text{(Eq. 1-42)}$$

The stochastic subsystem controllability, state, block Toeplitz covariance, and block Toeplitz cross-covariance matrices are the following:

$$\Delta_i^s = \begin{bmatrix} A^{i-1}G & \cdots & A^iG & G \end{bmatrix}, \quad X_k^s(k) = \begin{bmatrix} x_i^s & x_{i+1}^s & \cdots & x_{i+j-1}^s \end{bmatrix}$$

$$L_i^s = E\left[Y_{0/i} Y_{0/i-1}^t\right] = \begin{bmatrix} \Lambda_0 & \Lambda_{-1} & \cdots & \Lambda_{i-1} \\ \Lambda_1 & \Lambda_0 & \cdots & \Lambda_{i-2} \\ \vdots & \vdots & \ddots & \vdots \\ \Lambda_{i-1} & \Lambda_{i-2} & \cdots & \Lambda_0 \end{bmatrix}$$, and

$$H_i^s = E\left[Y_{0/i} Y_{i/2i-1}^t\right] = \begin{bmatrix} \Lambda_i & \Lambda_{i-1} & \cdots & \Lambda_i \\ \Lambda_{i+1} & \Lambda_i & \cdots & \Lambda_2 \\ \vdots & \vdots & \ddots & \vdots \\ \Lambda_{2i-1} & \Lambda_{2i-2} & \cdots & \Lambda_i \end{bmatrix} = \Gamma_i \Delta_i^s$$

The past and future inputs are denoted by $U_{0/i-1}$ and $U_{i/2i-1}$, respectively. Similarly, the past and future output are denoted by $Y_{0/i-1}$ and $Y_{i/2i-1}$. The matrix input and output equations due to the deterministic and stochastic subsystems become:

$$Y_{0/i-1} = \Gamma_i X_0^d + H_i^d U_{0/i-1} + Y_{0/i-1}^s, \qquad \text{(Eq. 1-43)}$$

$$Y_{i/2i-1} = \Gamma_i X_i^d + H_i^d U_{i/2i-1} + Y_{i/2i-1}^s \qquad \text{(Eq.1-44)}$$

And

$$X_i^d = A^i X_0^d + \Delta_i^d U_{0/i-1} \qquad \text{(Eq. 1-45)}$$

Oblique projections are utilized to transform the future output, $Y_{i/2i-1}$, onto the past and future inputs, and the past outputs, $U_{0/i-1}$, $U_{i/2i-1}$ and $Y_{0/i-1}$, respectively. The projections aid in the simplification of the computational effort. A block Hankel matrix is derived by

$$H = \begin{pmatrix} U_{0/2i-1} \\ Y_{0/i-1} \end{pmatrix} \Big/ \sqrt{j}$$

Where $\sqrt{j}$ operator the denotes the Expected Value Operator. The block Hankel is factored using the RQ decomposition to simplify the system

$$\begin{bmatrix} U_{0/i-1} \\ U_{i/i} \\ U_{i+1/2i-1} \\ Y_{0/i-1} \\ Y_{i/i} \\ Y_{i+1/2i-1} \end{bmatrix} = \begin{bmatrix} R_{11} & & & & & \\ R_{21} & R_{22} & & & & \\ R_{31} & R_{32} & R_{33} & & & \\ R_{41} & R_{42} & R_{43} & R_{44} & & \\ R_{51} & R_{52} & R_{53} & R_{54} & R_{55} & \\ R_{61} & R_{62} & R_{63} & R_{64} & R_{65} & R_{66} \end{bmatrix} \begin{bmatrix} Q_1^T \\ Q_2^T \\ Q_3^T \\ Q_4^T \\ Q_5^T \\ Q_6^T \end{bmatrix} \qquad \text{(Eq. 1-46)}$$

The projection of the future outputs onto the past and future inputs and the past outputs are determined by

$$Z_i = Y_{i/2i-1} \Big/ \begin{bmatrix} U_{0/i-1} \\ U_{i/2i-1} \\ Y_{0/i-1} \end{bmatrix} = \begin{bmatrix} L_i^1 & L_i^2 & L_i^3 \end{bmatrix} \begin{bmatrix} U_{0/i-1} \\ U_{i/2i-1} \\ Y_{0/i-1} \end{bmatrix} \qquad \text{(Eq. 1-47)}$$

(Eq. 1-48)

$$Z_{i+1} = Y_{i+1/2i-1} \Big/ \begin{bmatrix} U_{0/i} \\ U_{i+1/2i-1} \\ Y_{0/i} \end{bmatrix} = \begin{bmatrix} L_{i+1}^1 & L_{i+1}^2 & L_{i+1}^3 \end{bmatrix} \begin{bmatrix} U_{0/i} \\ U_{i+1/2i-1} \\ Y_{0/i} \end{bmatrix}$$

Where $L_i^1 = \Gamma_i([A^i - Q_i\Gamma_i]S(R^{-1}) + \Delta_i^d - Q_i H_i^d)$, $L_i^2 = H_i^{d+}\Gamma_i[A^i - Q_i\Gamma_i]S(R^{-1})$, and $L_i^3 = \Gamma_i Q_i$. The projections Z_i are used to create new state space equations:

$$Z_i = \Gamma_i \hat{X}_i + H_i^d U_{i/2i-1}$$

$$Z_{i+1} = \Gamma_{i-1} \hat{X}_{i+1} + H_{i-1}^d U_{i+1/2i-1} \qquad \text{(Eq. 1-49)}$$

The Singular Value Decomposition is performed on the portion of Z_i that contains the past inputs and outputs

$$\begin{bmatrix} L_i^1 & L_i^3 \end{bmatrix} \begin{bmatrix} U_{0/i-1} \\ Y_{0/i-1} \end{bmatrix} = \begin{bmatrix} U_1 & U_2 \end{bmatrix} \begin{bmatrix} \Sigma_1 & 0 \\ 0 & 0 \end{bmatrix} V^T \qquad \text{(Eq. 1-50)}$$

Where the system order is determined by the number of nonzero singular values in Σ_1. The observability matrix Γ_i can be determined since it has the same number of column space at L_i $\Gamma_i = U_1 \Sigma_1^{1/2}$ and $\Gamma_{i-1} = \underline{U}_1 \Sigma_1^{1/2}$, where the underlined value represents the augmented matrix whose last row is deleted. Due to the projections, the system can then be described as a linear system, where Z_{i+1} can be found due to Z_i using the general Kalman filter equations

$$X_{i+1} = A\hat{X}_i + BU_{i/i} + K_i(Y_{i/i} - C\hat{X}_i - DU_{i/i})$$

$$Y_i = C\hat{X}_i + DU_{i/i} + (Y_{i/i} - C\hat{X}_i - DU_{i/i}) \qquad \text{(Eq. 1-51)}$$

Where $\varepsilon_i = (Y_{i/i} - C\hat{X}_i - DU_{i/i})$, which is the residual.

From Eq. 1-49 and Eq. 1-51 the following system of equations is determined

$$\begin{bmatrix} \hat{X}_{i+1} \\ Y_{i/i} \end{bmatrix} = \begin{bmatrix} A \\ C \end{bmatrix} \hat{X}_i + \begin{bmatrix} B \\ D \end{bmatrix} U_{i/i} + \begin{bmatrix} U_{0/2i-1} \\ Z_i \\ \hat{X}_i \end{bmatrix}^{\perp} \quad \text{(Eq. 1-52)}$$

$$\begin{bmatrix} \Gamma_{i-1}^{\dagger} Z_{i+1} \\ Y_{i/i} \end{bmatrix} = \begin{bmatrix} A \\ C \end{bmatrix} \hat{X}_i + \begin{bmatrix} K_{12} \\ K_{22} \end{bmatrix} U_{i/i} + \begin{bmatrix} U_{0/2i-1} \\ Z_i \\ \hat{X}_i \end{bmatrix}^{\perp}$$

We now have a linear equation in which the least approximation can be used:

$$\min \left\| \begin{bmatrix} \Gamma_{i-1}^{\dagger} Z_{i+1} \\ Y_{i/i} \end{bmatrix} - \begin{bmatrix} A & K_{12} \\ C & K_{22} \end{bmatrix} \begin{bmatrix} \Gamma_i^{\dagger} Z_i \\ U_{i/2i-1} \end{bmatrix} \right\|_F^2 \quad \text{(Eq. 1-53)}$$

The system matrices, *A*, *B*, *C*, *D*, Q^s, S^s, and R^s can then be determined.

1.4.4 Enhanced Frequency Domain Decomposition (EFDD)

Enhanced Frequency Domain Decomposition is an output only frequency domain method which estimates modal parameters using spectral densities with the condition of a white noise input. The response can be formed by modal coordinates and the corresponding mode shape:

$$y(t) = \Phi q(t) \quad \text{(Eq. 1-54)}$$

From response signals of each sensor, a correlation matrix could be constructed including auto-correlation and cross-correlation where Φ^H is the Hermitian conjugate of Φ:

$$C_{yy}(\tau) = E(y(t+\tau)y(t)^T) = \Phi C_{qq}(\tau)\Phi^H \quad \text{(Eq. 1-55)}$$

After applying Fourier Transform to the correlation matrix, Eq. 1-55 can be written as:

$$G_{yy}(\omega) = \Phi G_{qq}(\omega)\Phi^H \quad \text{(Eq. 1-56)}$$

Eq. 1-56 can also be interpreted as:

$$G_{yy}(\omega) = H(\omega)^* G_{xx}(\omega) H(\omega)^T \quad \text{(Eq. 1-57)}$$

Where $G_{xx}(\omega)$ is the input Power Spectral Density (PSD) matrix, $G_{yy}(\omega)$ is the output PSD matrix, $H(\omega)$ is the Frequency Response function (FRF) matrix, and * denotes complex conjugate. $H(\omega)$ is written in a partial fraction form as:

$$H(\omega) = \frac{Y(\omega)}{X(\omega)} = \sum_{i=1}^{m} \frac{R_i}{j\omega - \lambda_i} + \frac{R_i^*}{j\omega - \lambda_i^*} \quad \text{(Eq. 1-58)}$$

Where $\lambda_i = -\sigma_i + j\omega_{di}$ is the pole containing damping and damped natural frequency, and *m* is the total number of modes. If the input is white noise, the input PSD matrix $G_{xx}(\omega)$ becomes a constant, and therefore the output PSD matrix $G_{yy}(\omega)$ can be expressed as Eq. 1-59 where ϕ_i is the mode shape and d_i is the scaling factor.

$$G_{yy}(\omega) = \sum \frac{d_i \phi_i \phi_i^T}{j\omega - \lambda_i} + \frac{d_i^* \phi_i^* \phi_i^{*T}}{j\omega - \lambda_i^*} \quad \text{(Eq. 1-59)}$$

A singular value decomposition $G_{yy}(\omega) = U\Sigma V^T$ is then applied to the output PSD matrix in order to estimate mode shapes and singular values (only first/largest singular values are selected) at each frequency. Similar to 'peak-picking' method, frequencies corresponding to energy peaks are identified as predominant frequencies. A Modal Assurance Criteria (MAC) is calculated by the distance between the mode shape of each predominant frequency and all mode shapes at every other frequency. A frequency range is selected for each predominant frequency as it includes frequencies of high MAC values. Therefore, taking MAC value as the weight, the frequency for each mode and the corresponding mode shape is computed within each frequency range. Data is transferred back to the time domain in order to obtain the decay function. Peaks and valleys of the decay function are picked for regression fitting, where the damping ratio of each mode can be estimated. Moreover, the frequency for each mode can also be calculated by counting the number of times the decay function crosses the zero axes per second.

1.4.5 Unscented Kalman Filter (UKF)

UKF is a method using sigma points to approximate probability distributions of parameters. Parameters mean and covariance are approximated from a group of sigma points, and each point propagates through the dynamic structure model to generate a response at the next step. Considering a nonlinear system with a state equation and a measurement equation Eq. 1-60 and Eq. 1-61:

$$x_k = f_{k-1}(x_{k-1}, u_{k-1}) + w_{k-1} \qquad \text{(Eq. 1-60)}$$

$$y_k = h_k(x_k, u_k) + v_{k-1} \qquad \text{(Eq. 1-61)}$$

Where u_k, x_k and y_k are the input, state the observation at time instant k, and both state and observation are contaminated by Gaussian white noise w_k and v_k, which have covariance matrix Q_k and R_k, respectively. At each step, the state point estimate and state covariance are updated by observation through Eq. 1-62 and 1-63:

$$\hat{x}_{k|k} = \hat{x}_{k|k-1} + K_k(y_k - \hat{y}_{k|k-1}) \quad \text{(Eq. 1-62)}$$

$$\hat{P}^{xx}_{k|k} = \hat{P}^{xx}_{k|k-1} - K_k \hat{P}^{yy}_{k|k-1} K_k^T \quad \text{(Eq. 1-63)}$$

Where $\hat{x}_{k|k}$ and $\hat{P}^{xx}_{k|k}$ are updated mean and covariance, K is the Kalman Gain calculated from the cross-covariance matrix, and $\hat{x}_{k|k-1}$, $\hat{P}^{xx}_{k|k-1}$, $\hat{y}_{k|k-1}$ and $\hat{P}^{yy}_{k|k-1}$ are state point prediction, state covariance prediction, observation point prediction and observation covariance prediction, respectively. For a system with n parameters, $2n$+1 sigma points are required to capture the true mean and covariance, and state and observation predictions are computed from weighted (W_m represents the weight for mean, and W_c represents the weight for covariance) points as shown through Eq. 1-64 to Eq. 1-67:

$$\hat{x}_{k|k-1} = \sum_{i}^{2n+1} W_m^i X_k^i \quad \text{(Eq. 1-64)}$$

$$\hat{P}^{xx}_{k|k-1} = \sum_{i}^{2n+1} W_c^i [X_k^i - \hat{x}_{k|k-1}][X_k^i - \hat{x}_{k|k-1}]^T + Q_{k-1} \quad \text{(Eq. 1-65)}$$

$$\hat{y}_{k|k-1} = \sum_{i}^{2n+1} W_m^i Y_k^i \quad \text{(Eq. 1-66)}$$

$$\hat{P}^{yy}_{k|k-1} = \sum_{i}^{2n+1} W_c^i [Y_k^i - \hat{y}_{k|k-1}][Y_k^i - \hat{y}_{k|k-1}]^T + R_k \quad \text{(Eq. 1-67)}$$

where X_k^i is the i^{th} sigma point at time k, and Y_k^i is the corresponding observation when X_k^i is plugged in to the model through Eq. 1-61.

1.4.6 Particle Swarm Optimization (PSO)

PSO works by initializing a population of candidate particles, which move in the search space to minimize the objective function. Each particle will update itself based on its own local best-known position as well as the global best-known position found by the entire group. PSO is selected due to its convenience in implementation, the fewer number of hyperparameters, and the capability of dealing with high dimensional optimization problems. As a gradient-free algorithm, PSO does not require the objective function surface to be differentiable and is suitable in this study, given that the objective function measures the discrepancy between recorded response and analytical response. As shown in Eq. 1-68, the velocity of particle i at dimension d at the k^{th} step (i.e., v_{id}^{k}) is updated by three terms. The first term represents the velocity of particle i at the previous step factored by w^k, where w (Eq. 1-70) decreases linearly as the algorithm carries on with index k (K is the total number of steps). The second term in Eq. 1-68 guides the particle's position (i.e., x_{id}^{k}) towards the local best position (i.e., x_{id}^{p-best}). The third term in Eq. 1-68 guides the particle towards the global best position (i.e., x_{d}^{g-best}), which is not a function of i. c_1 and c_2 are the hyperparameters that can be tuned as learning rates, and r_1 and r_2 are random variables ranging from 0 to 1 in order to increase uncertainty in the searching process. Finally, the position is updated by summing up the previous position and the velocity, as shown in Eq. 1-69.

$$v_{id}^{k} = w^k v_{id}^{k-1} + c_1 r_1 \left(x_{id}^{p-best} - x_{id}^{k-1}\right) + c_2 r_2 \left(x_{d}^{g-best} - x_{id}^{k-1}\right) \qquad \text{(Eq. 1-68)}$$

$$x_{id}^{k} = x_{id}^{k-1} + v_{id}^{k-1} \qquad \text{(Eq. 1-69)}$$

$$w^k = w_{max} - (w_{max} - w_{min}) \frac{k}{K} \qquad \text{(Eq. 1-70)}$$

1.4.7 Covariance Matrix Adaption Evolution Strategy (CMA-ES)

CMA-ES is widely used to solve non-linear non-convex optimization problems. In CMA-ES, several particles are randomly generated, and each particle represents a particular setting of parameters that are random variables of the objective function to be minimized or maximized. The mean of the distribution of the particles as well as the covariance matrix of the distribution of the particles are both updated during search steps until the algorithm converges at the global minimum as illustrated in Eq. 1-71 where m_{t+1} stands for the mean of the distribution at step t+1, and x_i stands for a setting of parameters of the i^{th} particle. The mean of the distribution m_{t+1} at step t+1 is updated based on the mean m_t at step t and the weight w_i, which is the weight of the i^{th} particle proportional to the objective function of the i^{th} particle. μ in Eq. 1-72 stands for the total number of particles. Eq. 1-72 illustrates the update of the covariance matrix of the distribution C_{t+1}at step t+1. $c_1$and $c_\mu$are both hyperparamters that affect the rate of convergence. p_{t+1} is the path at step t+1 and $\sigma_t$is a normalization factor at step t, which are updated as shown in Eq. 1-73 and Eq. 1-74, respectively. c and μ_w and c_σ and d_σ in Eq. 1-73 and Eq. 1-74, respectively, are also hyperparameters of the algorithm. $E||N(0,I)||$ in Eq. 1-74 represents the expectation of the Euclidean norm of the normal distribution $N(0, I)$ ands_{t+1} in Eq. 1-74 is the step size that is updated based on Eq. 1-75, where matrix B is formed from the normal distribution $N(0, I)$.

$$m_{t+1} = \sum_{i=1}^{\mu} w_i x_i = m_t + \sum_{i=1}^{\mu} w_i (x_i - m_t) \quad \text{(Eq. 1-71)}$$

$$C_{t+1} = (1 - c_1 - c_\mu) C_t + c_1 p_{t+1} p_{t+1}^T + c_\mu \sum_{i=1}^{\mu} w_i (\frac{x_i - m_t}{\sigma_t}) (\frac{x_i - m_t}{\sigma_t})^T \quad \text{(Eq. 1-72)}$$

$$p_{t+1} = (1-c)p_t + \sqrt{c(2-c)}\sqrt{\mu_w}\frac{m_{t+1} - m_t}{\sigma_t} \quad \text{(Eq. 1-73)}$$

$$\sigma_{t+1} = \sigma_t \, exp(\frac{c_\sigma}{d_\sigma}(\frac{||s_{t+1}||}{E||N(0,I)||} - 1)) \quad \text{(Eq. 1-74)}$$

$$s_{t+1} = (1-c_\sigma)s_t + \sqrt{c_\sigma(2-c_\sigma)}\sqrt{\mu_w}B\sum_{i=1}^{\mu} w_i x_i \quad \text{(Eq. 1-75)}$$

1.5 REFERENCES

ASCE-American Society of Civil Engineers (2017). *Minimum Design Loads for Buildings and Other Structures* (ASCE/SEI 7–10). American Society of Civil Engineers: Reston, VA.

ASCE-American Society of Civil Engineers (2010). *Minimum Design Loads for Buildings and Other Structures* (ASCE/SEI 7–10). American Society of Civil Engineers: Reston, VA.

ATC-Applied Technology Council (1996). *Seismic Evaluation and Retrofit of Concrete Buildings*, Volume 1. Applied Technology Council, Redwood City, CA

ATC-Applied Technology Council (2010). Modeling and acceptance criteria for seismic design and analysis of tall buildings. *PEER/ATC-72-1*, Applied Technology Council in cooperation with the Pacific Earthquake Engineering Research Center, Redwood City, CA.

Bentz, A., and Kijewski-Correa, T. (2008). Predictive models for damping in buildings: the role of structural system characteristics. In *Proceedings of the 2008 Structures Congress*, 18th Analysis and Computation Specialty Conference, Vancouver, Canada.

Bernal, D. (1994). Viscous damping in inelastic structural response. *ASCE Journal of Structural Engineering*, 120(4): 1240-1254.

Bernal, D., Kojidi, S., Kwan, K., and Döhler, M. (2012). Damping Identification in Buildings from Earthquake Records. *SMIP12 Seminar Proceedings*, 2012.

Davenport, A. G., & Hill-Carroll, P. (1986). Damping in tall buildings: its variability and treatment in design. In *Building motion in wind, ASCE*, p. 42-57.

Fang, J. Q., Jeary, A. P., Li, Q. S., and Wong, C. K (1999). Random damping in buildings and its AR model. *Journal of Wind Engineering and Industrial Aerodynamics*, 79(1), 159-167.

FEMA-Federal Emergency Management Agency (2012). *Seismic Performance Assessment of Buildings* Volume 1 – Methodology, Tech. Rep. P-58-1, Washington, D.C.

Hall, J. F. (2005). Problems encountered from the use (or misuse) of Raleigh damping. *Earthquake Engineering and Structural Dynamics*, 35(5): 525-545.

Jeary, A.P. (1997) Damping in structures. *Journal of Wind Engineering and Industrial Aerodynamics*, 72: 345 – 55.

LATBSDC (2018). *An Alternative Procedure for Seismic Analysis and Design of Tall Buildings Located in The Los Angeles Region.* Los Angeles Tall Buildings Structural Design Council.

Li, Q. S., Liu, D. K., Fang, J. Q., Jeary, A. P., and Wong, C. K. (2000). Damping in buildings: its neural network model and AR model. *Engineering Structures*, 22(9), 1216-1223.

McKenna, F., Scott, M. H., and Fenves, G. L. (2010), Nonlinear Finite Element Analysis Software Architecture using Object Composition. *Journal of Computing in Civil Engineering*, 24(3), 95-107.

PEER, 2017. *Guidelines for Performance-Based Seismic Design of Tall Buildings-ver. 2*, PEER Report 2017/06, prepared by the TBI Guidelines Working Group, Berkeley, CA.

Priestley, M.J.N., Calvi, M.C., and Kowalsky, M.J. (2007). Displacement-Based Seismic Design of Structures. *IUSS Press*, Pavia, 670 pp.

Satake, N., Suda, K. I., Arakawa, T., Sasaki, A., and Tamura, Y. (2003). Damping evaluation using full-scale data of buildings in Japan. *Journal of structural engineering*, 129(4), 470-477.

Spence, S.M.J., Kareem, A. (2014). Tall Building and Damping: A Concept-Based Data-Driven Model. *ASCE Journal of Structural Engineering*, Vol. 140, Issue 5.

Tamura, Y., and Yoshida, A. (2008). Amplitude dependency of damping in buildings. In *Proceedings of the 18th Analysis and Computation Specialty Conference* (Vol. 315).

Wyatt, T. A. (1977). Mechanisms of damping. *In Proceeding of a Symposium of Dynamic Behavior of Bridges* at the Transport and Road Research Laboratory, Crowthorne, Berkshire, England, May 19, 1977. (No. TRRL Rpt. 275 Proceeding).

Zareian, F., and Medina, R. (2010). A practical method for proper modeling of structural damping in inelastic plane structural systems. *Computers and Structures*, 88(1-2): 45-53.

CHAPTER 2: EVALUATION OF NATURAL PERIODS AND MODAL DAMPING RATIOS FOR SEISMIC DESIGN OF BUILDING STRUCTURES

2.1 INTRODUCTION

Currently, the use of Equivalent Modal Damping Ratio (EMDR) in seismic design has been at best ambiguous and not well defined. This is a major issue for the seismic design of new buildings and retrofit of existing structures. An estimate of fundamental period and EMDR is necessary for the structural design process (ASCE, 2010; 2017a; 2017b; LATBSDC 2018; PEER, 2017). Therefore, it is necessary to accurately model the energy dissipation of a building during seismic excitations. However, EMDR continues to include much uncertainty and the ratios currently used in seismic design continue to be anything but well-defined. The Minimum Design Loads for Buildings and Other Structures, ASCE/SEI 7 (ASCE, 2010, 2017b) requires the use of EMDR = 5%, whereas FEMA P-58-1 (FEMA, 2012) requires 1%< EMDR < 5% for the predominant modes. Similarly, the Los Angeles Tall Buildings Structural Design Council (LATBSDC, 2018) and Tall Building Initiative Guidelines (2017) suggests that the additional modal damping should not exceed 2.5% of the critical damping for predominant modes. It is evident that an EMDR between 1% and 5% should be used; however, the respective damping values for different Lateral Force Resisting Systems (LFRS) are not explicitly given, injecting additional uncertainty into the design process.

A Building's response to seismic excitation is a complex phenomenon and representation of its energy dissipation via a linear model (e.g., EMDR) is an approximation. EMDR assumes all sources of energy dissipation is explained by modal damping. EMDR incorporates all energy dissipation mechanisms (e.g., frictional damping and viscous damping) without contamination from energy dissipation through nonlinear action of structural components. EMDR in building structures is not a constant value and it can depend on many parameters such as building height, occupancy, and structural system. Researchers have suggested small values for the first mode damping ratio in tall buildings compared to low-rises (Cruz and Miranda, 2016; Satake *et al.*, 2003; Fritz *et al.*, 2009). As will be illustrated in the next sections, such a low estimate is directly related to the low sensitivity of the acceleration-response-based objective functions used in optimization routines for system identification of tall buildings. EMDRs also vary with amplitudes; much of the energy dissipation in building structures is from the friction between various structural as well as non-structural elements (Wyatt, 1977). Several studies have shown that EMDR is amplitude-dependent (Jeary, 1997; Li *et al.*, 1999; Davenport and Hill-Caroll, 1986; Fang *et al.*, 1999; Tamara, 2008). These studies showed that EMDR remains constant at low excitation amplitudes, and then increases with amplitude after a certain threshold to reach a plateau at a higher excitation amplitude (Jeary 1997). Other researchers related EMDR values with their corresponding frequency and period. Satake *et al.* (2003) found that EMDR decrease with the natural period, it is amplitude-dependent and increasing with mode shape number. Bernal *et al.* (2012) similarly concluded that EMDR, although contained a high amount of variability, increased with a natural frequency. Bentz and Kijewski-Correa (2008) discussed the prediction of EMDR based on the dominance of structural systems deformation mechanisms, shear or cantilever (i.e., flexural) action (Miranda, 1999).

This study utilizes a technique to combine the results of time-domain and frequency-domain modal system identification methods to arrive at an unbiased estimate of structure modal properties (i.e., natural periods and EMDRs). Compared to the previous studies in which a single system identification was utilized, this study gathers results from multiple system identification methods to form a combined distribution of modal properties by which stable estimates of modal damping and periods can be achieved. Moreover, this study utilizes a dataset of seismic events along with a more detailed classification of building types compared to previous similar research. Statistical analysis is conducted to generate equations for the prediction of natural period and EMDR of building structures. Results are compared with those of other researchers and sources of difference between the estimates are explained. A 52-story office building in Los Angeles (LA-52)–building #24602–is selected for case study and discussion.

2.2 SYSTEM IDENTIFICATION

The suggested method for estimating modal properties (i.e., natural periods and EMDR) of building structures is rooted in four system identification methods, including: (1) Eigensystem realization algorithm with an observer Kalman Filter (ERA-OKID) method (Juang, 1994), (2) System Realization Using Information Matrix (SRIM) method (Ljung, 1999), (3) Subspace algorithms for identification of combined deterministic-stochastic systems (N4SID) method (Van Overschee & De Moor, 1994), and (4) Enhanced Frequency Domain Decomposition (EFDD) method (Le & Tamura. 2009). The three time-domain methods focus on different targets: ERA-OKID solves a least-square fit to pulse responses; SRIM solves a least-square fit to data correlations with time lags; N4SID is a least-square fit to the residual of projections of future data onto past data. While ERA-OKID innovatively utilizes an observer state/Kalman Filter instead of the traditional Frequency Response Functions to solve Markov Parameters, its recursive algorithm is computationally expensive. N4SID avoids iterative algorithms and can identify deterministic and stochastic sub-systems simultaneously, but the QR factorization could also be time-consuming if the matrix is of large size. SRIM gets rid of the formation of large Hankel Matrices and QR factorization; however, it still involves matrix inversion and can thus lead to ill-conditioned matrices. EFDD, while providing an accurate estimate for frequency contents, can overestimate the damping ratio due to spectral leakage. In summary, the three time-domain methods are first combined to gather a complete distribution of results, and EFDD prunes that estimate by eliminating fictitious modes with its damping estimates unused. Estimated pairs of frequency and EMDR vary with the choice of system identification method as well as the selection of parameters for each system realization, especially in time-domain methods (parameters such as model order, starting point, time length). To alleviate this issue, a combined method is recommended for the estimation of a unique and stable set of frequency and EMDR in each mode considering all possible model parameters within the first three system identification methods listed above (i.e., time-domain system identification methods). In this study, model order N and the time length p are considered as two parameters in all three time-domain methods. N stands for the model order, which can be mathematically understood as the number of non-trivial eigenvalues of the state matrix and can be physically interpreted as the number of pairs of natural frequencies and damping ratios that sufficiently describe the structural system. p stands for the time (data) length and its interpretation depends on the system identification methods. In SRIM, p represents stacked data layers of input and output matrices with shifted time lags. For ERA-OKID, p represents the length of Markov parameters beyond which the state matrix is asymptotically stable and can therefore be neglected and truncated. Finally, in N4SID, p represents the position separating past and future data. After combining the results of the three system identification methods (see below), the estimates of modal properties are compared with the results of the fourth method listed above (i.e., EFDD system identification method) for verification.

The process for combining the results of the system identification methods was developed to assure the results are encompassing and can address the variety of structural systems. Several combinations of model parameters (i.e., N and p) are selected in each time-domain method; model order (N) is selected based on the number of stories and the time length representation (p) is selected based on the stability and rate of convergence of the state-space model. Each specific combination of model parameters will lead to estimates of frequency and EMDR pairs for each mode. Once modal frequency and EMDR pairs are obtained for each time-domain method, these results are combined based on the least common multiple of the number of estimates. The three time-domain methods are equally treated. Predominant frequencies can therefore be picked from those frequency components at peaks, which represents the frequency component with the most population. Both frequency and EMDR estimates are obtained by averaging all estimates in predominant frequency ranges. Final results are then compared to EFDD estimates for verification.

The suggested process to arrive at a single estimate for modal frequency and EMDR for a building during a seismic event is summarized in the following steps. The next few paragraphs will illustrate this process for LA-52 building subjected to La Habra event on 28th of March 2014 (information was obtained from CSMIP[1]). In the next section, estimates of modal properties for various buildings are obtained using the suggested process using CSMIP data and equations for first mode properties based on building height, occupancy, and excitation amplitude are suggested.

1. Use time-domain system identification methods (i.e.ERA-OKID, SRIM, N4SID) to identify modal property pairs as a function of *N* and *p*.

2. For data generated in step 1, select pairs of modal properties whose EMDR is between 0.5% and 20% for each time-domain system identification method.

3. Combine the data from step 2 and identify the statistical modes of natural frequencies in the combined population of estimated pairs of frequency and EMDR (i.e. peaks in the histogram of estimated frequencies).

[1] The Center for Engineering Strong Motions Data via California Strong Motion Instrumentation Program, https://strongmotioncenter.org/

4. Find the average of modal frequency and EMDR values in the range between 0.9 and 1.1 times each peak estimate of natural frequency computed in step 3. The population located in this range covers a sizable portion of the probability mass located under each peak for all cases investigated. These are the estimated modal properties for the building in the seismic event.

5. Verify modal properties suggested in step 4 using the EFDD method.

Figure 2-1 illustrates the first step in our proposed technique for computing modal properties for a given building; the figure is developed for LA-52 building during the La Habra event on 28th of March 2014. Figure 2-1a shows the results obtained using the SRIM method to show the variation in identified frequencies and EMDR for model order and time length (stacked data layer); other time-domain system identification methods would result in similar plots (see Figure 2-1b). Model order and stacked layer are two factors controlling the estimate of system matrices from the state-space model, and different sets of factors lead to different realizations of system matrices and, therefore different estimates of frequency and EMDR. Since different combinations of model order and stacked layer leads to different estimate, a stable zone is defined in which variations of modal properties are reasonable. The stable zone is defined according to the data computed for EMDR; all modal property pairs (i.e., frequency and EMDR) with 0.5% < EMDR < 20% are kept since the unrealistically low (or high) damping ratio indicates a spurious mode. The modal property values in the stable zones (plural for each mode) are taken to represent an overall estimate of frequency and EMDR for the SRIM method (i.e. step 2).

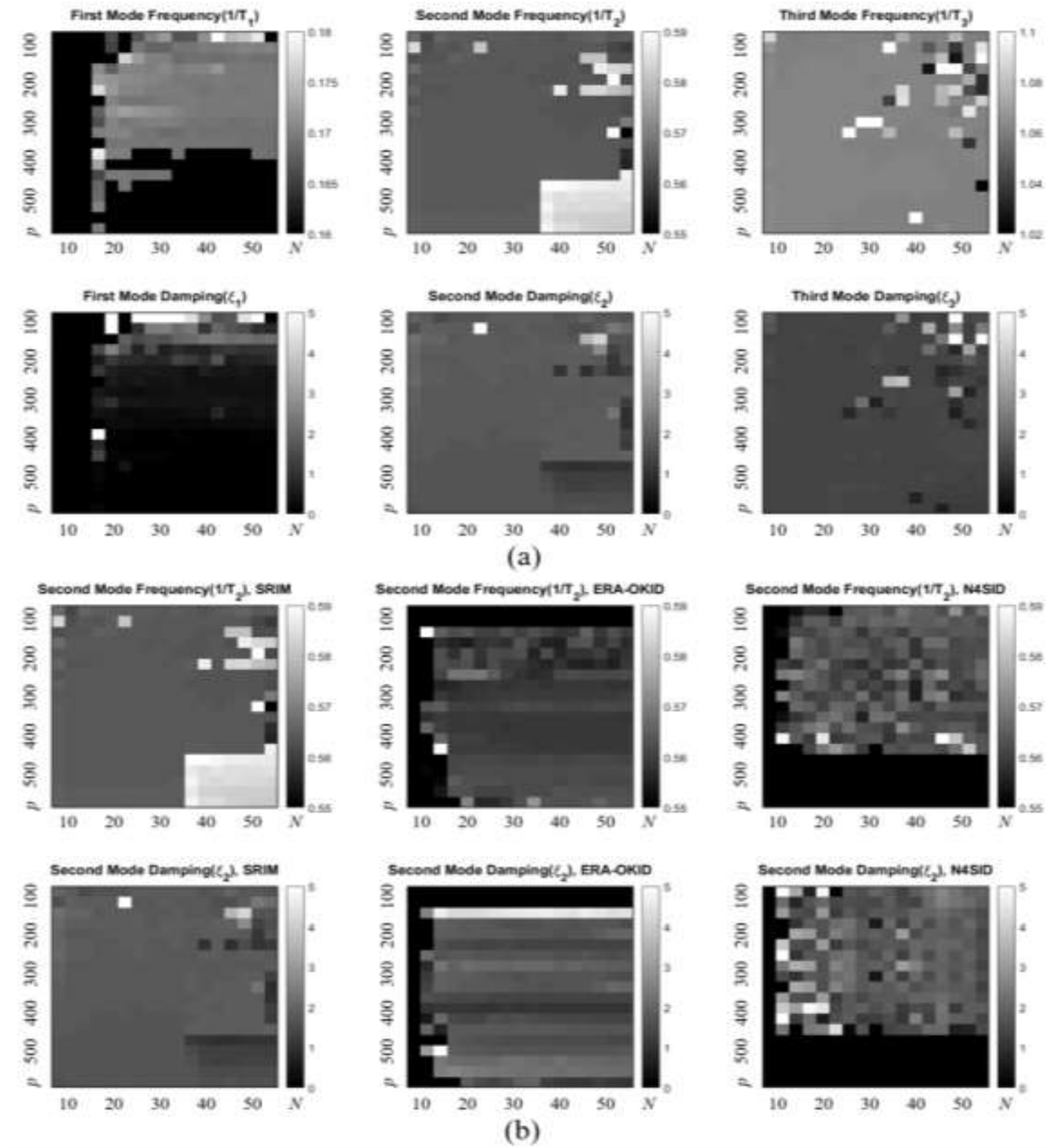

Figure 2-1. (a) Frequency and EMDR estimates of first three modes from SRIM method for building LA-52 subjected to La Habra, 28Mar 2014; (b) Frequency and EMDR estimates of the second mode from three time-domain method for building LA-52 subjected to La Habra, 28Mar 2014

In step 3, the stable estimates of modal properties obtained from each of the three time-domain system identification method are combined to arrive at a single set of modal properties.

Figure 2-2 shows the histogram of estimated frequencies for LA-52 during the La Habra event (shown with gray bars). The histogram represents the population of each frequency component; frequencies up to the fourth mode of vibration are indicated in the figure. We assume that the histogram of frequencies shows peak values of the population at frequencies close to the ‘true’ value of modal frequencies of LA-52 building during the La Habra event. Results show that the building’s vibration has been mostly in flexural mode (Chopra, 2016; Bernal et al., 2012). In step 4, an average of modal frequencies and EMDR for a range between 0.9 to 1.1 times the peak estimate of modal frequencies is computed and suggested as modal properties of LA-52 during the La Habra event. In Figure 2-2, these values are printed near the peaks at the first line, and the coefficients of variation for each estimate is given at the second line. Mode shapes are plotted with dash lines at their respective frequencies. In step 5, the results obtained from the combined time-domain method are compared to those obtained from the EFDD method for verification shown with solid black lines.

2.3 DATA COLLECTION AND DESCRIPTION

At the time of conducting this study, the CSMIP database of instrumented buildings contains structural records from more than 561 events in the general California crustal area. For the research study presented herein, 80 buildings with a total of 896 distinct seismic event and building direction records are selected from the CSMIP database. The selected buildings include Steel and Reinforced Concrete Moment Resisting Frames (i.e., SMRF, and RCMRF), Reinforced Concrete Walls (RCW), Concentrically Braced Frames (CBF), and Eccentrically Braced Frames (EBF). The distribution of the CSMIP instrumented buildings used in this study is presented in Figure 2-3. Among the 80 buildings used in this study, there are 25 SMRF, 11 RCMRF, 30 RCW, 11 CBF, 3 EBF buildings with 214, 123, 380, 145 and 34 distinct seismic events and building direction records.

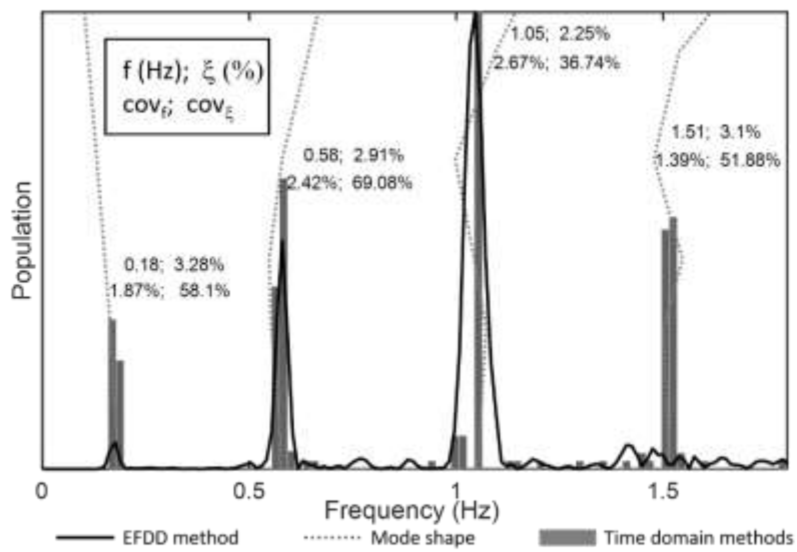

Figure 2-2. Frequency and damping estimates for each mode based on the combined System ID for building LA-52 (#24602) subjected to La Habra, 28Mar 2014

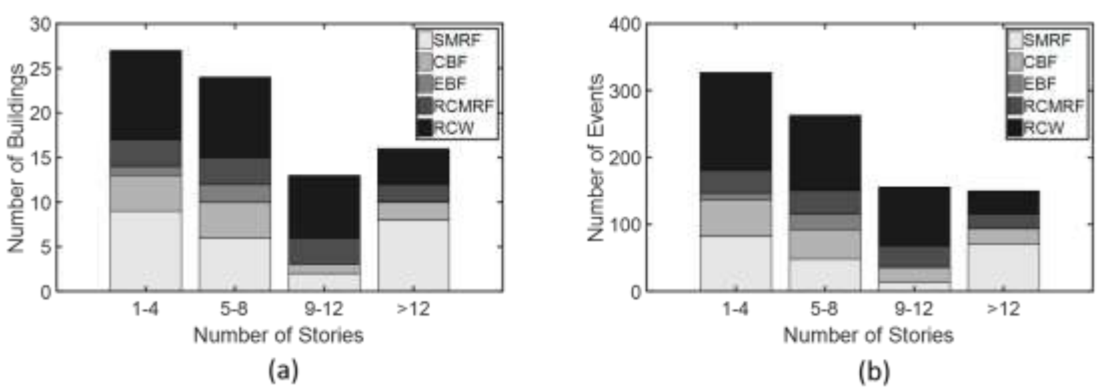

Figure 2-3. Information about the dataset of building responses used in this study

2.4 EQUATIONS FOR NATURAL PERIODS AND DAMPING RATIOS

We have utilized our suggested combined system identification technique to quantify modal properties for the 896 distinct seismic events and building directions; we have used these estimates to form a set of meaningful and practical equations for natural periods and EMDRs based on structural system types, building height and other factors that may prove to be significant. Multivariate regression analysis is utilized to fit the stable modal properties to expressions in either linear function or power function with building heights, building occupancy, and ground motion intensity measures being considered as predictors. The goodness of fit is measured through hypothesis testing that utilizes the t-test and F-test. A T-test analyzes if the inclusion (or exclusion) of one predictor will significantly affect the performance of the statistical model, while an F-test analyzes if the overall model containing multiple predictors successfully explains the source of data variance. The results of the hypothesis testing will be examined by *p-values*. A *p-value* less than the significance level (i.e., 0.05) is considered significant in this study.

A preliminary model investigation was performed before the statistical model is built. Automatic search procedure, including Best Subsets algorithm and Stepwise Regression method, serves to select the most proper set of predictors without evaluating all the possible combinations (Kutner, 2005). Five criteria for model selection were utilized: coefficient of determination (R^2); adjusted $R^{2,}$ which penalizes model complexity, mean of squared errors (*MSE*), *Mallow's Cp* and *PRESSp*. More details with respect to the model selection criteria can be found in Appendix A of the paper. Best Subsets regression is a rather simple and straightforward method that identifies the 'best' regression model containing a certain number of predictors with respect to a specified criterion; and stepwise regression automatically adds or removes individual predictors step by step according to p-values. The model with the most suitable set of predictors is then examined by hypothesis tests.

The accuracy of the regression model was examined before any inference is undertaken.

Diagnostics involving residuals were considered, including tests for normality, test for constancy, lack of fit test and test for outliers. For identification of outlying observations, *Hat Matrix Leverage values*, *Studentized Deleted residuals*, *DFFITS* and *Cook's Distance* (more details with respect to the outlier detection methods can be found in Appendix A of the paper). are calculated, and the corresponding T-tests or F-tests are employed. Remedial measures are then carried out when diagnostics demonstrate that the regression model is not appropriate enough for the data. For the non-normality of error terms, *Box-Cox Transformation* that transforms the shape and the spread of the distribution of response to correct the skewness of the distribution of error terms is utilized. *IRLS* robust regression is also employed in this study using weights that vary inversely with the magnitude of scaled residuals. Several iterations were required to keep to properly revise the weights until convergence criteria is satisfied. Final estimates reported in this study are based on the results after taking the remedial measures.

2.5 MODAL PROPERTIES FOR SMRFs

Dynamic properties of 25 SMRF buildings representing 195 building-events were computed using the suggested system identification technique. Building height ranges from 26 ft to 693 ft, *PG*A ranges from 0.004g to 0.3g, *PGV* ranges from 0.19cm/s to 24.40 cm/s, and *PGD* ranges from 0.008cm to 12.64cm. The buildings were divided into two subcategories as far as occupancy is concerned: (1) Residential, office and commercial buildings, (2) Hospitals. Our recommended regression equation for estimating the fundamental period, and first mode EMDR of SMRF buildings is given in Eq. 2-1, and Eq. 2-2, respectively; units are: T_1(sec), *PGV* (cm/sec), *H*(ft). Comparison of regression results for fundamental period of SMRFs at *PGV* = 10cm/s and ASCE-7 formula are shown in Figure 2-4(a). The 95% confidence and prediction intervals for the damping regression equation are presented in Figure 2-4(b).

$$T_1 = \begin{cases} 0.017H^{0.82}PGV^{0.06} & Hospital \\ 0.026H^{0.82}PGV^{0.06} & other \end{cases}$$ Eq. (2-1)

$$\xi_1 = 8.86H^{-0.16} \qquad 25' \leq H \leq 700' \;\&\; PGV$$ Eq. (2-2)

$$\leq 20cm/s$$

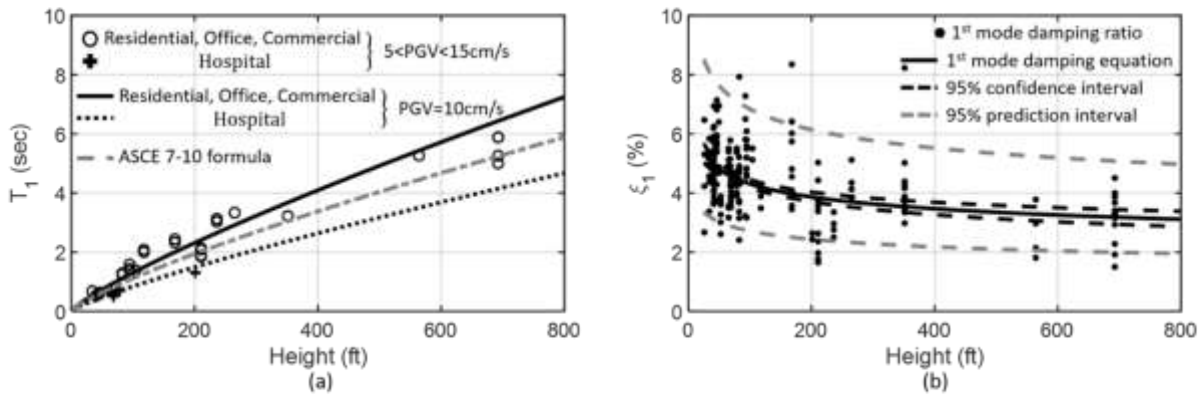

Figure 2-4. (a) Fundamental period for SMRF buildings regressed on Height vs. ASCE-7 formula, (b) 95% confidence and prediction range for first mode EMDR of SMRFs.

2.6 MODAL PROPERTIES FOR RCMRFs

Dynamic properties of 11 RCMRF buildings representing 123 building-events were computed using the suggested system identification technique. Building height ranges from 30 ft to 169 ft, *PGA* ranges from 0.003g to 0.45g, *PGV* ranges from 0.16cm/s to 54.90 cm/s, and *PGD* ranges from 0.008cm to 13.78cm. Our recommended regression equation for estimating the fundamental period, and first mode damping of RCMRF buildings is given in Eq 2-3 and 2-4. Comparison of regression results for T_1 at PGV=10cm/s and ASCE-7 formula are shown in Figure 2-5(a).

$$T_1 = 0.01H^{1.0}PGV^{0.12}$$ Eq. (2-3)

$$\xi_1 = 3.89H^{-0.16} \qquad 30' \leq H \leq 165' \;\&\; PGV \leq 50cm/s$$ Eq. (2-4)

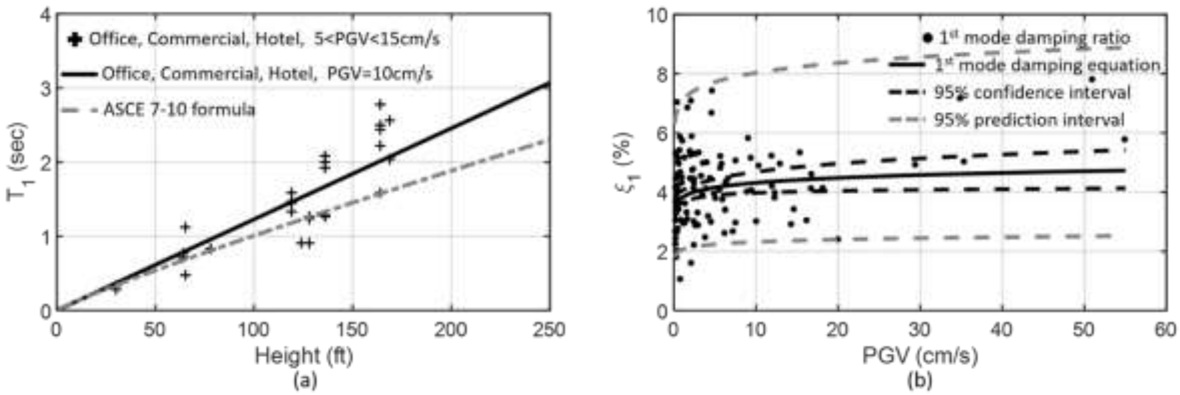

Figure 2-5. (a) Fundamental period for RCMRF buildings regressed on Height vs. ASCE-7 formula, (b) 95% confidence and prediction range for first mode EMDR of RCMRFs.

2.7 MODAL PROPERTIES FOR RCWs

Thirty RCW buildings with heights ranging from 28 ft. to 230 ft representing 336 building-events were used for quantifying their dynamic properties. *PGA*, *PGV*, and *PGD* range from 0.001g to 0.8g, 0.062cm/s to 112.14 cm/s, and 0.003cm to 28.3cm, respectively. The buildings were divided into two subcategories: (1) Library, Residential, Office, Hotel, Commercial buildings and Parking Structures, and (2) Schools and Hospitals. Recommended equations for first mode properties are given in Eq 2-5 and 2-6 Comparison of regression results for *PGV*=10cm/s and ASCE-7 formula is shown in Figure 2-6(a). The 95% confidence and prediction intervals for the equation presented for first mode EMDR are presented in Figure 2-6(b).

$$T_1 = \begin{cases} 0.009H^{0.87}PGV^{0.02} & School/Hospital \\ 0.013H^{0.82}PGV^{0.02} & other \end{cases}$$ Eq. (2-5)

$$\xi_1 = 5.06H^{-0.08} \qquad 25' \leq H \leq 200' \;\&\; PGV \leq 100cm/s$$ Eq. (2-6)

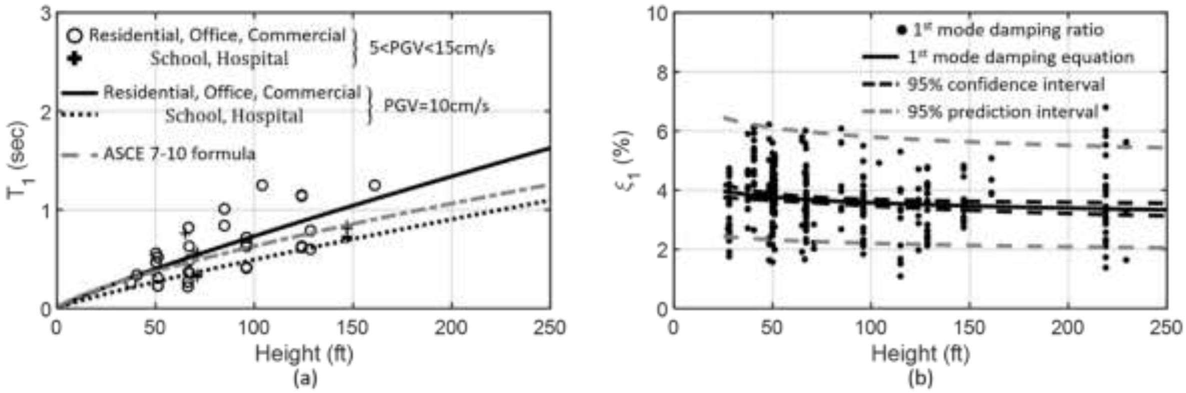

Figure 2-6. (a) Fundamental period for RCW buildings regressed on Height vs. ASCE-7 formula, (b) 95% confidence and prediction range for first mode EMDR of RCWs.

2.8 MODAL PROPERTIES FOR CBFs

Dynamic properties of 11 CBF buildings representing 144 building-events were computed; 32 ft < H < 716 ft, 0.001g < PGA < 0.33g, 0.001 cm/s< PGV < 29.64cm/s, and 0.003cm < PGD < 9.81cm. The buildings were divided into two subcategories: (1) Industrial, Office, Commercial buildings and Parking Structures, and (2) Jails and Hospitals. The recommended equations for first mode properties of CBF buildings is given in Eq 2-7 and 2-8 Comparison of regression results and ASCE-7 formula is shown in Figure 2-7(a). The 95% confidence and prediction intervals for the equation presented for first mode EMDR are presented in Figure 2-7(b).

$$T_1 = \begin{cases} 0.005H^{1.02} & Jail/Hospital \\ 0.007H^{1.02} & other \end{cases} \qquad \text{Eq. (2-7)}$$

$$\xi_1 = 3.37 \qquad 30' \leq H \leq 700' \;\&\; PGV \leq 30cm/s \qquad \text{Eq. (2-8)}$$

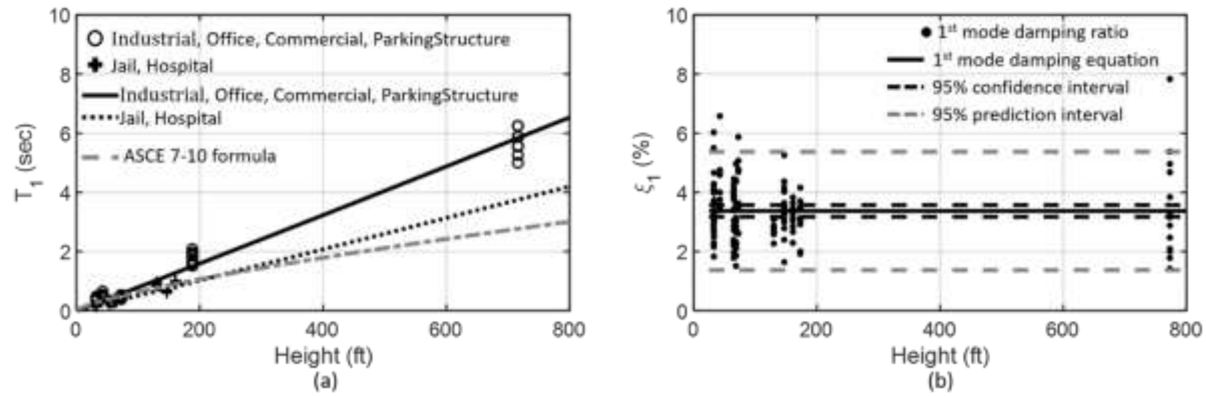

Figure 2-7. (a) Fundamental period for CBF buildings regressed on Height vs. ASCE 7-10 formula, (b) 95% confidence and prediction range for first mode equivalent damping of CBF

2.9 MODAL PROPERTIES FOR EBFs

3 EBF buildings representing 34 building-events were used to generate equations for their fundamental period and first modal damping; see Eq 2-9 and 2-10 Building height ranges from 25 ft to 134 ft, *PGA* ranges from 0.005g to 0.117g, *PGV* ranges from 0.152cm/s to 17.563 cm/s, and *PGD* ranges from 0.014cm to 4.989cm. All the EBF buildings in this database are hospital building structures. Comparison of regression results and ASCE-7 formula are shown in Figure 2-8(a). The 95% confidence and prediction intervals for the equation presented for first mode EMDR are presented in Figure 2-8(b).

$$T_1 = 0.07H^{0.460}PGV^{0.04} \quad \text{Eq. (2-9)}$$

$$\xi_1 = 6.43H^{-0.13} \qquad 25' \leq H \leq 150' \ \& \ PGV \leq 20cm/s \quad \text{Eq. (2-10)}$$

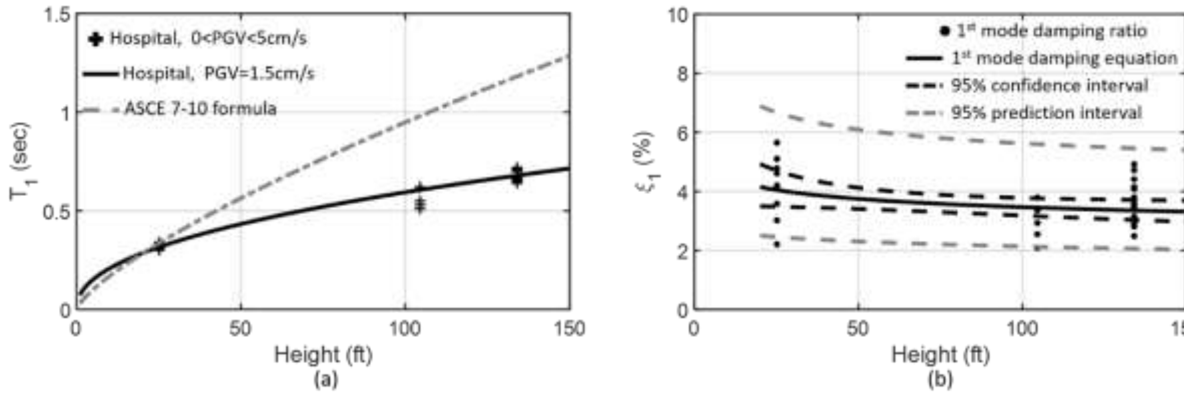

Figure 2-8. (a) Fundamental period for EBF buildings regressed on Height vs. ASCE-7 formula, (b) 95% confidence and prediction range for first mode equivalent damping of EBF

2.10 COMPARISON WITH PREVIOUS RESEARCH

Variation in EMDR with building height has been studied by other researchers (e.g. Fritz *et al.*, 2009 who uses building data from US, Japan and UK; Satake *et al.*, 2013 who uses building data from Japan; Bernal *et al.*, 2015 who uses building data from California; Cruz *et al.*, 2016 who uses building data from California) and their work provides recommendations for EMDR for a combination of mid-rises and high-rises, and steel and concrete buildings. Figure 2-9(a) and Figure 9(b) compare the results of this study with what was suggested by other investigators for steel buildings and concrete buildings, respectively.

All concrete buildings investigated in this study have heights of less than 250ft. As shown in Figure 2-9(b), estimates of EMDR in this study for concrete buildings accord with those proposed by other researchers. Satake *et al.* (2013) underestimate EMDR for concrete buildings taller than 100ft since the majority of their database consist of low amplitude ground motion excitations.

For midrise steel buildings (height<200') illustrated in Figure 2-9(a), identified damping ratios in this study agree with few other investigations. Damping ratio estimate proposed by ATC-72-1 can be considered a lower bound, while that proposed by Cruz *et al*. (2016) can be considered a higher bound. For high-rise steel buildings, however, this study has a higher estimate of EMDR compared with other estimates; on average EMDR = 3.2% is suggested by this study compared to the recommendation from other researches which has an average of less than 2%. To identify the source of this difference, a case study is conducted to understand the significance of EMDR for high-rise steel buildings with respect to signal reconstruction. We aim to demonstrate that the response of a tall building is relatively insensitive to the value of EMDR; therefore, estimates of EMDR for tall buildings is subjected to high variability.

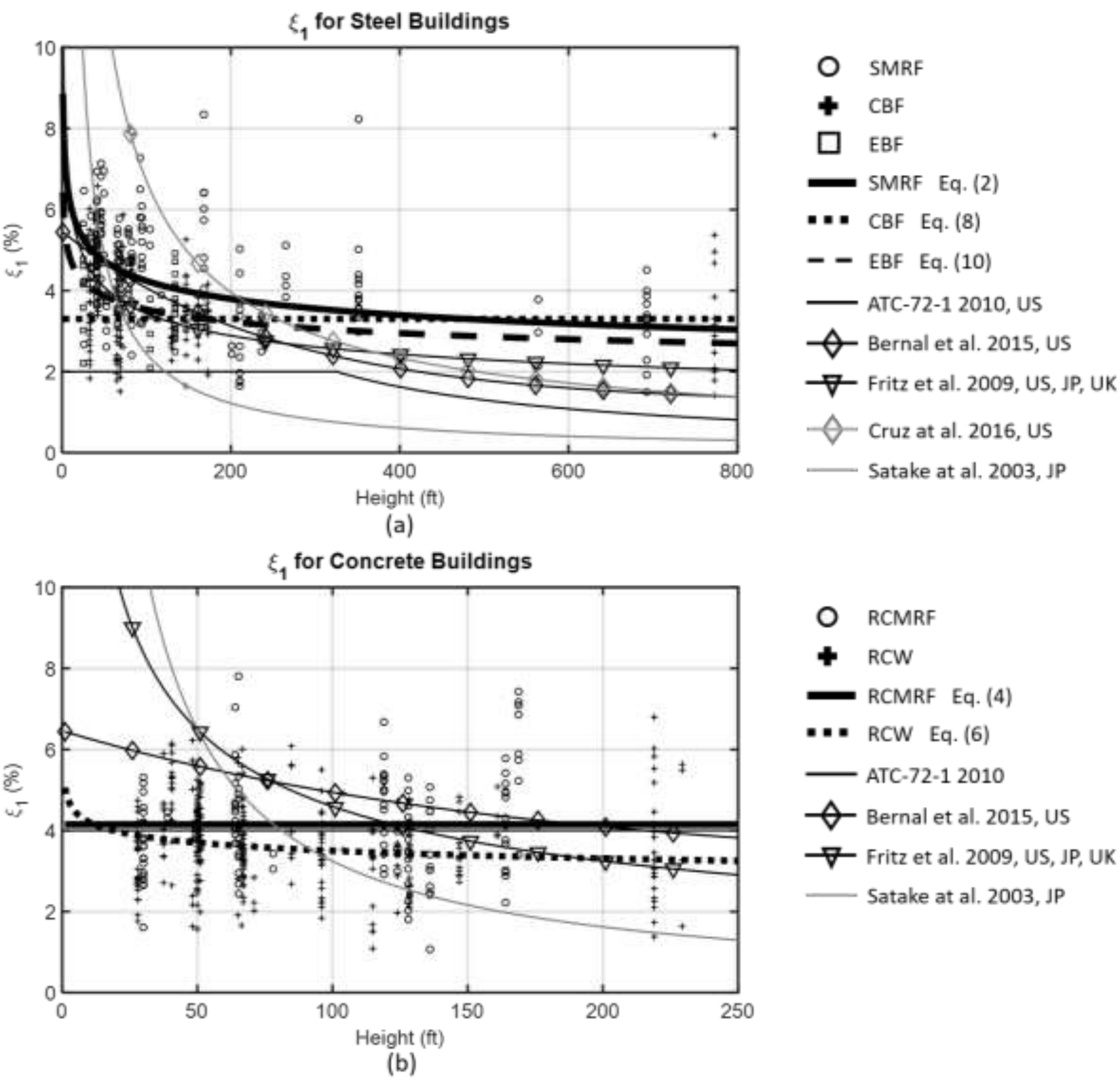

Figure 2-9. (a) First mode damping ratio versus height for steel buildings estimated in this study compared to other researches. (b) First mode damping ratio versus height for concrete buildings estimated in this study compared to other researches.

Cruz *et al.* (2016) proposed an objective function minimization method to estimate modal frequencies, EMDRs, and mode shapes. Their suggested objective function is based on acceleration measurements by sensors on the building; it is defined as the sum of the squared difference between predicted and measured relative acceleration, normalized by the sum of squared measured relative acceleration at each floor (See Eq.2-11, where θ denotes parameters such as periods, EMDRs and mode shapes; i represents time samples; and j represents the number of sensors on the building; $\ddot{\hat{u}}_j$ stands for the predicted acceleration of the j^{th} sensor; and $\ddot{u}_j$ stands for the recorded acceleration of the j^{th} sensor). This method assumes that acceleration response is a linear combination of the response of several single degrees of freedom. A simplified model of the building is utilized to compute the initial point for the algorithm, and the predicted values of acceleration are obtained via modal combination. The algorithm cannot guarantee modal orthogonality.

$$J(\theta) = \sum_{j=1}^{N_{sen}} \sum_{i=1}^{\tau} \frac{[\ddot{u}_j(i\Delta t) - \ddot{\hat{u}}_j(i\Delta t)]^2}{\sum_{k=1}^{\tau}[\ddot{u}_j(k\Delta t)]^2} \qquad \text{Eq. (2-11)}$$

Using first three modal frequencies, EMDRs, and mode shapes obtained from the recommended system identification technique in this study along with a linear combination of modal response in the time domain, the reconstructed signals are compared with measured signals as illustrated in Figure 2-10. Northridge earthquake, 17Jan, 1994 is used in this case and the corresponding EMDR estimates are 2.47%, 2.41% and 2.21% for the first three modes. As the estimate of the first mode EMDR for LA-52 varies between 1.7% and 7.7% (at different events), the sensitivity of acceleration response to first mode EMDR for LA-52 subjected to the Northridge earthquake is analyzed by reducing the identified first mode EMDR by a factor of 2 (EMDR = 1.2% damping that is close to the value proposed by Cruz *et al*., 2016), and increased by a factor of 2 (using EMDR = 5%). EMDR at second and third mode is kept as estimated (i.e. 2.41% and 2.21%, respectively). We demonstrate how such large variability in the first mode EMDR may affect the difference between the reconstructed and measured acceleration signal at the roof and 35th floor of the LA-52 building during the Northridge excitation.

As shown in Figure 2-10, the first mode EMDR reduced or increased by a factor of 2 has almost no effect on the reconstructed signal. Reconstructed signal, however, for cases with all three EMDR values magnified (or reduced) by a factor of two show some difference (results not shown here). As shown in Figure 2-10, regardless of EMDR for the first mode, the reconstructed signal at the roof level overestimates the measured signal, especially during the time with intense excitation. In the 35th floor, no significant discrepancy is observed among three different damping ratios, and all three 35th floor level signal reconstructions match relatively well with the sensor measurements.

It can be shown that the damping ratio is not the only factor affecting signal reconstruction. The poor match, in some cases, may stem from the assumptions made in the signal reconstruction process. Energy dissipation in structures is a rather complex physical phenomenon, combined with viscous damping, frictional damping and nonlinear behaviors of structural elements. Explaining different sources of energy dissipation by equivalent viscous damping along with a linear combination of predominant modes leads to some level of inaccuracy. Besides, the sparsity of sensor placement, especially in tall buildings, could be an issue for system identification techniques, for example, sensors are only implemented at 6 stories out of 52 stories in building LA-52.

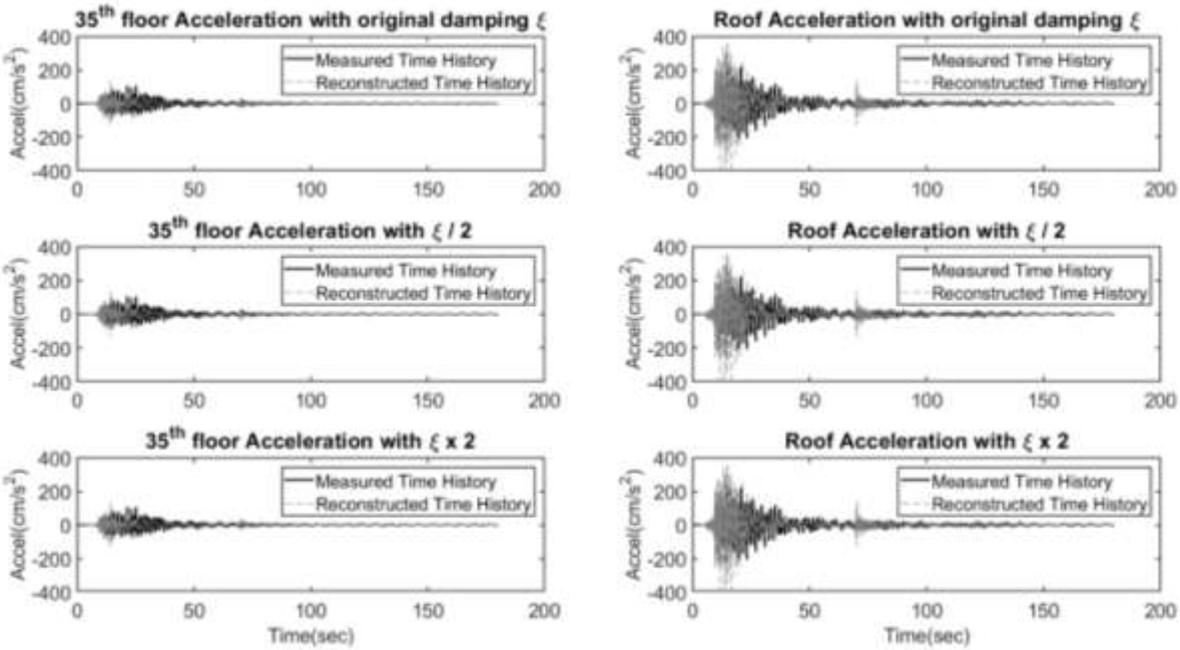

Figure 2-10. Reconstructed Acceleration and measured acceleration for CBF building LA-52 subjected to Northridge, 17Jan, 1994, with original damping estimate compared with damping reduced and increased by a factor of 2

To further study the significance of the damping ratio of the first mode, especially in tall buildings, SDOF response of the first three modes of the LA-52 building to two forms of base excitation is analyzed. For a tall building with a long first mode period (e.g., longer than 4sec), there are cases that the frequency content of certain ground motions cannot excite the first mode; therefore, the acceleration response of the first mode SDOF is insensitive to the corresponding damping ratio. Moreover, the objective function (Eq. 2-11) inherently favors matching the high-frequency range, therefore, damping ratios of high-frequency modes are weighted more than that of low frequency. In contrast, displacement response is sensitive to damping in low-frequency regime and may indicate that an appropriate method for detecting the first mode of a tall building is to use an objective function in terms of displacement records while acceleration records shall be used to detect higher modes. The use of an acceleration-based objective function desensitizes the first mode damping ratio and the obtained results might not be as reliable as those of higher modes.

To illustrate the inherent bias of an acceleration-based objective function for detecting modal damping, we resort to a simple thought experiment. Consider function J, shown in Eq. 2-12, that measures the normalized difference between the damped acceleration response and undamped (ξ=0) acceleration response of an SDOF system to base excitation. Eq. 2-12 is similar in format to Eq. 2-11; while in Eq. 2-11 the error stands for the difference between recorded and computed data, in Eq. 2-12 the error stands for the difference between damped response and undamped response. J is bounded between 0 to 1; J close to 0 indicates that the damped response has little difference compared to the undamped response, (i.e., response is insensitive to EMDR), and a J value close to 1 indicates the damped and undamped responses are significantly different. Figure 2-11(a) illustrates the value of J at various EMDR values for the Northridge ground motion record at LA-52 building; results for SDOFs representing the first three modes of vibration of LA-52 with 0.0 ≤ EMDR ≤ 10.0 are illustrated. For an SDOF system with a period identical to that of the first mode of LA-52, EMDR is a trivial factor and has little impact on its acceleration response (i.e., low values of J). For SDOF systems representing higher modes, small EMDRs (i.e., <2%) are where response shows the largest sensitivity, while in higher EMDRs there is no significant difference in acceleration response when different damping ratios are utilized. A similar pattern can be found in all seven ground motion records of LA-52 except for the recording during the Landers Earthquake in which the first mode is not excited (Cruz *et al.*, 2016). To analyze how the frequency contents of input excitation affect the acceleration response, a white noise excitation is applied to the three SDOF systems and Eq. 2-12 is similarly investigated–see Figure 2-12(b). Figure 2-12(b) shows that subjected to a white noise input that has a uniform frequency content, SDOFs with large periods are still insensitive to EMDR. The response of SDOFs with smaller periods is highly affected by EMDR, especially when this value is small (<5%). This finding is in accordance with the illustrations in Chopra (2016) where SDOF systems with various EMDRs are subjected to the El Centro ground motion. It is demonstrated that the spectral acceleration for natural periods longer than 3 sec. is insensitive to EMDR.

$$J(\xi) = \frac{\sum_{i=1}^{N}[\ddot{u}_{\xi=0}(i\Delta t) - \ddot{u}_{\xi}(i\Delta t)]^2}{\sum_{i=1}^{N}[\ddot{u}_{\xi=0}(i\Delta t)]^2} \qquad \text{Eq. (2-12)}$$

2.11 CONCLUSION AND FUTURE WORK

A system identification technique is suggested to assess the modal properties of buildings during seismic excitation. The suggested technique borrows the advantages of three time-domain and one frequency-domain system identification method (i.e., SRIM, ERA-OKID, N4SID; and EFDD). When three time-domain methods generate a total distribution of estimates of modes, the EFDD method rules out the fictitious modes by using spectral analysis. Using this technique, we estimated the modal properties of 80 buildings with a total of 896 distinct seismic events and building direction records from the CSMIP database. The identified modal properties are mainly from the linear response of buildings and are not plagued by the short time instances in which few cases within the dataset moved into minor nonlinear behavior due to the nature of the utilized system identification methods and remedial statistical measures. Using the identified modal properties, we have developed simple and practical equations for natural periods and EMDRs based on structural system types, building height, and other factors that prove to be significant. In general, a decreasing trend of the first mode damping ratio with an increase in building height can be observed. In some cases (i.e., RCMRF), the damping ratio is amplitude (PGV) dependent. The results of EMDRs estimated by the recommended system identification technique are in high agreement with those of other researches for low-rise steel buildings, even though a high uncertainty level could be an inevitable issue in damping estimation. For concrete buildings, although a decreasing trend is also observed in this study, damping ratio estimates for buildings shorter than 50 ft are lower than those from other researches. For tall buildings, the first mode EMDR is an insensitive factor with respect to acceleration response.

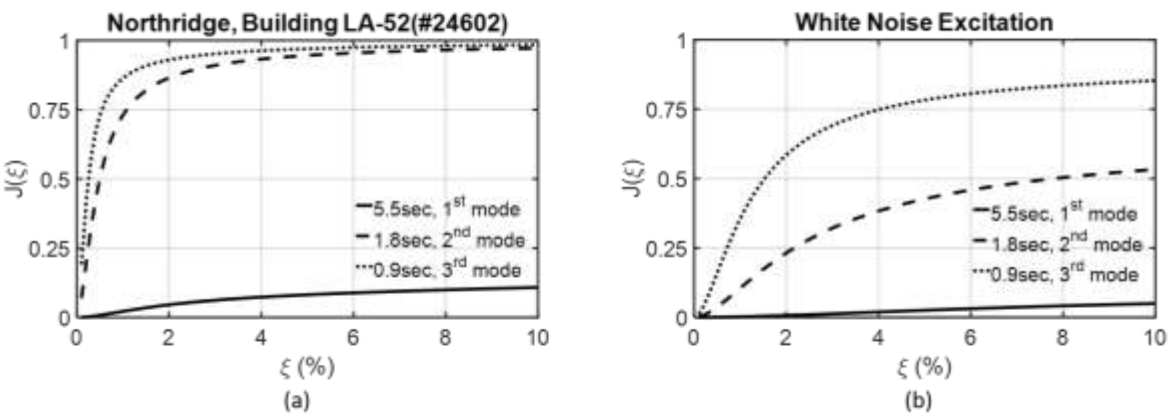

Figure 2-11. First three modes of J vs. ξ for CBF building LA-52 subjected to (a) Northridge, 17Jan, 1994, (b) White noise excitation

The EMDR discussed in this study is based on the assumption that energy dissipation in structures has a viscous nature. Given the inaccuracy and insufficiency of velocity-dependent viscous damping, frictional or amplitude-dependent damping has caught researchers' attention. Spence and Kareem (2013) have proposed a joint probability density function to explain the distribution of vibration amplitude and slip force for frictional dampers. In light of their work, it is suggested that a more detailed model is needed to represent the energy dissipation in structural systems and replace the modal damping model for nonlinear response history analysis. One suggestion for such model can be a damping element comprising a viscous damper and a frictional damper to be located at each story of the structural model of a building. The frictional damping is used to capture the friction and slippage between surfaces of structural members.

This model can be calibrated with real data to arrive at validated modeling parameters. The suggested damping element exhibits displacement-dependent energy dissipation characteristics and can provide more accurate quantification of internal forces and deformations in the response of buildings and exposed to dynamic excitations (Xiang and Zareian, 2018).

2.12 REFERENCES

ATC, 1978. Tentative provisions for the development of seismic regulations for buildings. *Rep. No. ATC 3-06*, Applied Technological Council, Palo Alto, Calif.

ATC, 2010. Modeling and acceptance criteria for seismic design and analysis of tall buildings. *PEER/ATC-72-1*, Applied Technology Council in cooperation with the Pacific Earthquake Engineering Research Center, Redwood City, CA.

ASCE-American Society of Civil Engineers, 2017a. *Seismic Evaluation and Retrofit of Existing Buildings* (ASCE/SEI 41–17). American Society of Civil Engineers: Reston, VA.

ASCE-American Society of Civil Engineers, 2017b. *Minimum Design Loads for Buildings and Other Structures* (ASCE/SEI 7–10). American Society of Civil Engineers: Reston, VA.

ASCE-American Society of Civil Engineers, 2010. *Minimum Design Loads for Buildings and Other Structures* (ASCE/SEI 7–10). American Society of Civil Engineers: Reston, VA.

Bentz, A., & Kijewski-Correa, T., 2008. Predictive models for damping in buildings: the role of structural system characteristics. In *Proceedings of the 2008 Structures Congress, 18th Analysis and Computation Specialty Conference, Vancouver, Canada*.

Bernal, D., Kojidi, S., Kwan, K., Döhler, M. (2012). Damping Identification in Buildings from Earthquake Records. *SMIP12 Seminar Proceedings*, 2012.

Bernal, D., Döhler, M., Kojidi, S., Kwan, K, & Liu, Y., 2015. First mode damping ratios for buildings. *Earthquake Spectra*, **31**(1), 367-381.

Chopra, A. K., 2016. Dynamics of Structures: Theory and Applications to Earthquake Engineering. Fourth Edition.

Cruz, C., Miranda, E., 2016. Evaluations of damping ratios for the seismic analysis of tall buildings. *ASCE Journal of Structural Engineering*, **143**(1).

Davenport, A. G., & Hill-Carroll, P., 1986. Damping in tall buildings: its variability and treatment in design. In *Building motion in wind*, p. 42-57. ASCE.

Fang, J. Q., Jeary, A. P., Li, Q. S., & Wong, C. K., 1999. Random damping in buildings and its AR model. *Journal of Wind Engineering and Industrial Aerodynamics*, **79**(1), 159-167.

Federal Emergency Management Agency (FEMA), 2012. *Seismic Performance Assessment of Buildings Volume 1 – Methodology, Tech. Rep. P-58-1*, Washington, D.C.

Fritz, W. P, Jones, N.P., & Igusa, T., 2009. Predictive models for the median and variability of building period and damping. *Journal of Structural Engineering*, **135**(5), 576-586.

Goel, R., & Chopra, A.K., 1997. "Period formulas for moment-resisting frame buildings". *Journal of Structural Engineering*; **123**(11): 1454 – 1461.Jeary, A. P., 1997. Damping in structures. *Journal of Wind Engineering and Industrial Aerodynamics*, 72: 345 – 55.

Juang, J. N., 1994. Applied System Identification, *Prentice-Hall*, Englewood Cliffs, New Jersey.

Kutner, M. H., Nachtsheim, C.J., Neter, J., & Li, W., 2005. *Applied Linear Statistical models*. Fifth Edition.

Le, T. H., & Tamura, Y., 2009. Modal Identification of ambient vibration structure using frequency domain decomposition and wavelet transform. *The Seventh Asia-Pacific Conference on Wind Engineering, Taipei, Taiwan.*

Li, Q. S., Liu, D. K., Fang, J. Q., Jeary, A. P., & Wong, C. K., 2000. Damping in buildings: its neural network model and AR model. *Engineering Structures*, **22**(9), 1216-1223.

Ljung, L., 1999. *System Identification: Theory for the User*, Upper Saddle River, NJ, Prentice-Hal PTR.

LATBSDC, 2018. *An Alternative Procedure for Seismic Analysis and Design of Tall Buildings Located in The Los Angeles Region.* Los Angeles Tall Buildings Structural Design Council.

Miranda, E., 1999. Approximate Seismic Lateral Deformation Demands in Multistory Buildings. *ASCE Journal of Structural Engineering*, Vol. 125, Issue 4.

PEER, 2017. *Guidelines for Performance-Based Seismic Design of Tall Buildings-ver. 2*, PEER Report 2017/06, prepared by the TBI Guidelines Working Group, Berkeley, CA.

Satake, N., Suda, K. I., Arakawa, T., Sasaki, A., & Tamura, Y., 2003. Damping evaluation using full-scale data of buildings in Japan. *Journal of structural engineering*, **129**(4), 470-477.

Spence, S.M.J., Kareem, A., 2014. Tall Building and Damping: A Concept-Based Data-Driven Model. *ASCE Journal of Structural Engineering*, Vol. 140, Issue 5.

Tamura, Y., & Yoshida, A., 2008. Amplitude dependency of damping in buildings. In *Proceedings of the 18th Analysis and Computation Specialty Conference* (Vol. 315).Van Overschee, P., & De Moor, B., 1994. N4SID: Subspace algorithms for the identification of combined deterministic-stochastic systems. *Automatica*, **30**(1), 75-93.

Wyatt, T. A., 1977. Mechanisms of damping. In *Proceeding of a Symposium of Dynamic Behavior of Bridges at the Transpor and Road Research Laboratory, Crowthorne, Berkshire, England, May 19, 1977*. (No. TRRL Rpt. 275 Proceeding).

Xiang Y, Zareian F., 2018. A damping element model for energy dissipation characterization in building structures. *Proceedings of the 11th National Conference in Earthquake Engineering,* Earthquake Engineering Research Institute, Los Angeles, CA.

2.13 APPENDIX A

R^2: Coefficient of Determination. It measures how much of the variation is reduced by the statistical model; in other words, how well the prediction can represent the observations.

R_{adj}^2: Adjusted Coefficient of Determination. It penalizes the Coefficient of Determination for model complexity, given the number of predictors used in the model.

MSE: Mean of squared errors. It measures the average squared difference between the predictions and the observations.

Mallow's Cp: It compares the precision of a full model with models including only a subset of the predictors.

PRESSp: Prediction Sum of Squares. It measures the fit of a model when certain observations are omitted; therefore it serves as a cross-validation analysis for the data.

Hat Matrix Leverage values: It measures the distance between a specific predictor and the mean of predictors. Therefore, it is used to identify outlying predictors.

Studentized Deleted Residuals: It measures the difference between observed response and studentized response when certain cases are deleted. Therefore, it is used to identify outlying response observations.

DFFITS: It measures the standardized change of fitted value when a certain case is excluded. Therefore, it provides an estimate of the influence on a single fitted value.

Cook's Distance: It is calculated by squaring, summing and standardizing the change of fitted values. Therefore, it provides an estimate of influence on all fitted values.

CHAPTER 3: CRITICAL ASSESSMENT OF ACCIDENTAL TORSION IN BUILDINGS WITH SYMMETRIC PLANS

3.1 INTRODUCTION

Seismic code provisions, such as ASCE 7-10 (ASCE, 2010) and ASCE 7-16 (ASCE, 2017), require that the effect of building torsion during seismic excitation is considered at each floor level. This torsion is comprised of two components: inherent torsion and accidental torsion. For all buildings, including symmetric-in-plan buildings where there are no inherent torsional effects, seismic codes require consideration of accidental torsion. Accidental torsion is considered by exerting the seismic equivalent lateral force of each floor at a distance equal to 5% of the building's plan dimension which is perpendicular to the direction of the applied equivalent lateral force from the center of mass (CM) of the floor diaphragm. Accidental torsion is intended to represent the effect of random discrepancies between the mass and stiffness distribution along with the height of the real building. For buildings with an asymmetric plan, accidental torsional moments are small compared with inherent torsional moments. However, accidental eccentricity is significant for symmetric-in-plan buildings.

There is a substantial body of research on quantifying the eccentricity that may represent accidental torsional moments in symmetric-in-plan buildings (De la Llera & Chopra 1992; 1994; 1995; Lin *et al.*, 2001; Hernandez & Lopez, 2004; De-la-Colina & Almeida, 2004; Basu *et al.*, 2014). In one of the most relevant studies, De la Llera and Chopra (1992) used recorded data from three buildings instrumented by the California Strong Motion Instrumentation Program (CSMIP) to conclude that the 5% eccentricity rule suggested by codes for consideration of accidental torsional moments is adequate. Their follow up study (De la Llera & Chopra, 1994; 1995) used single-story linear analytical models to show that 5% eccentricity is adequate for most steel and concrete Special Moment Resisting Frames (SMRFs). DeBock *et al*. (2014) compared the collapse capacities of buildings designed with provisions for accidental torsion to those designed without code provisions. They concluded that accidental torsion is significant and needed to be considered only when Torsional Irregularity Ratio (*TIR*, defined as the ratio of the maximum lateral displacement at the corner of a certain story to the average lateral displacement of the same story) is large.

This study utilizes multi-degree of freedom (MDOF) systems that are capable of nonlinear response with various heights to investigate if the 5% eccentricity rule is adequate to capture the effect of accidental torsion in buildings. Stiffness uncertainty is considered as the main source of torsional behavior in symmetric-in-plan buildings for this research study. In a perfectly symmetric building, the dynamic responses of two translational directions of the system are uncoupled. When asymmetric stiffness distribution takes place in a system with a nominally symmetric plan, translational ground motion triggers torsional vibration, amplifying deformations along the translational axes.

To consider the effect of uncertainty in stiffness of Vertical Lateral Load Resisting systems (VLLRs), a literature review is conducted to access the variability of element cross-section dimensions, second moment of inertia, and material strength. Ramsay *et al*. (1979) used Monte Carlo simulations to conclude that the deformation of reinforced concrete beams has a coefficient of variation of 0.14; De la Llera and Chopra (1994) suggest the same coefficient of variation for the stiffness of reinforced concrete elements. De la Llera and Chopra (1994) assumed that force distribution is deterministic (a conservative estimate). Ellingwood *et al* (1980) investigated probability-based load criterion and Melechers (1987) evaluated the reliability of structures, showing that the coefficient of variation is approximately 0.6 and 0.05 for Young's modulus and for section moment of inertia respectively. Bournonville *et al*. (2004) performed statistical analysis on mechanical properties of reinforcing bars and found that the coefficient of variation of the reinforcement's yield strength ranges from 0.03 to 0.09. ASTM A6-05 provides variability of structural element dimensions, and ASTM A992-04 provides steel and concrete material strength. According to these ASTM sources, section depth and width has a coefficient of variation (COV) ranging from 0.01 to 0.04, and column steel (Grade 50) yield stress has a COV of 0.05. Based on the information provided above and using 10,000 realizations of sections dimensions, the coefficient of variation for section moment of inertia is in the range of 0.06 to 0.12; these estimated are based on the following assumptions: 1) COV of section width and depth is set to 0.025, and 2) correlation coefficient between section width and depth ranges between 0 and 1. Given that the coefficient of variation of Young's modulus is approximately 0.06, the coefficient of variation values for the stiffnesses of all structural elements are conservatively set to be 0.14. This value acts as a good proxy for representing the coefficient of variation of concrete members but slightly overestimates the coefficient of variation for steel members. Since the implementation of stiffness uncertainty in this study does not differentiate between concrete and steel materials, a coefficient of variation value of 0.14 serves as an upper limit which yields conservative results.

Translational and torsional modes of vibration affect the general behavior of a building. To capture this in a parametric form, a factor Ω, which is the ratio of the dominant translational period to the dominant rotational period, is introduced. Large Ω values are associated with perimeter frame buildings with large torsional stiffness while small Ω values represent buildings, such as core-wall systems, with low torsional stiffness. Realistic values for Ω, ranging from 1.1 to 2.0, are investigated in this study and is informed by a database of instrumented buildings from California

Strong Motion Instrumentation Program (CSMIP).

3.2 METHODOLOGY

The goal of this study is to quantify the eccentricity factor that represents an accidental torsional moment in buildings due to randomness in VLLR stiffness. Parameters that characterize building torsional response (namely α_1 and α_2 which will be explained in the following section) are investigated. Statistics of these parameters are quantified using building models and ground motions considered in this study. This data is used to identify the equivalent eccentricity – represented by $e(\%)$ – from static pushover analysis when similar statistical measures (e.g., median and 84th percentile) are reached for each building model.

One of the most important parameters that affect torsional behavior of a building is Ω, the ratio of the dominant translational period (T_{tran}) to the dominant rotational period (T_{rot}); (Eq. 3-1). Ω values ranging from 1.1 to 2.0 for MDOFs are investigated in this study, which covers the range of values observed in real-world building scenarios.

$$\Omega = \frac{T_{tran}}{T_{rot}} \qquad \text{Eq. (3-1)}$$

3.2.1 Parameter Characterizing Building Torsional Response

The effect of torsional vibration is measured as the largest amplification in displacement among the four corners of each floor plan (i.e., rigid diaphragm assumption). Asymmetric stiffness distribution, due to randomness in stiffness of VLLRs, causes torsional vibration for a nominally symmetric system. The total response of a building subject to ground motion excitations is a combination of translational and rotational displacements. Given this background, two torsional vibration parameters are introduced (Eq.3-2, and Eq.3-3) to study the relative contribution of displacement response of each floor to torsional effects. In these equations, δ_{tran} is the maximum displacement of the floor solely due to translational vibration; δ_{rot} is similarly defined for torsional vibration. δ_{tran} and δ_{rot} are defined for buildings with an asymmetric distribution of stiffness due to randomness. δ_b denotes the displacement of a symmetric-in-plan base case system (i.e., symmetric with no randomness in VLLRs). α_1 is the ratio of peak total displacement of an asymmetric system to peak translational response of the base system. α_2 is the ratio of peak total displacement to peak translational displacement of the same asymmetric system. α_1 estimates the total displacement amplification due to stiffness eccentricity compared to a base case system, and it is a function of both translational response and rotational response. α_2 shows the displacement amplification within a certain asymmetric system, and it represents the contribution of rotational response to the total response. Note that α_1 and α_2 are random variables, therefore, statistical measures of these parameters (e.g., median and 84th) will be used to calculate equivalent eccentricity.

$\alpha_1 = \dfrac{max(\delta_{trans} + \delta_{rot})}{max(\delta_b)}$	Eq. (3-2)
$\alpha_2 = \dfrac{max(\delta_{trans} + \delta_{rot})}{max(\delta_{trans})}$	Eq. (3-3)

3.2.2 Equivalent Eccentricity from a Static Push-Over

To analyze the displacement amplification caused by eccentric static loading, equivalent lateral force is applied to each base system in two manners: 1) with eccentricity equal to *e*(%) to obtain the maximum floor deformation denoted as δ_p, and 2) with no eccentricity to obtain the maximum floor deformation denoted as δ_{np}. The ratio of these two displacements at the critical floor demonstrates the amplification due to eccentric pushover, see Eq. 3-4. The plan aspect ratio, n, appears in the numerator to represent displacement measured at the edge of the floor, and the $(1+n^2)$ term appears in the denominator to represent the effect of rotational inertia. Therefore, contrary to what one may speculate, an increase in plan aspect ratio diminishes the amplification factor, i.e., the 1:1 square system has the highest amplification factor among all cases when the Ω value is fixed. α_p differs from α_1 mainly in two aspects: 1) α_p is the response of a static analysis where inertia does not take place, 2) α_p is the response of a deterministic system with a symmetric plan where no stiffness uncertainty exists for VLLRs.

$$\alpha_p = \frac{\delta_p}{\delta_{np}} = 1 + \frac{6ne}{\Omega^2(1+n^2)} \qquad \text{Eq. (3-4)}$$

Given displacement data from time history analysis, the median and 84th percentile value of equivalent eccentricity (denoted as $e^{50\%}$ and $e^{84\%}$) can be obtained by equating median and the 84th percentile value of α_1 (denoted as $\alpha_1^{50\%}$ and $\alpha_1^{84\%}$) with α_p calculated using Eq. 3-5 and Eq. 3-6 (for each building height and aspect ratio n). It is worth noting that Eq. 3-5 and Eq. 3-6 imply that equivalent eccentricity increases with the increase of n and Ω^2. However, given that $\alpha_1^{50\%}$ and $\alpha_1^{84\%}$ are also highly dependent on n and Ω^2, the outcome for $e^{50\%}$ and $e^{84\%}$ is only slightly sensitive to n and Ω^2 (illustrated in the next sections).

$$e^{50\%} = \frac{\left(\alpha_1^{50\%} - 1\right)\Omega^2(1+n^2)}{6n} \qquad \text{Eq. (3-5)}$$

$$e^{84\%} = \frac{\left(\alpha_1^{84\%} - 1\right)\Omega^2(1+n^2)}{6n} \qquad \text{Eq. (3-6)}$$

3.3 BUIDLING MODELS AND GROUND MOTIONS

To study the effect of building height, nonlinear behavior, and various plan aspect ratios, 4-, 8-, 12- and 20-story building models are generated. Each frame is a single bay generic frame with 20' (6.10 meters) bay width and 12' (3.65 meters) story height modeled in *OpenSees* (McKenna et al., 2010) (see Figure 3-1). Through investigation of beam-to-column stiffness ratio (ρ) (Chopra, 2016) and column to beam strength ratio (assuming strength and stiffness are proportional), the ratio of the second moment of inertia of beams to columns at each floor is identified. The variation of the second moment of inertia along the height of the models follows the distribution of the story shear experienced by the model under the ASCE-7 Equivalent Lateral Force (ELF) method. The fundamental periods of the model are set to 1.6, 2.4, 3.0, and 4.0 seconds for the 4-, 8-, 12-, and 20-story structures, respectively. These periods are conforming with archetype models suggested in FEMA P695 (2009) moment frames. The second moment of inertia is then calibrated to match the fundamental period. Springs with bilinear hysteretic (Ibarra *et al*., 2005) characteristics at beam ends are used to model nonlinear behavior in the generic frames (illustrated in Figure 3-1). The capacity of each beam is calibrated to achieve 1% inter-story drift ratio at yielding via double curvature assumption for beams and columns. Figure 3-2 shows the pushover curve of the generic frames subject to ELF lateral loads from ASCE-7.

Three dimensional (3-D) models with plan aspect ratios of 1:1, 1:2, 1:4, and 1:8 are generated using 2-D generic frames discussed earlier. While square systems with an aspect ratio of 1:1 consist of 4 identical 2-D frames, those with aspect ratios of 1:2, 1:4 and 1:8 (i.e. n = 2, 4, 8) need to be carefully tackled. Figure 3-3 shows the plan view the 3-D models used in this study. For a 3-D model with a plan aspect ratio of 1:n, the benchmark model is set as n number of 1:1 square systems placed in a row. To simplify the model and keep Ω unchanged, a 3-D model consisting of four VLLRs is used in this study, with each VLLR being *n* times stiffer (and stronger). The stiffness (and strength) of each VLLR is treated as a random variable, that being said, structural components (beams and columns) in each VLLR is fully correlated and structural components between any two VLLRs are correlated with COV = 0.14. For all plan aspect ratios, cases with translational to rotational period ratios ranging from 1.1 to 2.0 are considered. Among these, only cases with two translational period ratios (one for each orthogonal direction) larger than 0.5 and less than 2 are used. It is critical to note that the 3-D model is representative of the benchmark model of a perimeter frame system, which is commonly seen in realistic building structures. Pushover analyses with 5% eccentricity are also conducted for all selected cases to ensure that none of the buildings have Type 1a or Type 1b horizontal irregularity specified in ASCE-7.

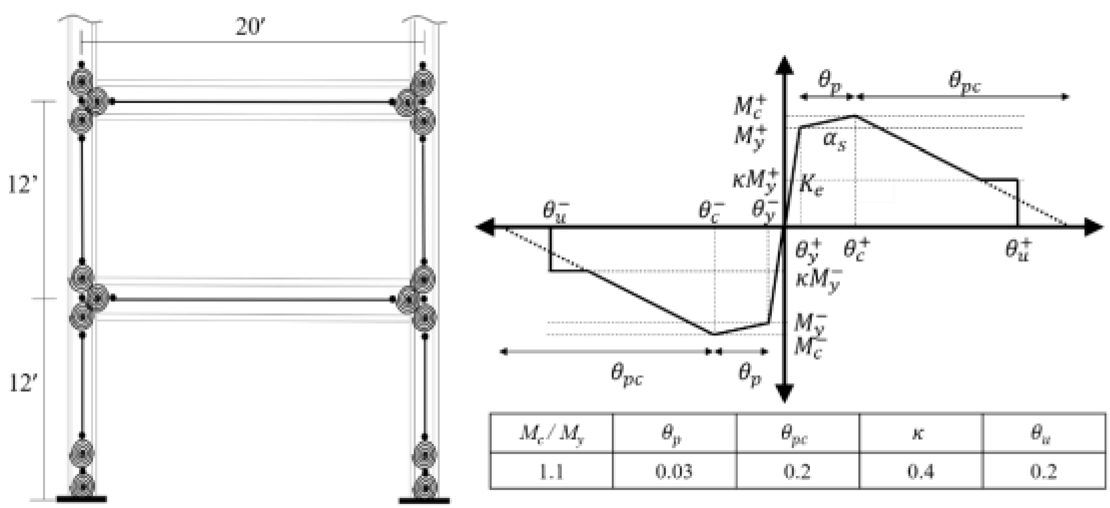

M_c/M_y	θ_p	θ_{pc}	κ	θ_u
1.1	0.03	0.2	0.4	0.2

(a) (b)

Figure 3-1. Generic frame used in this study: (a) geometry, (b) spring backbone curve

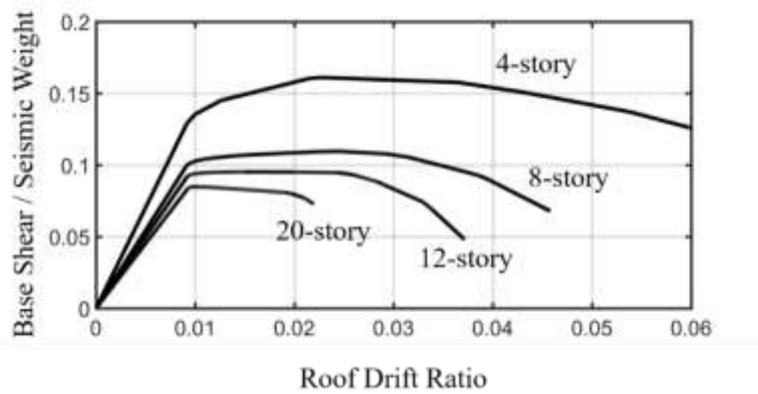

Figure 3-2. Pushover curves of the generic frames used in this study

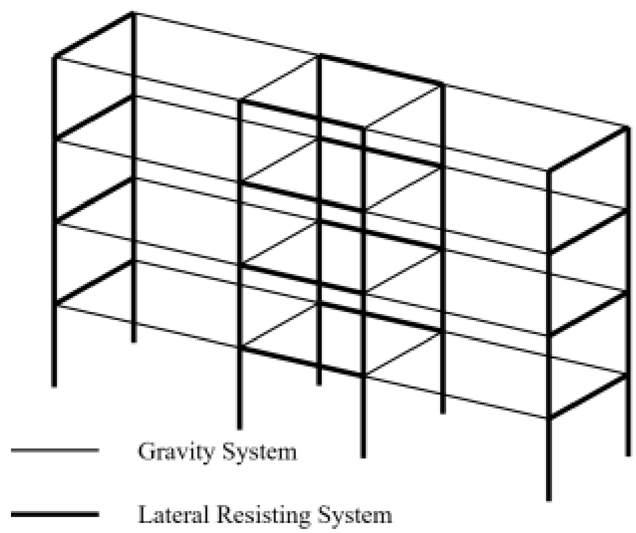

Figure 3-3. A three-dimensional modeling approach to capture plan aspect ratio (1:4 aspect ratio)

Downtown Los Angeles (37.0416°, -118.2468°) and Downtown San Francisco (37.7749°, -122.4194°) are used as testbeds for the generic structures. 50% and 10% probability of exceedance in 50 years (average return period of 72 and 475 years) are used as the ground motion hazard levels for this investigation. Disaggregation of seismic hazard using *OpenSHA* is adopted to obtain magnitude, distance, and epsilon. A conditional spectrum (Baker, 2011) that matches a period range from 0.2 times the smallest translational period to 1.5 times the largest translational period is then used for the selection of 30 pairs of ground motion with a scaling factor larger than 0.5 and less than 2.0. Each selected ground motion is applied to one symmetric-in-plan base case system and two asymmetric systems with randomized VLLRs for each Ω value. Therefore, for each Ω value, nonlinear time history analysis from each ground motion leads to two pairs of asymmetric to symmetric case comparison, and statistical analyses for each Ω value is conducted by $30 \times 2 \times 2 = 120$ data points representing 120 random cases considering both uncertainty in ground motion and uncertainty in asymmetric systems.

3.4 GENERAL OBSERVATIONS AND TRENDS

Results of the downtown San Francisco site for an average return period of 475 years are illustrated in this section. Similar patterns can be found at other hazard levels in downtown San Francisco and for all hazard levels at downtown Los Angeles site (Xiang *et al.*, 2018). The results for the average return period of 475 years would be more attractive, given that this hazard level is close to the design base earthquake in ASCE-7. Statistics of torsional characteristics such as α_1, α_2 and equivalent eccentricity are analyzed in two manners: (1) '*max*' which focuses on the critical floor (the floor with the largest value of α_1 and α_2) among all stories representing the worst-case scenario; (2) '*all floors*': which considers values from all stories. Results of *all floors* for site downtown San Francisco are illustrated in this section, and those of *max* and for downtown Los Angeles are provided in Xiang *et al.* (2018).

In this study, building collapse is defined as maximum inter-story drift ratio exceeding 10%. The space of results (i.e., pairs of one randomized case and its corresponding base case) can be categorized into four distinct scenarios: both randomized case and base case survive (S1); randomized case collapses and base case survives (S2); randomized case survives and base case collapses (S3); both cases collapse (S4). Collapsed base cases provide no significant information in comparing randomized cases and base cases, so results associated with S3 and S4 scenarios are excluded from data for statistical analyses. Data belonging to S2 scenario, by definition, can be interpreted as randomized cases undergoing infinite displacement, therefore, their α_1 and e values are replaced with infinity for statistical analyses. α_2 value is undefined for any data point at S2 scenario (α_2 is computed using displacements of a randomized case); these datapoints are also removed for statistical analyses.

The contribution of the torsional mode of vibration for the maximum displacement observed in all cases is highly dependent on Ω. Figure 3-5 shows the variation of median and the 84th percentile value of α_1 (i.e. $\alpha_1^{50\%}$ and $\alpha_1^{84\%}$) for all buildings with combinations of aspect ratio and Ω. Circle, asterisk, triangle, and square markers represent information associated with 1:1, 1:2, 1:4, and 1:8 floor plan aspect ratios, respectively. A similar trend can be observed in both the median value and variation (the difference between 50% and 84%) of α_1 as they drop with an increase of Ω. When aspect ratio and Ω are both small values, the tall buildings (12-story, 20-story) can achieve a mean amplification as high as 1.14, and an 84th percentile amplification of 1.49, for shorter buildings, the displacement amplification due to torsional effect is small.

The ratio α_2/α_1 as a function of Ω shows the relative dominance of rotational or translational response in the total response of the structure. The ratio of the median value of α_2 to the median value of α_1, from Figures 3-5 and 3-6, is larger than unity at low Ω values. This shows the dominance of torsional response in the total displacement of torsional sensitive buildings. Systems with large Ω, in contrast, have α_2/α_1 less than unity due to dominance of translational response.

In general, the probability of collapse is limited between 0% to 2.5% for an average return period of 475 years. The only exception (8.8% probability of collapse) to this is the 20-story building in downtown San Francisco subject to the average return period of 475 years with a plan aspect ratio of 1:1, Ω value of 1.4 (see Figure 3-5). It is evident that this case possesses the highest probability of collapse; the response (i.e., displacement amplification) of this system is significantly larger than that of other aspect ratios; Ω = 1.4 is the most torsionally sensitive case among all systems with an aspect ratio of 1:1. 20-story buildings are more likely to have higher displacement amplification and spectral acceleration at the 20-story building's natural period is higher in downtown San Francisco compared to that in downtown Los Angeles at 475-year hazard level. As demonstrated in Figure 3-5, this case results in a significantly higher equivalent eccentricity in 84th percentile because 8.8% of the statistics are shifted towards infinity.

Figure 3-6 shows the variation of median and 84th percentiles of α_2 (i.e. $\alpha_2^{50\%}$ and $\alpha_2^{84\%}$) for all buildings with respect to aspect ratio and Ω. The median amplification due to the torsional moment can reach as high as 1.13 (and 1.33 for 84th percentile), and in the same manner, it happens in tall buildings with small values of aspect ratio and Ω.

Equivalent eccentricity is even less dependent on Ω because the mapping from α_1 to α_p offsets their dependency on Ω. Figure 3-7 shows that the median value of equivalent eccentricity to capture the accidental torsional moment is between 2% to 5% for almost all buildings and floor plan aspect ratios. This observation is different for buildings with a floor plan aspect ratio of 1:1 in which the median equivalent eccentricity exceeds 10%. Much of this deviation is due to the nature of how α_p is calculated (see Eq. 3-4). The width of each side of a building with 1:1 floor plan aspect ratio is equal and relatively small; therefore, a larger equivalent eccentricity is needed to compensate and achieve magnifications similar to what is observed for 1:2 and larger floor plan aspect ratios. A similar conclusion can be obtained for the 84th percentile data; equivalent eccentricity is in the order of 6% to 12% for all cases except those with 1:1 floor plan aspect ratio at which the value of equivalent eccentricity is much higher and can reach 33%.

As equivalent eccentricity is computed based on equivalent displacement amplification from a randomized asymmetric case to the base case, other engineering demand parameters (EDPs), such as inter-story drift ratio (IDR), are considered for computing the corresponding equivalent eccentricity. e_{IDR}% is defined as the distance where lateral force should be applied from the center of mass of a base system in order to capture the same level of IDR from an asymmetric system subject to earthquake ground motions. Figure 3-8 shows that the median e_{IDR}% can be above 6% for 1:1 floor plan aspect ratio, and around 1% to 4% for other cases. 84th percentiles of e_{IDR}% for a 20-story building can reach as high as 22% for large values of Ω. Compared to equivalent eccentricity e% that is based on displacement amplification, e_{IDR}%, in general, is smaller because of the inherent difference in governing vibrational mode shapes. However, when focusing on the 'critical floor', much more extreme cases occur and therefore $e_{IDR,max}$% is, in general, a higher estimate than e_{max}%. (Xiang *et al.*, 2018)

Deflection Amplification Factor (C_d) (ASCE 7) is investigated based on two displacement measures: 1) the linear elastic displacement of a symmetric planned building when 5% accidental torsion is applied (base shear computed from the design spectrum assuming R = 8 and I_e = 1); 2) nonlinear displacement response when the building is subjected to GM excitations. Figure 3-9 shows that for buildings designed in downtown San Francisco, the median and 84th percentile values of C_d decrease with the number of stories. For the 4-, 8-, 12- and 20-story buildings, the median C_d is 6.0, 4.0, 3.6 and 2.8, respectively. This decrease is due to the fact that the seismic response coefficient C_s for all cases is governed by the minimum base shear. Results confirm that C_d has a decreasing trend with an increase in building's natural period.

Torsional Irregularity Ratio (TIR) is defined as the ratio of the maximum lateral displacement at the corner of a certain story to the average lateral displacement of the same story. The maximum and average lateral displacements used to calculate *TIR* are determined from a pushover analysis with 5% accidental torsion. A building with *TIR* > 1.2 is classified as having a torsional irregularity per ASCE 7-10. A proportional trend between *TIR* and α_2, shown in Figure 3-10, is expected as α_2 also represents the ratio of maximum lateral displacement (total response) to average lateral displacement (translational response), but with randomized frame stiffness and strength when subject to ground motion excitations. Both *TIR* and α_2 represent system sensitivity to torsion, the former indicating static torsional behavior and the latter indicating dynamic torsional behavior. Utilizing this mapping between *TIR* and α_2, one is able to estimate the 'dynamic torsional irregularity ratio' given the 'static torsional irregularity ratio' as well as building properties such as the building height, aspect ratio and Ω.

Equivalent eccentricity *e* is influenced by the variation of five factors including location (downtown Los Angeles and downtown San Francisco), hazard level (72 years and 475 years average return period), number of stories (4-, 8-, 12- and 20-story), plan aspect ratio (1:1, 1:2, 1:4 and 1:8) and translational to rotational period ratio (ranging from 1.1 to 2.0). As the influence of plan aspect ratio and Ω is explained in Eq.3-5 and Eq.3-6, the influence of building height and ground motion intensity (including location and hazard level) are studied by carrying out an Analysis of Variance. (ANOVA)- see Tables 3-1 and 3-2. *p*-values demonstrate that there are three distinct levels of eccentricity with respect to different numbers of stories: 1) 4-story, 2) 8-story, and 3) 12- and 20-story, which statistically have no difference. This leads to a conclusion that equivalent eccentricity increases with building height: as building height increases, the effect of accidental torsion and the effect of rotational response are prone to 'accumulate' along with the building stories. However, there is not enough evidence to show that a 20-story building has essentially higher levels of equivalent eccentricity than a 12-story building.

Table 3-1. F test results for the dependence of equivalent eccentricity and number of stories

Source	*F-Value*	*p-Value*
4 story vs. 8 story	69.29	9e-17
4 story vs. 12 story	206.43	1e-46
4 story vs. 20 story	205.49	2e-46
8 story vs. 12 story	41.8	1e-10
8 story vs. 20 story	33.54	7e-9
12 story vs. 20 story	1.14	0.286

Table 3-2. F test results for the dependence of equivalent eccentricity and number of stories

Source	*F-Value*	*p-Value*
LA 72 vs. LA 475	3.5	0.063
LA 72 vs. SF 72	2.12	0.148
SF 72 vs. SF 475	9.44	0.003
LA 475 vs. SF 475	0.1	0.964

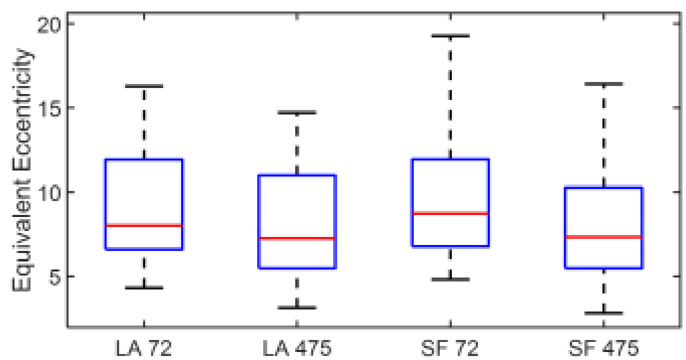

Figure 3-4. Distribution of Equivalent Eccentricity for four cases: site downtown Los Angeles and downtown San Francisco with 72-year and 475-year average return period return period

Table 3-2 and Figure 3-4 show that the equivalent eccentricity derived from ground motions selected based on two different locations (LA and SF) is not statistically different regardless of the return period. While the return period is statistically significant regardless of the selection of the location, given the small *p*-values for both cases (LA 72 vs. LA 475 and SF 72 vs.

SF 475). For this reason, only the results of downtown San Francisco are shown in this section and the results of downtown Los Angeles are provided in Xiang *et al.* (2018).

The suggested values for equivalent eccentricity are obtained using all floors in the buildings. $\alpha_1^{50\%}$ and $\alpha_1^{84\%}$ obtained from performing statistical analysis on α_1 values of the most critical floor will be much larger than the values if all floors were considered. Data available in Xiang *et al.* (2018) (not illustrated for space consideration) show a complete set of results of α_2, α_1, e, e_{IDR}, and C_d. The median values of α_1 and α_2 can reach up to 1.29 and 1.28, respectively; their 84th percentile values can reach up to 1.69 and 1.61, respectively. The median values of e and e_{IDR} can reach up to 17% and 29%, respectively and the 84th percentile values can reach up to 45% and 62% for e and e_{IDR}, respectively. Considering EDPs at all floors, 5% accidental torsion is adequate for most of the cases to capture the torsional effect due to the randomness in stiffness. If a more conservative confidence level, such as 84th percentile, is required then 20% accidental torsion will be suitable for most 1:1 plan aspect ratio case; for 1:2, 1:4 and 1:8 plan aspect ratio cases, an eccentricity value slightly larger than 10% will be adequate for design purposes. While considering the worst-case scenario (critical floor), for median level, 10% to 20% accidental torsion is needed for the 1:1 system, and 5%-10% will be adequate for all other aspect ratios. A more conservative confidence level (84th percentile) will require a value between 10%-20% for aspect ratios other than 1:1 and as high as 20%-40% for a building with 1:1 plan aspect ratio.

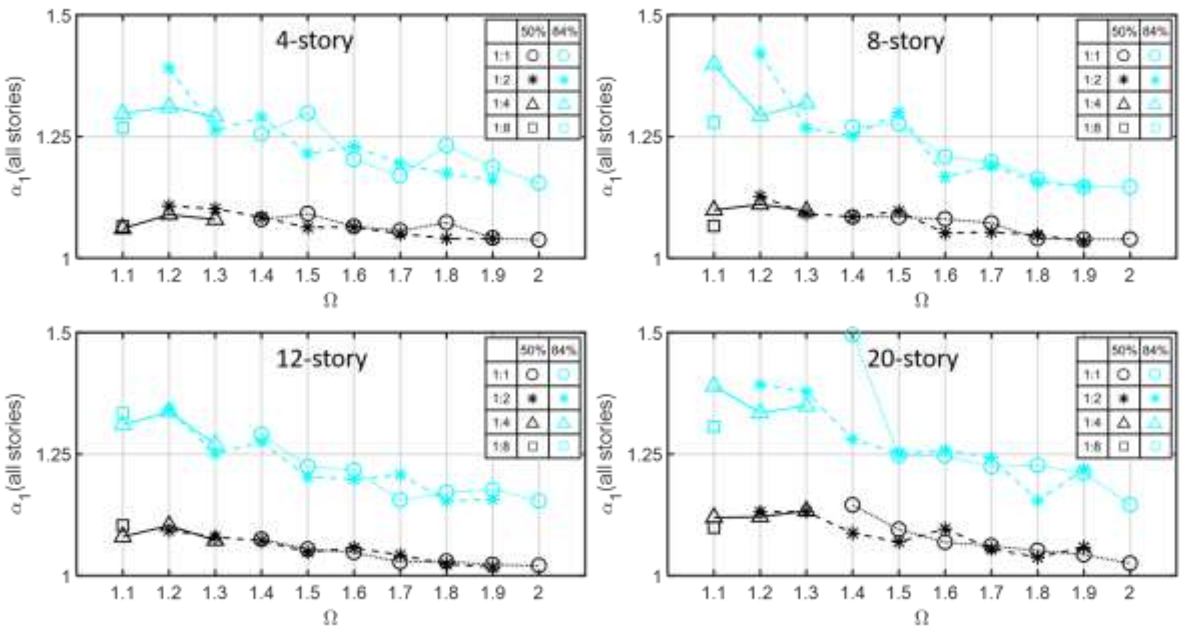

Figure 3-5. Variation of $\alpha_{1,all}^{50\%}$ and $\alpha_{1,all}^{84\%}$ with respect to Ω and plan aspect ratio for all buildings

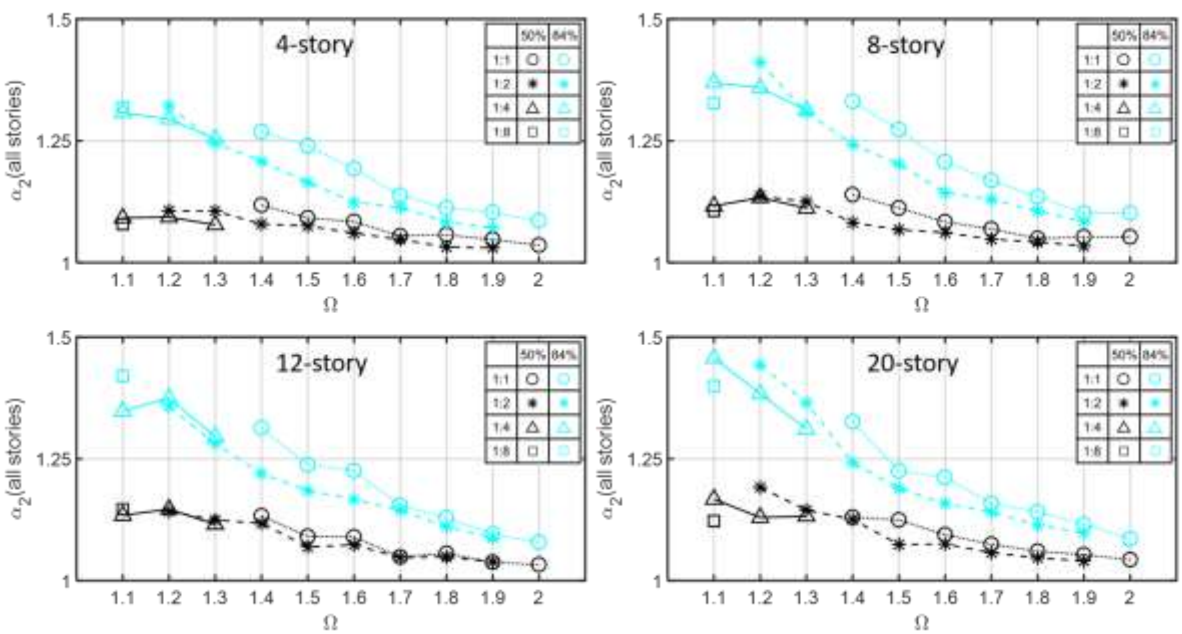

Figure 3-6. Variation of $\alpha_{2,all}^{50\%}$ and $\alpha_{2,all}^{84\%}$ with respect to Ω and plan aspect ratio for all buildings

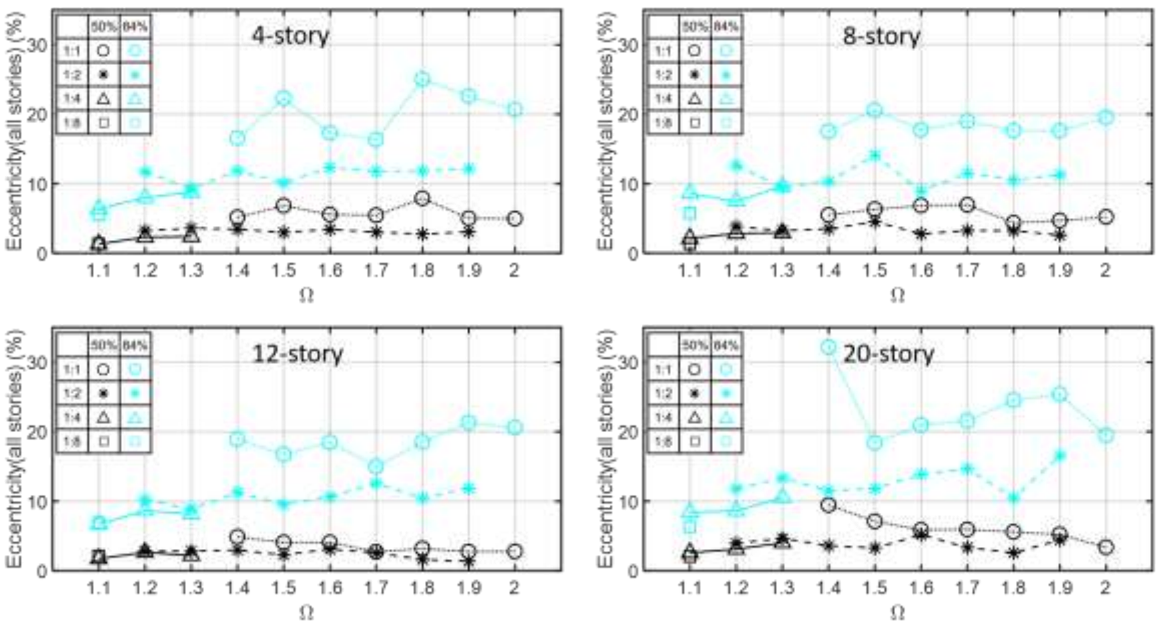

Figure 3-7. Variation of $e_{all}^{50\%}$ and $e_{all}^{84\%}$ with respect to Ω and plan aspect ratio for all buildings

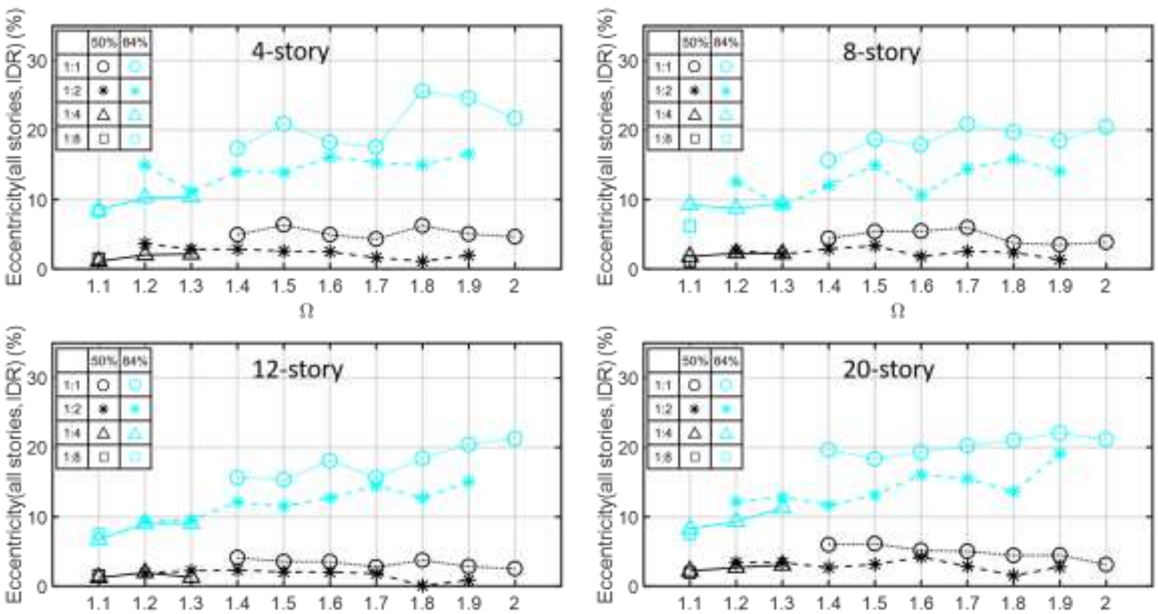

Figure 3-8. Variation of $e_{IDR,all}^{50\%}$ and $e_{IDR,all}^{84\%}$ with respect to Ω and plan aspect ratio for all buildings

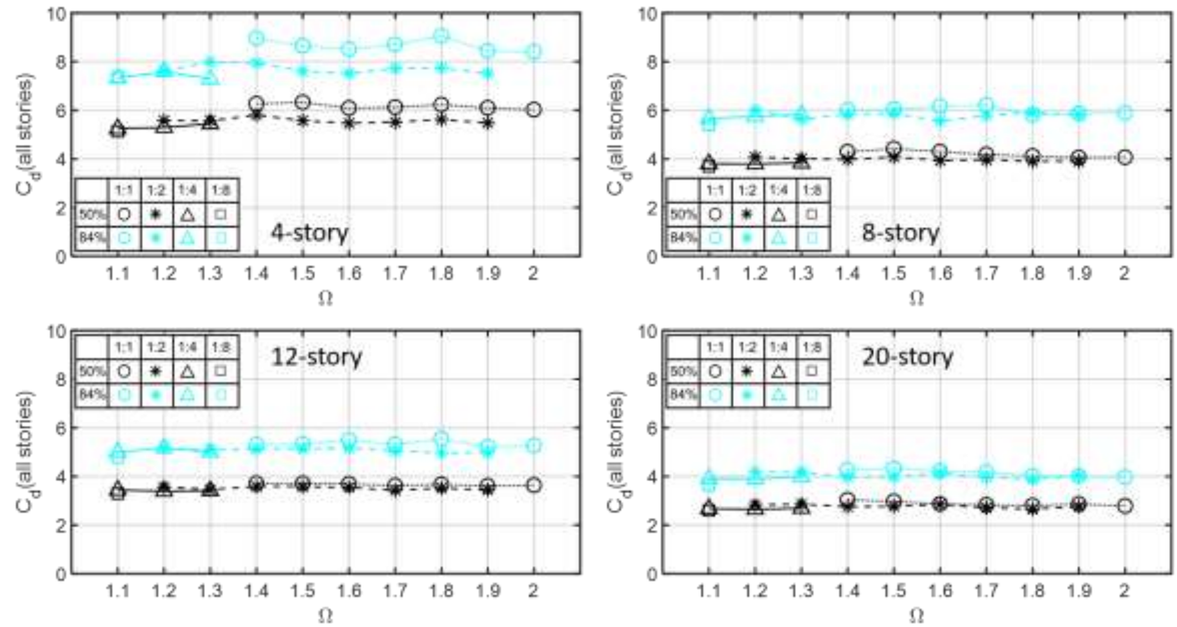

Figure 3-9. Variation of $C_{d,all}^{50\%}$ and $C_{d,all}^{84\%}$ with respect to Ω and plan aspect ratio for all buildings

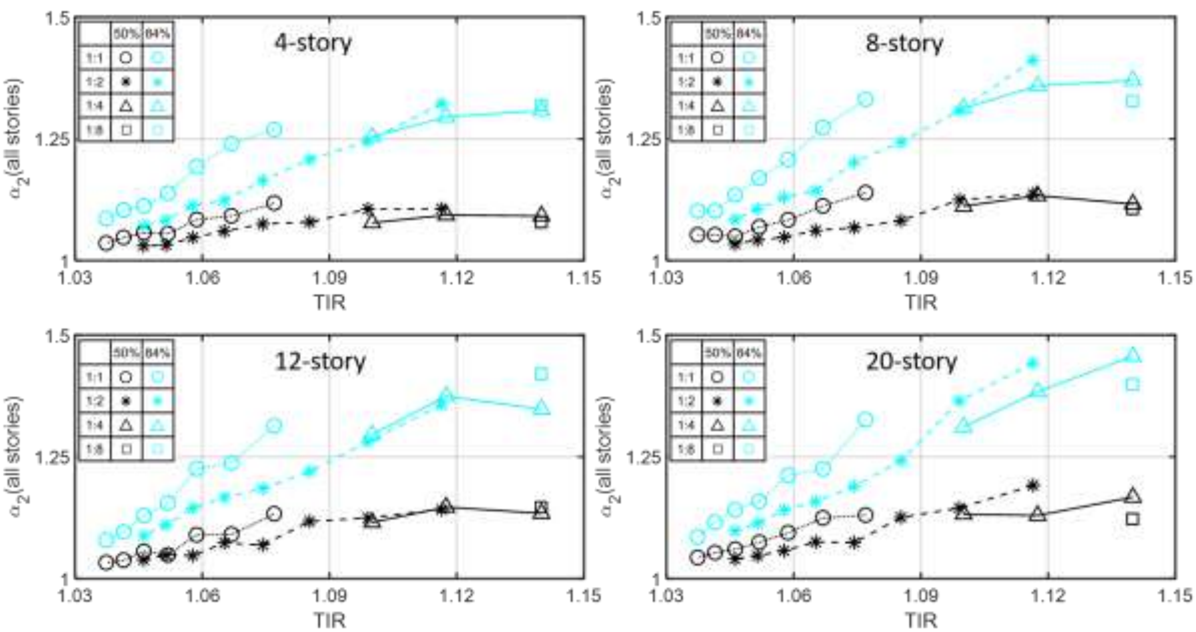

Figure 3-10. Variation of $\alpha_{2,all}^{50\%}$ and $\alpha_{2,all}^{84\%}$ with respect to TIR and plan aspect ratio for all buildings

3.5 COMPARISON WITH CSMIP DATABASE

To validate analytical results, the variation of α_2 with respect to Ω and plan aspect ratio of

11 buildings along with 12 sets of recorded translational and rotational responses from CSMIP database (Table 3-3). The selected buildings are nominally symmetric in plan and have more than one sensor on each floor in at least one translational direction (#57357 has two sensors in both directions). 4- and 5-story CSMIP buildings are categorized into the 4-story building group, 7-, 8- and 9-story CSMIP buildings are categorized into the 8-story building group and 13-story CSMIP buildings are categorized into the 12-story building group. Ω is computed using the signals in the frequency domain. Given that different sets of signals lead to a different estimate of the dominant frequency, the Ω estimate varies for the same building subject to multiple ground motion excitations. An illustration of the calculation of Ω is demonstrated in Figure 3-11 using Frequency domain system identification methods. (Juang, 1997). As shown in Figure 3-12, 3-13 and 3-14, α_2 is computed from every instrumented floor for each seismic event, then compared to the analytical results of $\alpha_{2,all}^{50\%}$ and $\alpha_{2,all}^{84\%}$ under the hazard level of 50% probability of exceedance in 50 years (72-year average return period). This comparison is valid because the recorded seismic events have spectral acceleration at the building's fundamental period ranging from 0.0004g to 0.5g, with a median of 0.03g. Table 3-3 summarizes the location of the selected buildings. Given that location is not statistically significant in predicting the building torsional characteristics, CSMIP data is plot with the analytical results obtained from site downtown San Francisco regardless of the actual location of the building in CSMIP database. The plan aspect ratio of CSMIP buildings is divided into two categories: larger than 1:1 and less than 1:2 (denoted by red pentagons), and larger than 1:2 and less than 1:4 (denoted by blue hexagons).

Table 3-3. Selected buildings from CSMIP database

Building ID	*Number of stories*	*Plan Aspect Ratio*	*Category*	*Location*
12299	4	1.8		Palm Springs

58261	4	1.9	4-story	South San Francisco
24463	5	1.4		Los Angeles
12493	4	1.7		Indio
24571	9	2.5		Pasadena
24386	7	2.8	8-story	Van Nuys
23481	7	1.5		Redlands
24249	8	2.3		Los Angeles
57357, x-dir	13	1.0		San Jose
57357, y-dir	13	1.0	12-story	San Jose
58354	13	1.0		Hayward
24322	13	2.6		Sherman Oaks

Analytical building models have Ω values ranging from 1.1 to 2; Ω of CSMIP buildings do not necessarily cover the same range and can reach less than 1.1 under certain circumstances. However, a declining trend in α_2 with increasing Ω can be observed both in analytical models and CSMIP buildings. Plan aspect ratio, on the other hand, is not as a significant factor as Ω for both analytical and CSMIP statistics. The median values of the analytical results are able to capture the median of α_2 obtained from CSMIP buildings and the dispersion of CSMIP data matches well with that of analytical data: the more torsionally sensitive the system is, the higher the variance of α_2 will be.

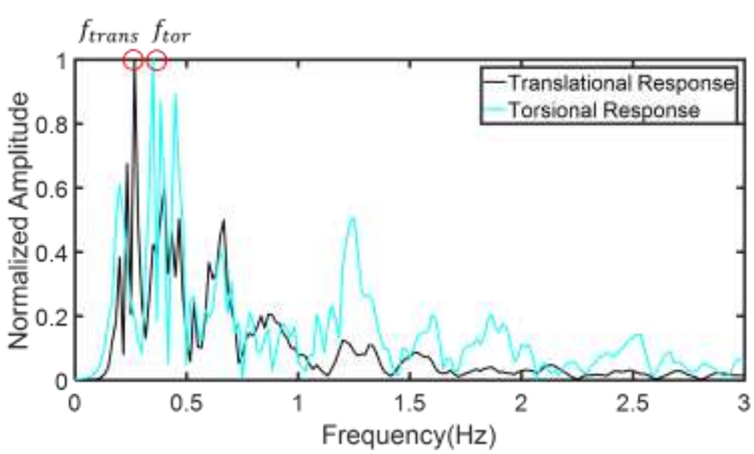

Figure 3-11. Illustration of calculation of Ω for 8-story building ID 24322 subject to Earthquake Landers 92

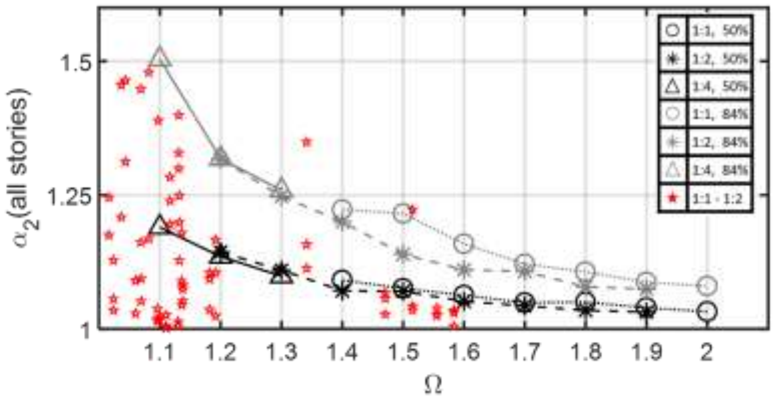

Figure 3-12. Analytical and CSMIP data of $\alpha_{2,all}^{50\%}$ and $\alpha_{2,all}^{84\%}$ with respect to Ω and plan aspect ratio for 4-story buildings subject to ground motions of 475-year average return period in downtown San Francisco

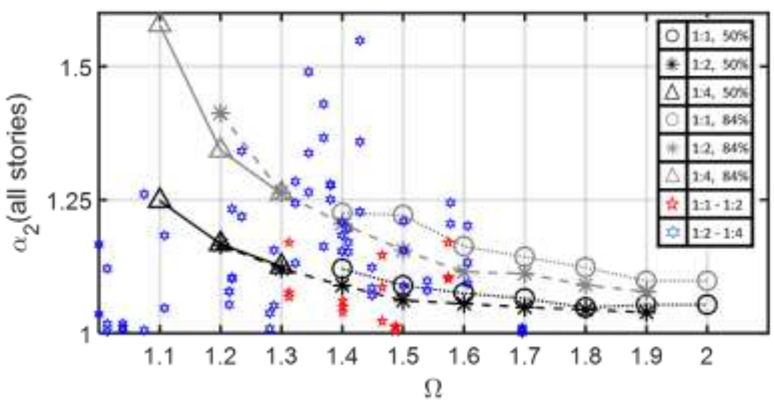

Figure 3-13. Analytical and CSMIP data of $\alpha_{2,all}^{50\%}$ and $\alpha_{2,all}^{84\%}$ with respect to Ω and plan aspect ratio for 8-story buildings subject to ground motions of 475-year average return period in downtown San Francisco

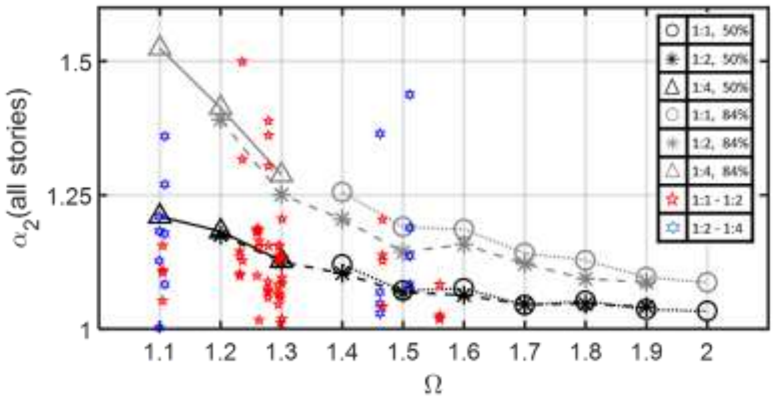

Figure 3-14. Analytical and CSMIP data of $\alpha_{2,all}^{50\%}$ and $\alpha_{2,all}^{84\%}$ with respect to Ω and plan aspect ratio for 12-story buildings subject to ground motions of 475-year average return period in downtown San Francisco

3.6 CONCLUSIONS

The research summarized herein aims to quantify equivalent eccentricity–for ASCE-7 lateral load application–that captures the effects of the accidental torsional moment in building structures. It is assumed that randomness in the stiffness of VLLRs is the primary source of accidental torsion. For this purpose, a combination of four building heights with 4, 8, 12, and 20 stories, and four-floor plan aspect ratios (i.e., 1:1, 1:3, 1:4, and 1:8) are considered. For each combination, 3-D models are generated with ratios of torsional and translational modes of vibration that fall in intervals realistic in actual structural designs. Each side of the 3-D model consists of a single-bay generic frame whose stiffness and strength characteristics are tuned to deform in a straight-line shape under ASCE-7 lateral load application and the reach yield moment at beam ends at 1% inter-story drift ratio.

Following a comprehensive literature survey, it is assumed that the coefficient of variation (COV) of the stiffness of all structural elements is equal to 0.14. Using this information, and by utilizing 30 pairs of ground motions that represent seismic hazard with an average return period of 475 years for a site in downtown San Francisco, Monte Carlo simulation was employed to obtain statistical measures of maximum floor displacement due to randomness in the stiffness of VLLRs. Similar simulations were conducted for a site located in downtown Los Angeles.

From the Monte Carlo scheme explained earlier, a median value for the floor amplification factor can be obtained. This median amplification value obtained from Monte Carlo is used to determine the median eccentricity value through a static pushover analysis using ASCE-7 equivalent lateral forces.

84^{th} percentile values for equivalent eccentricity are obtained in the same manner by using the 84^{th} percentile values for the magnification factor obtained from the Monte Carlo scheme.

From the Monte Carlo scheme explained earlier, a median value for the floor amplification factor can be obtained. This median amplification value obtained from Monte Carlo is used to determine the median eccentricity value through a static pushover analysis using ASCE-7 equivalent lateral forces.

The results show that the 5% equivalent eccentricity rule is adequate to capture the median value of magnification in deformation due to accidental torsion. In all cases, except for buildings with a 1:1 plan aspect ratio, this value is conservative. This conclusion is based on performing statistical analysis on all floor displacement magnification due to accidental torsion. The reported value for equivalent eccentricity would be larger if the most critical floor displacement amplification due to accidental torsion is considered in the statistical analysis or a higher than median confidence is sought to develop the values of equivalent eccentricity.

Finally, ductility (C_d) in randomized asymmetric systems is scrutinized so that an approach of estimating peak total displacement response given designed elastic displacement is provided. Torsional Irregularity Ratio (*TIR*), as a measure of torsional sensitivity in the design phase, is reviewed and related to another torsional sensitivity representation used in dynamic time history analysis.

3.7 ACKNOWLEDGEMENT

The research reported herein was carried out in part with support from the California Strong Motion Instrumentation Program (CSMIP) through standard agreement 1016-986. This support is gratefully acknowledged. The contents of this manuscript do not necessarily represent the policy of that agency nor endorsement by the State Government.

3.8 REFERENCES

ASCE-American Society of Civil Engineers (2017). Minimum Design Loads for Buildings and Other Structures (ASCE/SEI 7–16). American Society of Civil Engineers: Reston, VA.

ASCE-American Society of Civil Engineers (2010). Minimum Design Loads for Buildings and Other Structures (ASCE/SEI 7–10). American Society of Civil Engineers: Reston, VA.

ASTM A6 (2005). Standard Specification for General Requirements for Rolled Structural Steel Bars, Plates, Shapes, and Sheet Piling. American Standards for Testing and Materials, ASTM International, West Conshohocken, Pennsylvania.

ASTM A992 (2004). Standard Specification for Structural Steel Shapes. American Standards for Testing and Materials, ASTM International, West Conshohocken, Pennsylvania.

Baker, JW. (2011). Conditional Mean Spectrum: Tool for Ground-Motion Selection. ASCE Journal of Structural Engineering, 137 (3), 322-331.

Basu, D., Constantinou, M., Whittaker, A. (2014). An Equivalent Accidental Eccentricity to Account for The Effects of Torsional Ground Motion on Structures. Engineering Structures, 69: 1-11.

Bournonville, M., Dahnke, J. and Darwin, D. (2004). Statistical Analysis of the Mechanical Properties and Weight of Reinforcing Bars. Structural Engineering and Engineering Materials. Report 04-1.

British Standards Institution. (1996). Eurocode 8: design provisions for earthquake resistance of structures. London, British Standards Institution.

DeBock, D.J., Liel, A.B., Haselton, C.B., Hooper, J.D., Henige Jr. R.A. (2014). Importance of seismic design accidental torsion requirements for building collapse capacity. Earthquake Engineering and Structural Dynamics, 43:831-850.

Chopra, A. K., (2016). Dynamics of Structures: Theory and Applications to Earthquake Engineering. Fourth Edition.

De-la-Colina, J., Almeida, C. (2004). Probabilistic Study on Accidental Torsion of Low-Rise Buildings. Earthquake Spectra, 20(1):25-41.

De la Llera, JC., Chopra, A. (1992). Evaluation of Code-Accidental Torsion Provisions using Earthquake Records from Three Nominally Symmetric-Plan Buildings. SMIP92 Seminar Proceedings.

De la Llera, JC., Chopra, A. (1994). Accidental Torsion in Buildings Due to Stiffness Uncertainty. Earthquake Engineering and Structural Dynamics, 23:117-136.

De la Llera, JC., Chopra, A. (1995). Estimation of Accidental Torsion Effects for Seismic Design of Buildings. Journal of Structural Engineering, 121(1):102-114.

Ellingwood, B., Galambos, T., MacGregor, J. and Cornell, C. (1980). Development of a probability based load criterion for American National Standard. Special Publication No.577, National Bureau of Standards, Washington, DC.

FEMA, 2009, Quantification of Building Seismic Performance Factors, FEMA P-695, prepared by Applied Technology Council for the Federal Emergency Management Agency, Washington, D.C.

Hernandez, JJ., Lopez, O. (2004). Dependence of Accidental Torsion on Structural System Properties. Proceedings of the 13th World Conference on Earthquake Engineering, Vancouver, Canada.

Juang, J. (1997). Identification of Linear Structural Systems using Earthquake Induced Vibration Data. Journal of Guidance, Control, and Dynamics, 20(3):492-500.

Ibarra L.F., Medina R. A., and Krawinkler H. (2005). "Hysteretic models that incorporate strength and stiffness deterioration", Earthquake Engineering and Structural Dynamics, 34(12), 1489-1511.

Lin, WH., Chopra, A., De la Llera, JC. (2001). Accidental Torsion in Buildings: Analysis versus Earthquake Motions. Journal of Structural Engineering, 127(5):475-481.

McKenna, F., Scott, M.H., and Fenves, G.L. (2010). Nonlinear Finite Element Analysis Software Architecture Using Object Composition. Journal of Computing in Civil Engineering, 24(1):95-107.

Melchers, R. (1987). Structural Reliability: Analysis and Prediction, Ellis Horwood, Chichester, 1987.

Ramsay, R., Mirza, S., and MacGregor. (1979). Monte Carlo Study of Short Time Deflections of Reinforced Concrete Beams. ACI, Vol.76 (897-918)

Xiang, Y., Naeim, F., Zareian, F. (2018) Critical Assessment of Code Torsional Provisions using CSMIP Database of Instrumented Buildings, CSMIP Report.

CHAPTER 4: A DAMPING ELEMENT MODEL FOR ENERGY DISSOPATION CHARACTERIZATION IN BUILDING STRUCTURES

4.1 INTRODUCTION

One of the most unclear issues in the seismic design of new buildings, and retrofit of existing structures, is how damping is characterized and modeled. All design codes provide suggestions for the model damping ratio and how to use them in the design process. Federal Emergency Management Agency, FEMA P-58-1 (2012), requires a 1% to 5% equivalent model damping ratio for predominant modes of building structures. Meanwhile, the minimum design loads for buildings and other structures, ASCE/SEI 7 (2017), suggests the use of a 5% model damping ratio for the fundamental mode. Tall Building Initiative Guidelines, PEER (2017), and Los Angeles Tall Buildings Structural Design Council, LATBSDC (2018) both suggest that model damping ratio of the predominant modes should not exceed 2.5%.

The estimation of the model damping ratio has been widely studied. Researchers have suggested that the damping ratio is not a constant value but depends on variables such as building material type and building height. Cruz and Miranda (2016), Satake et al. (2003), and Fritz et al. (2009) provide equations of damping ratio as a function of building height for a different type of building structures such as steel moment frames and reinforced concrete moment frames. They used data from instrumented buildings in the US and Japan and estimated damping ratios through system identification methods. It is found that the first mode damping ratio is smaller in tall buildings compared to low-rises. Researchers also related damping ratio values with their corresponding frequency and period. Stake (2003) analyzed building periods and damping ratios from full-scale data of buildings in Japan and concluded that damping is amplitude-dependent, and the first mode damping ratio in the small amplitude region increases linearly with the building's natural frequency. Similar patterns are observed by Bernal et al. (2012) that damping ratio is a function of the natural period, and it increases at higher mode shapes.

Other researchers found that the damping ratio also varies with amplitudes because much of the energy dissipation in building structures is from the friction between various structural as well as non-structural elements. Several studies have shown that the damping ratio is amplitude-dependent. Wyatt (1977) assumed that the source of energy dissipation in a structural system is friction-based and introduced a 'Stick-Friction' model implemented via stick-slip elements. Jeary (1997) found that damping remains constant at low amplitude vibrations, and it increases with vibration amplitude in the nonlinear region. Damping increases since more imperfections are activated until it arrives at the high amplitude plateau where all material imperfections are activated so that damping becomes eventually constant. In contrast, some studies have demonstrated that after all contact surfaces have slipped, total friction force remains constant, and the increase of amplitude causes a decrease of damping. Tamura (2008) used a random decrement technique to obtain the damping ratio estimation from signals and developed a model demonstrating the behavior of the critical tip ratio from where damping begins to decrease. These studies showed that the damping ratio remains constant at low excitation amplitudes. It increases after the amplitude passed a certain threshold, and the damping ratio reaches a plateau or even starts dropping at a higher excitation amplitude. Instead of using deterministic values for the vibration amplitude and the slip force, Spence and Kareem (2014) proposed a joint probability density function for these two parameters through a 'Stick-Slip' nonstructural element model.

Given that one of the goals of this study is to calibrate the properties of the damping element to match the recorded data with analytical results from finite element models, engineering optimization approaches are utilized to estimate and evaluate the key components of the generic building frame, including the stiffness of the columns and beams, the viscous damping coefficient, the stiffness of the frictional damper and the yielding point of the frictional damper. Optimization methods are widely used in system identification and model updating of building structures. Ebrahimian et al. (2017) updated a nonlinear finite element model of a frame-type structure by minimizing the discrepancies between predicted and measured response; their work, among others, is conducted using simulated data instead of recorded data. Nasrellah and Manohar (2011) proposed an identification method that uses particle filtering to capture the behavior of structures, including both computational models and models from laboratory and field tests. Song and Dyke (2014) proposed a real-time dynamic model updating method to match a modified Bouc-Wen model using data from two shake table tests. Lagaros et al. (2002) investigated evolutionary algorithms, including Genetic Algorithms and Evolution Strategies and optimized the weight of two space structures with inter-story drift being the constraints. Perez and Behdinan (2007) verified the effectiveness of the Particle Swarm Optimization method on structural optimization tasks by estimating the cross-sectional area, allowable displacement, and stresses for members in a truss system.

This study investigated seven steel moment-resisting frame buildings located in California. Acceleration response is obtained from the instrumented buildings subject to multiple ground motion excitations at different intensities. Particle Swarm Optimization (PSO) (Perez and Behdinan, 2007) is adopted in this study to capture the parameters in the generic frame with a damping element containing viscous and frictional damper built in OpenSees (McKenna et al., 2010) that match the acceleration response of the building at the sensor location with the recorded data. Energy dissipation from the viscous damper and the frictional damper, as well as the parameter of the damper such as the viscous damping coefficient, the stiffness of the frictional damper and the yielding point of the frictional damper, are analyzed and studied according to several variables such as building height, frame depth, and ground motion intensity measure.

4.2 MODEL DESCRIPTION

It is hypothesized that energy dissipation in structures is viscous and friction-based and propose a damping element model that captures both sources of damping. The suggested model consists of a friction damper and a viscous damper working in parallel, as demonstrated in Figure 4-1. To implement a damping element model, this study adopts a continuum model (Miranda and Taghavi, 2005) where axially rigid members connect a flexural cantilever beam and a shear cantilever beam. As is shown in Figure 4-1(a), deformation in bending and shear configurations can be captured by flexural rigidity EI and shear rigidity GA, respectively. Parameters that are used to describe this model include *i*) flexural rigidity, *ii*) shear rigidity at the base, and *iii*) two constant values controlling the distribution of flexural rigidity and shear rigidity along the height. Bilinear hysteretic material properties are used for zero-length elements at each floor. The suggested model was calibrated based on the CSMIP database of strong motion data. Masses at each floor are treated as knowns based on the floor plan information provided by the CSMIP database. Compared to detailed models, the continuum model used here is preferable because it is governed by a relatively small number of parameters and can be generalized to represent a large group of buildings, e.g., a model with large flexural rigidity and small shear rigidity can be representative of a tall reinforced concrete shear wall, and a model with small flexural rigidity and large shear rigidity can be representative of a short moment resisting frame.

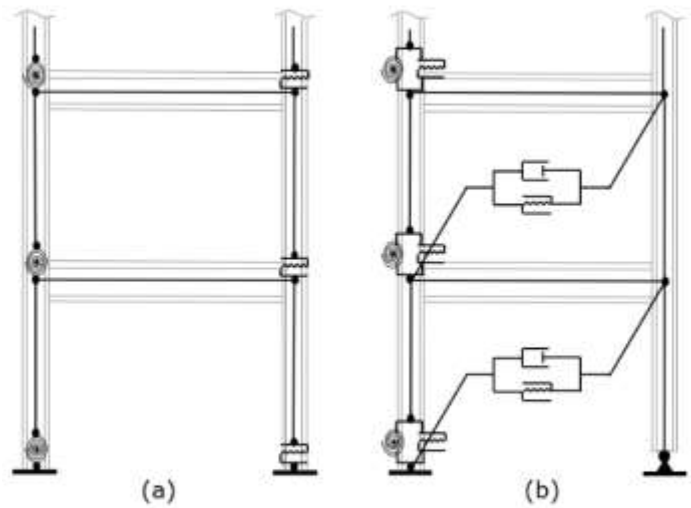

Figure 4-1. (a) A continuum model where a flexural cantilever beam and a shear cantilever beam are connected; (b) A further simplified ‘two-beam’ model with damping elements implemented

The continuum model is further simplified as a ‘two-beam model’ demonstrated in Figure 4-1(b) to introduce the energy dissipation of the model through damping elements. The model consists of three sets of elements: *i*) vertical element on the left-hand side denoted as ‘L-beam,’ *ii*) vertical element on the right-hand side denoted as ‘R-beam,’ and *iii*) damping elements. The R-beam is made of a material with large flexibility and pinned at the base and is connected to the L beam to representing a rigid diaphragm. The L-beam is an amalgam of rigid elements in the middle connecting zero-length elements representing the shear and flexure behavior at each story level by ‘shear material’ in the transverse direction and ‘flexure material’ in the rotational direction, respectively. Damping elements are then incorporated in this model between every two adjacent floors, and damping forces are modeled as functions of relative displacement and relative velocity.

Three different sources of history-dependent damping force are considered: one accounts for energy dissipation through breakage of nonstructural elements, one accounts for friction and slippage behavior of joints and nonstructural element contact surfaces, the other accounts for velocity-dependent material viscous damping. For the nonstructural element breakage, the governing parameters are initial stiffness K_{e1} and yield strength F_{y1}. It is assumed that no hardening, unloading, or stiffness/strength deterioration will be observed in the breakage of nonstructural elements. For the frictional damping element, the governing parameters are initial stiffness K_{e2} ($\approx\infty$ since very small amplitude can trigger frictional behavior), yield strength F_{y2} and cyclic strength deterioration parameter λ_s. For simplicity, the first two damping mechanisms are combined, and the force-deformation relationship of the combined material is modeled by initial stiffness K_e, yield deformation δ_y and cyclic strength deterioration parameter λ_s. Usually, the hysteretic material properties are controlled by four factors: pinching factor for strain, pinching factor for stress, damage due to ductility, and damage due to energy. This model ignores the first three factors and only considers the strength reduction caused due to energy dissipated by the inelastic strain (the strength reduction increases with the number of cycles at fixed strain). The combined material and the viscous damping material are then included in the model in parallel at every two adjacent floors and are assumed to be the same for all story levels.

To build the generic frames in OpenSees, the theoretical model in Figure 4-1 is transferred to two possible “physically meaningful” models illustrated in Figure 4-2, namely, the α_0 model and the ρ model. The relationship between the flexural rigidity EI, the shear rigidity GA and the nondimensional parameter α_0 is given in Eq. 4-1, and the relationship between α_0 and ρ (beam-to-column stiffness ratio) is given in Eq. 4-2, where N represents the total number of stories. α_0 is a nondimensional parameter that controls the flexural and shear behavior of the building; therefore, it can be related to the eigenvalue parameters γ_i and modal periods T_i, as shown in Eq. 4-3 and 4-4, where γ_i are the roots of Eq. 4-4. It should be noted that the α_0 model consists of distributed mass along the building height; therefore, it is computationally expensive to run nonlinear time history analysis. The equivalent ρ model, however, only requires the beam to column stiffness ratio can be built with beam-column elements and lumped mass at each story conveniently. Therefore, the ρ model is finally adopted in this study and built in OpenSees with parameters including the stiffness of the beam I_b, the stiffness of the columns I_c, the area of the columns A, the damping coefficient of the viscous damper c, the initial stiffness of the frictional damper K_e, the yield deformation of the frictional damper δ_y.

$$\alpha_0 = H\sqrt{GA_0 / EI_0} \qquad \text{Eq.(4-1)}$$

$$\rho = \alpha_0^2 / 12N^2 \qquad \text{Eq.(4-2)}$$

$$T_i / T_1 = (\gamma_1 / \gamma_i)\sqrt{(\gamma_1^2 + \alpha_0^2) / (\gamma_i^2 + \alpha_0^2)} \qquad \text{Eq.(4-3)}$$

$$2 + [2 + \frac{\alpha_0^4}{\gamma_i^2(\gamma_i^2 + \alpha_0^2)}]\cos(\gamma_i)\cosh(\sqrt{\alpha_0^2 + \gamma_i^2}) + \frac{\alpha_0^2}{\gamma_i(\gamma_i^2 + \alpha_0^2)}\sin(\gamma_i)\sinh(\sqrt{\alpha_0^2 + \gamma_i^2}) = 0 \qquad \text{Eq.(4-4)}$$

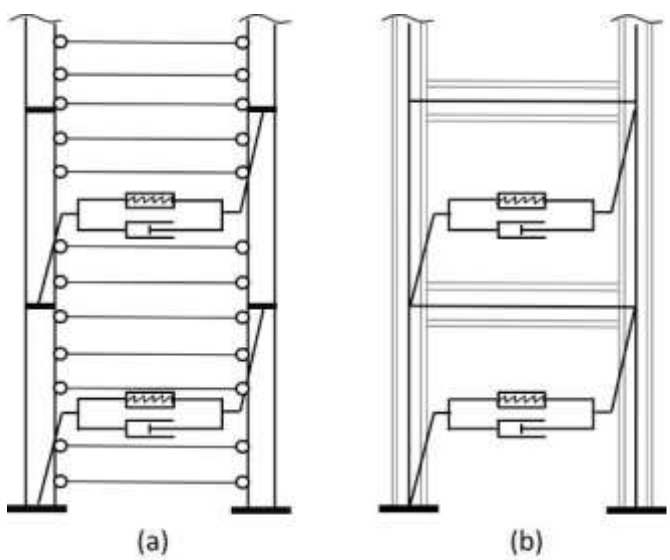

Figure 4-2. (a). The α_0 model with damping elements; (b). The ρ model with damping elements

The following steps are taken in order to estimate the optimal setting of parameters of the model:

1) Recorded acceleration signals are extracted and analyzed. The first three modal periods are estimated via the system identification method.

2) Given that the period ratio T_i / T_1 is computed in Step 1, a multi-subjective optimization technique is carried out to find the optimal α_0 value using Eq. 4-3 and Eq.4- 4.

3) The beam-to-column stiffness ratio ρ is calculated from Eq. 4-2.

4) A generic frame without damping elements is built in OpenSees. It should be noted that the only parameter controlling the model is the stiffness of the column I_c since the stiffness of the beam I_b is known and calculated from ρ. The optimal I_c is found through a one-dimensional optimization technique. (number of parameters equals 1).

5) A sophisticated ρ model with damping elements is built in OpenSees with I_c and I_b estimated from step 4. The optimal setting of parameters, including the damping coefficient of the viscous damper *c*, the initial stiffness of the frictional damper K_e, the yield deformation of the frictional damper $\delta_{y,}$ is found through the multi-dimensional optimization technique.

4.3 OPTIMIZATION METHOD

Particle Swarm Optimization (PSO) is adopted in this study to calibrate the best setting of the parameters of the model that matches the real building structure. The algorithm works by initializing a population of candidate particles, which move in the search space to minimize the objective function. Each particle will update itself based on its own local best-known position as well as the global best-known position found by the entire group. PSO is selected due to its convenience in implementation, the fewer number of hyperparameters, and the capability of dealing with high dimensional optimization problems. As a gradient-free algorithm, PSO does not require the objective function surface to be differentiable and is suitable in this study, given that the objective function measures the discrepancy between recorded response and analytical response.

As shown in Eq. 4-5, the velocity of particle *I* at dimension *d* at the k^{th} step (i.e., v_{id}^{k}) is updated by three terms. The first term represents the velocity of particle *I* at the previous step factored by w^k, where *w* (Eq. 4-7) decreases linearly as the algorithm carries on with index *k* (*K* is the total number of steps). The second term in Eq. 4-5 guides the particle's position (i.e., x_{id}^{k}) towards the local best position (i.e., x_{id}^{p-best}). The third term in Eq. 4-5 guides the particle towards the global best position (i.e., x_{d}^{g-best}), which is not a function of *i*. c_1 and c_2 are the hyperparameters that can be tuned as learning rates, and r_1 and r_2 are random variables ranging from 0 to 1 in order to increase uncertainty in the searching process. Finally, the position is updated by summing up the previous position and the velocity, as shown in Eq. 4-6.

$$v_{id}^{k} = w^k v_{id}^{k-1} + c_1 r_1\left(x_{id}^{p-best} - x_{id}^{k-1}\right) + c_2 r_2\left(x_{d}^{g-best} - x_{id}^{k-1}\right) \qquad \text{Eq. (4-5)}$$

$$x_{id}^{k} = x_{id}^{k-1} + v_{id}^{k-1} \qquad \text{Eq. (4-6)}$$

$$w^k = w_{max} - (w_{max} - w_{min})\frac{k}{K} \qquad \text{Eq. (4-7)}$$

In PSO, the objective function is minimized, and the set of parameters corresponds to the minimum objective function is selected as the optimal parameters. In this study, the objective function is the measure of discrepancy between recorded acceleration response and simulated acceleration response in the time domain, as shown in Eq. 4-8, where $\boldsymbol{\theta}$ stands for the setting of parameters. The discrepancy is summed over all strong motion data points along with time history and overall sensor locations where the recorded response is measured. Acceleration instead of displacement is picked as the response where the error is computed due to the rich information contained in acceleration data and its stationarity compared to displacement time history.

$$J(\boldsymbol{\theta}) = \sum_{j=1}^{N_{sen}} \sum_{l=1}^{\tau} \frac{[\ddot{u}_j(l\Delta t) - \hat{\ddot{u}}_j(l\Delta t)]^2}{\sum_{p=1}^{\tau}[\ddot{u}_j(p\Delta t)]^2} \qquad \text{Eq. (4-8)}$$

4.4 SELECTED BUILDING CASES

Seven steel moment-resisting frame (SMRF) buildings, four reinforced concrete moment-resisting frame (RCMRF) buildings and five reinforced concrete walls (RCW) from the CSMIP database are analyzed and investigated in this study. These buildings are selected based on the inclusion criteria given below, and based on the inclusion criteria, the information of the selected buildings is listed in Table 4-1.

1) The selected buildings are symmetric in plan so that the 2-Dimensional generic frame is representative of the real building frame. Buildings with any types of irregularity is excluded from the analysis.

2) The selected buildings have at least three stories so that the period ratio T_i / T_1 could be estimated. That requires the recorded data to be less noisy and the first three clean mode shapes can be estimated.

3) The selected buildings have sensors instrumented on the ground level so that the input ground motion excitation is accessible.

4) The selected buildings have at least five ground motion records so that the effect of the ground motion intensity measures can be studied. That also requires ground motion intensity must be in a wide range that covers both benign and strong motions.

5) The direction which has sensors located at the middle of the frame is taken, so that the torsional effect will be eliminated.

6) The database has a few high-rises but a large number of low rises. To avoid bias in the statistical model, the selected buildings are evenly distributed in terms of building height.

Table 4-1. Information about Selected Buildings

CSMIP ID	Type of Building	Number of Stories	Height(ft)	Dimension in both directions(ft)	Number of GMs
23481	SMRF	7	103.75	140 / 93	10
23516	SMRF	3	41.35	144 / 132	20
24288	SMRF	32	337.9	123.5 / 89	16
24370	SMRF	6	82.5	120 / 120	16
24629	SMRF	54	735.5	196 / 121	14
57357	SMRF	13	186	167 / 167	12
58506	SMRF	3	46.20	165 / 80	16
12493	RCMRF	5	80	180 / 106.5	12
24386	RCMRF	7	65.7	160 / 60.3	16
24464	RCMRF	20	176.4	183.5 / 96	8
57355	RCMRF	12	141	190 / 96	14
13589	RCW	11	147	147 / 88	8
23285	RCW	6	80	204.6 / 136.5	38
25339	RCW	12	113.4	155 / 61.7	18
58479	RCW	6	78	182 / 67	8
58483	RCW	24	219	211 / 78	28

4.5 OPTIMIZED TIME HISTORY RESULTS

Before analyzing the recorded time history data, the signal, especially the acceleration data needs to be denoised. Discrete wavelet transformation is used to decompose the original signals. As shown in Eq.4-9, a dyadic wavelet (with base equals 2) transformation operates on the original signal f(t) is equivalent to applying filters on the signal, and by applying the low pass filter and the high pass filter, the original signal is averaged and differenced, respectively, as illustrated in Figure 4-3. In this study, db4 wavelet is used and each signal is decomposed to a level where the time interval between each data point is larger than 0.08 sec, given the original signal can have the interval from 0.005 sec (sample frequency = 200) to 0.02 sec (sample frequency = 50). The final averaged signal is the smoothed and denoised signal that will be analyzed and used with optimization techniques to obtain the best estimate of the model parameters.

$$Wf(u,2^j) = \int f(t)\frac{1}{\sqrt{2^j}}\phi(\frac{t-u}{2^j})dt \quad \text{Eq. (4-9)}$$

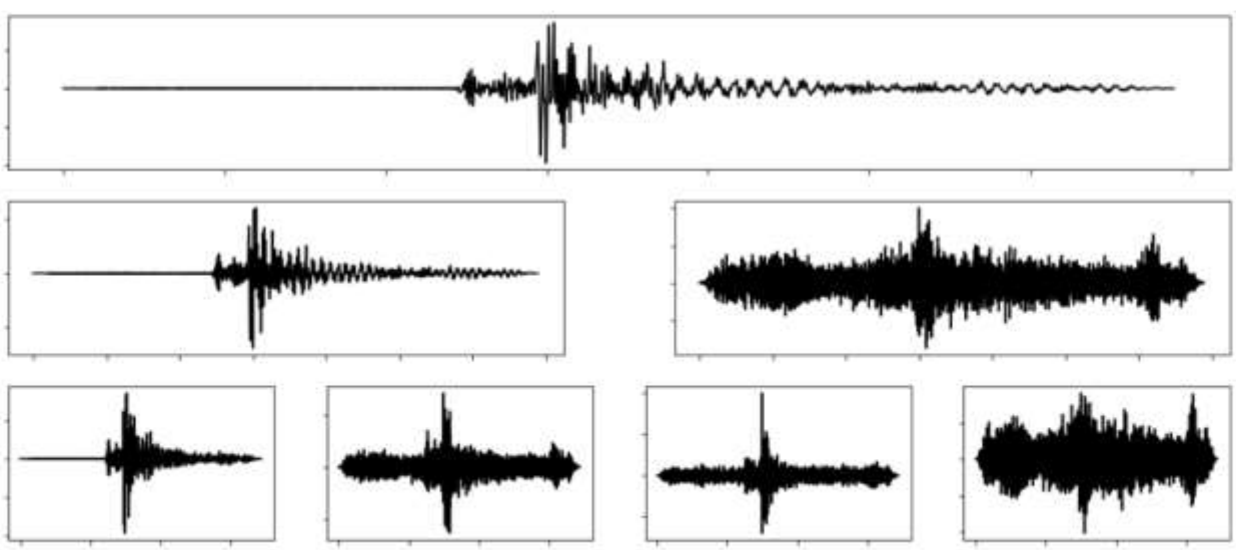

Figure 4-3. The process of wavelet averaging and differencing

To show the optimization technique results, two tallest buildings (CSMIP ID 24629, 54-story SMRF building, and CSMIP ID 24288, 32-story SMRF building) are selected as two examples to show the goodness of fitting between reconstructed response and the recorded response. The two buildings' response to the largest ground motion excitation (Northridge and Chino Hills, respectively) are plotted in Figures 4-4 and 4-5. The analytical response of the 54-story building matches the recorded response very well at the 20th, 36th and penthouse floor, although the analytical model cannot capture several peaks during 40-60 sec. At the ground floor and the 46th floor, the general trend is detected well by the analytical model, while some peaks during 25-20 sec are missing. Overall, considering the limitation of the analytical model and the rather small number of parameters utilized for the model's characterization, the reconstructed response is in acceptable agreement with the recorded one. For the 32-story building response, the reconstructed response is in high accordance with the recorded response, especially at the 8th, 16th and the roof level. At the 25th floor, the reconstructed response has a slight underestimate of the acceleration amplitude during 28-32 sec.

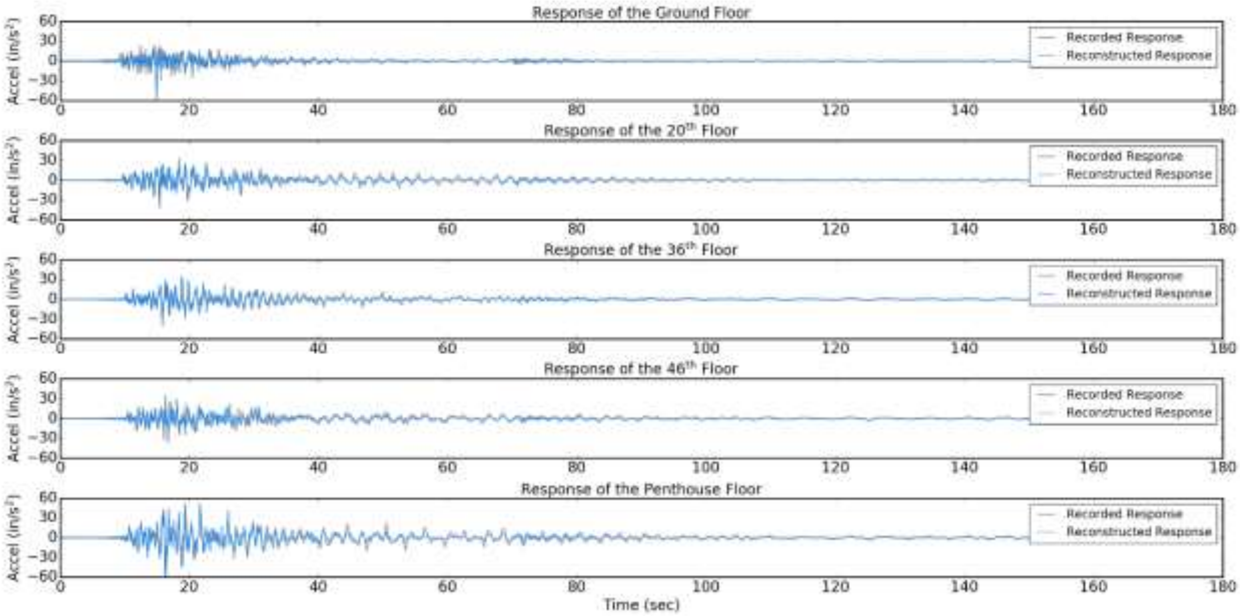

Figure 4-4. Response of the 54-story Building (CSMIP ID 24629) subject to Northridge Earthquake, January 1994.

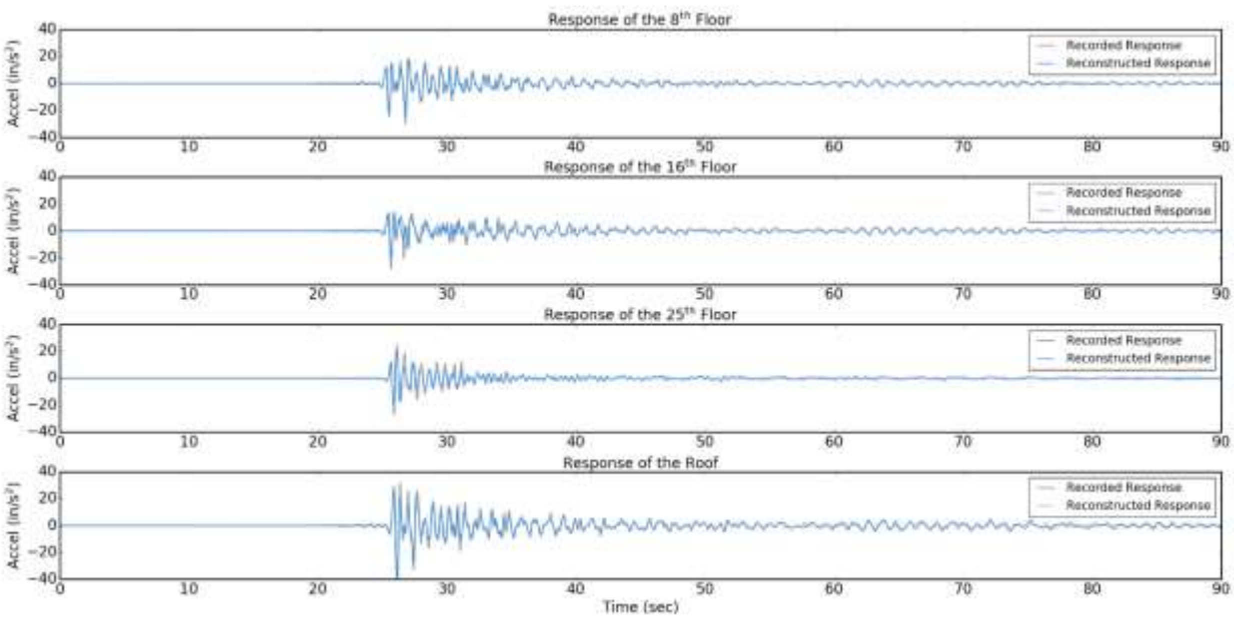

Figure 4-5. Response of the 32-story Building (CSMIP ID 24288) subject to Chino Hills Earthquake, July 2008.

4.6 STATISTICAL ANALYSIS

The data points obtained from the time history optimization are highly correlated since more than 5 ground motion records correspond to the same building structure. In other words, by carrying out the traditional linear regression, the underlying assumption of independent events is violated. To consider the correlation between records under the same building and the prediction (i.e., the estimation of the mean value) of building models parameters, the hierarchical mixed effect model is carried out in this study. The hierarchical model explains the predicted value using fixed effect and random effect in multi-level modeling. It can be expressed in a functional form shown in Equation 4-10, where y_{ij} represents any target: estimated viscous damping coefficient and estimated stiffness of the frictional damper, the function f is the fixed effect estimation given building height, dimension, ground motion intensity measures such as peak ground acceleration (PGA), peak ground velocity (PGV) and peak ground displacement (PGD) as well as the building material. The random effects of the i^{th} building, namely η_i represents inter-event variation, and ε_{ij} represents the intra-event variation of the j^{th} recording from the i^{th} building. For each target, the components of η_i and ε_{ij} are assumed to be normally distributed with zero means and variances τ^2 and σ^2, respectively.

$$\ln y_{ij} = f(H, Dim, GMIM, mat) + \eta_i + \varepsilon_{ij} \qquad \text{Eq. (4-10)}$$

Given the equation, mixed effect analysis is conducted for the database of the selected buildings with 254 ground motions in total. In this study, ground motion intensity measures, as well as building height, building dimension of the frame are selected as candidates of the predictors, while the normalized viscous damping coefficient c/m and the square root of normalized frictional damper stiffness $\sqrt{K_e/m}$ are selected as the targets to be predicted. It should be noted that the damping coefficient and the stiffness are normalized by the mass of the floor so that the values of these parameters being suggested to engineers during seismic design procedures can be related to the story mass in order to accurately model the energy dissipation mechanism of building structures. The square root of the stiffness is used to keep the units of the two targets consistent such that they are both 1/sec. After the statistical analysis is carried out to predict these parameters using different combinations of predictors, the best statistical model is suggested.

On the other hand, the predictors are adjusted to better explain the variance of the targets: 1) building height is always kept in the model as it is the most crucial indicator of the targets; 2) instead of simply including the dimension of the frame into the model, two other predictors are introduced: the floor area of the building (Dim in x-direction multiply by Dim in y-direction) and the total length of Vertical Lateral Load Resisting systems (VLLRs) of the building (for moment frames, it equals the total length of the frame, while for shear walls, it equals the total length of the wall). In total, 3 cases are considered: only include the floor area, only include the side area, and include both predictors. Although arguably, the inclusion of both predictors may introduce collinearity to the model, it is still not desirable to decompose the model into height and dimension, because the floor area, as a multiplication of two variables, introduces nonlinearity into the statistical model, and the total length of VLLRs is a more accurate indicator of building stiffness rather than the dimension. 3) PGA, PGV and PGD are analyzed in all possible models, and the one results in a model with the smallest Akaike Information Criterion (AIC), Bayesian Information Criterion (BIC), and the largest coefficient of determination (R^2) will be picked. 4) the building material (the type of building) is treated as a categorical variable and dummy variables are created from the One-Hot encoding. RCMRF is treated as the base case because it is made of concrete (correlated with RCW) and it belongs to moment frames (correlated with SMRF). Table 4-2 summarizes 9 models for viscous damping coefficient c/m and Table 4-3 summarizes 9 models for the square root of normalized frictional damper stiffness $\sqrt{K_e/m}$.

Table 4-2. Statistical model selection for viscous damping coefficient c/m

	GMIM	VLLR length	Floor Area	AIC	BIC	R^2
Model 1	PGA	Included	Excluded	190.1	218.6	0.639
Model 2	PGV	Included	Excluded	196.2	224.7	0.630
Model 3	PGD	Included	Excluded	196.3	224.8	0.631
Model 4	PGA	Excluded	Included	192.9	221.5	0.640
Model 5	PGV	Excluded	Included	198.9	227.4	0.631
Model 6	PGD	Excluded	Included	198.7	227.3	0.632
Model 7	PGA	Included	Included	188.3	220.4	0.638
Model 8	PGV	Included	Included	194.3	226.4	0.629
Model 9	PGD	Included	Included	194.3	226.4	0.630

Table 4-3. Statistical model selection for stiffness of frictional damper $\sqrt{K_e/m}$

	GMIM	VLLR length	Floor Area	AIC	BIC	R^2
Model 1	PGA	Included	Excluded	38.4	66.9	0.802
Model 2	PGV	Included	Excluded	42.2	70.7	0.798
Model 3	PGD	Included	Excluded	41.5	70.0	0.799
Model 4	PGA	Excluded	Included	-7.1	21.4	0.770
Model 5	PGV	Excluded	Included	-3.5	25.0	0.767
Model 6	PGD	Excluded	Included	-5.0	23.5	0.768
Model 7	PGA	Included	Included	-11.3	20.8	0.775
Model 8	PGV	Included	Included	-8.0	24.1	0.772
Model 9	PGD	Included	Included	-9.1	23.1	0.773

By investigating the difference GMIMs, it can be observed that the model with PGA has smaller AIC, BIC and lager R^2 in all models compared to the model with PGV and PGD. Therefore, for both targets, PGA is selected as the GMIM, and only Model 1, Model 4 and Model 7 are further studied. For the viscous damping coefficient c/m, Model 1 and Model 7 both have much better AIC and BIC compared to Model 4. After Model 4 is ruled out, although Model 1 has a slightly larger AIC than Model 7, it has better performance in both BIC and R^2. Therefore, Model 1 is picked for estimating c/m. This is following the traditional treatment of viscous damping coefficient because Model 1 indicates that the viscous damper is highly correlated with the total length of VLLRs, which is representative of the dependency of viscous damping on building stiffness. For the square root of normalized frictional damper stiffness $\sqrt{K_e/m}$, Model 4 and Model 7 both have much better AIC and BIC compared to Model 1. After Model 1 is ruled out, Model 4 shows significantly better performance in AIC compared to BIC, along with a slightly larger BIC and the difference in R^2 is negligible. Therefore, Model 4 is picked for estimating $\sqrt{K_e/m}$. This is also as expected since the properties of the frictional damper depend on the non-structural elements, including partition walls and suspended ceilings which are highly dependent on the floor area rather than the load resisting systems. To verify the models for two targets, detailed statistics of the models are presented in Table 4-4 and 4-5.

Table 4-4. Final statistical model for the viscous damping coefficient c/m

	Interception	PGA	Height	VLLRs	SMRF	RCW
Estimate	3.376	-0.047	-0.277	0.181	-0.267	0.041
Lower Est	2.237	-0.083	-0.402	0	-0.494	-0.202
Upper Est	4.516	-0.010	-0.153	0.363	-0.388	0.283
p-Value	0	0.011	0	0.049	0.022	0.743
τ^2	0.229^2					
Lower τ^2	0.171^2					
Upper τ^2	0.307^2					
σ^2	0.305^2					
Lower σ^2	0.278^2					
Upper σ^2	0.333^2					

Table 4-5. Final statistical model for the stiffness of the frictional damper $\sqrt{K_e/m}$

	Interception	PGA	Height	Floor Area	SMRF	RCW
Estimate	8.846	-0.026	-0.074	-0.636	0.662	-0.112
Lower Est	8.052	-0.052	-0.114	-0.717	0.582	-0.192

Upper Est	9.639	0	-0.034	-0.554	0.741	-0.031
p-Value	0	0.058	0	0	0	0.007
τ^2	0					
Lower τ^2	0					
Upper τ^2	0					
σ^2	0.232^2					
Lower σ^2	0.213^2					
Upper σ^2	0.252^2					

Table 4-4 provides the following information about the statistical model of the viscous damper in terms of both fixed effect and random effect: 1) the effect of PGA, building height and length of VLLRs are statistically significant. The increment of PGA and building height result in the decrease of viscous damping. 2) SMRFs have smaller viscous damping compared to RCMRFs, which are also moment frames but made of reinforced concrete. The difference between RCMRFs and RCWs are not significant. 3) the inter-event variability is slightly less than the intra-event variability. Similarly, Table 4-5 provides the following information about the statistical model of the frictional damper: 1) the effect of PGA, building height and floor area are statistically significant, and all predictors are negatively correlated with the stiffness of the damper. 2) SMRFs, RCMRFs, and RCWs have 3 distinct levels of predicted stiffness: SMRFs have the largest stiffness and RCWs have the smallest stiffness. 3) the inter-event variability is negligible, indicating that the inter-event random effect can be ignored, and all buildings can be treated as independent events. Figure 4-6 to figure 4-11 show the formula of the prediction for viscous damping coefficient c/m and stiffness of frictional damper $\sqrt{K_e/m}$ versus building height, PGA, VLLR length and floor area. Circles, squares, and diamonds stand for SMRF buildings, RCW buildings and RCMRF buildings, respectively. Red lines and blue lines stand for the steel formula (for SMRFs) and the concrete formula (for RCWs and RCMRFs), respectively, with the solid lines representing the mean prediction and the dashed lines representing 95% confidence intervals.

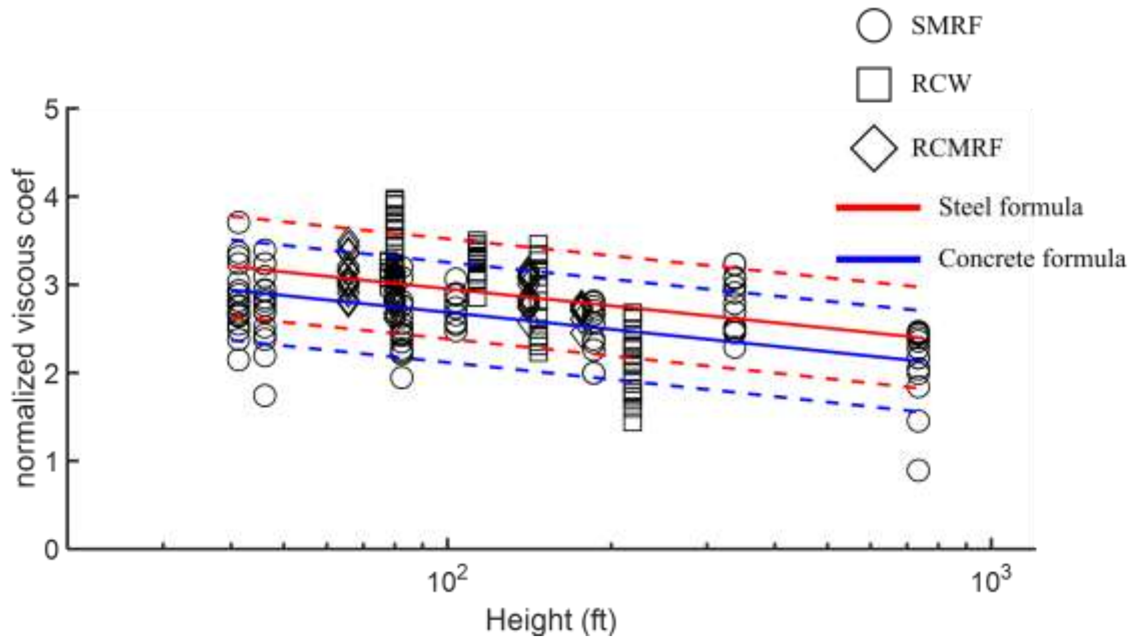

Figure 4-6. Viscous damping coefficient vs. Building height

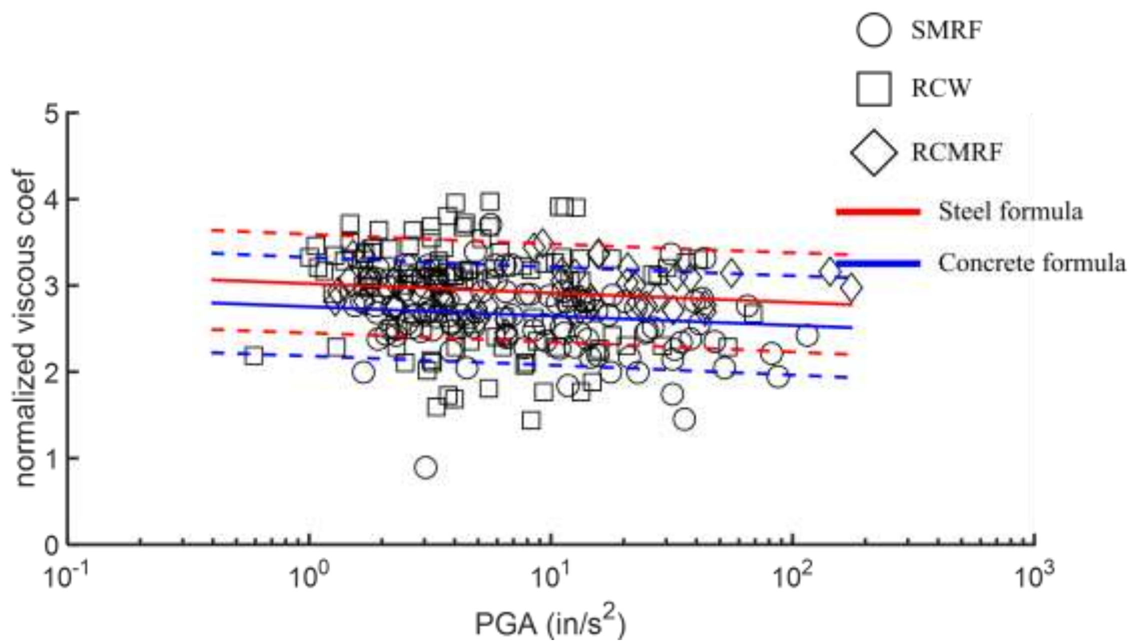

Figure 4-7. Viscous damping coefficient vs. PGA

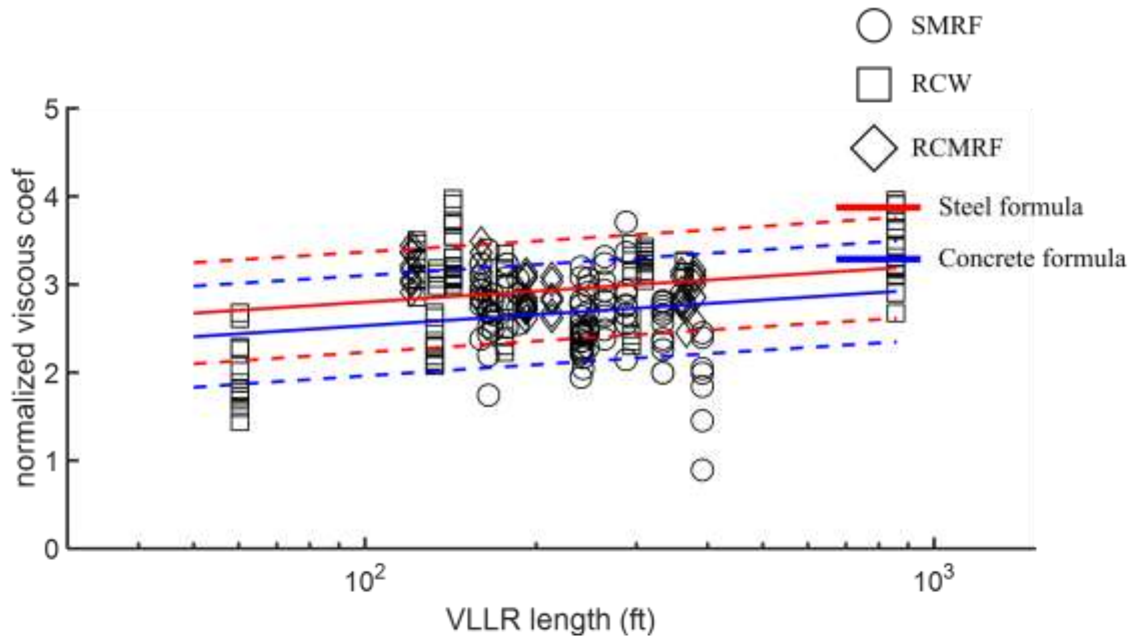

Figure 4-8. Viscous damping coefficient vs. Total length of VLLRs

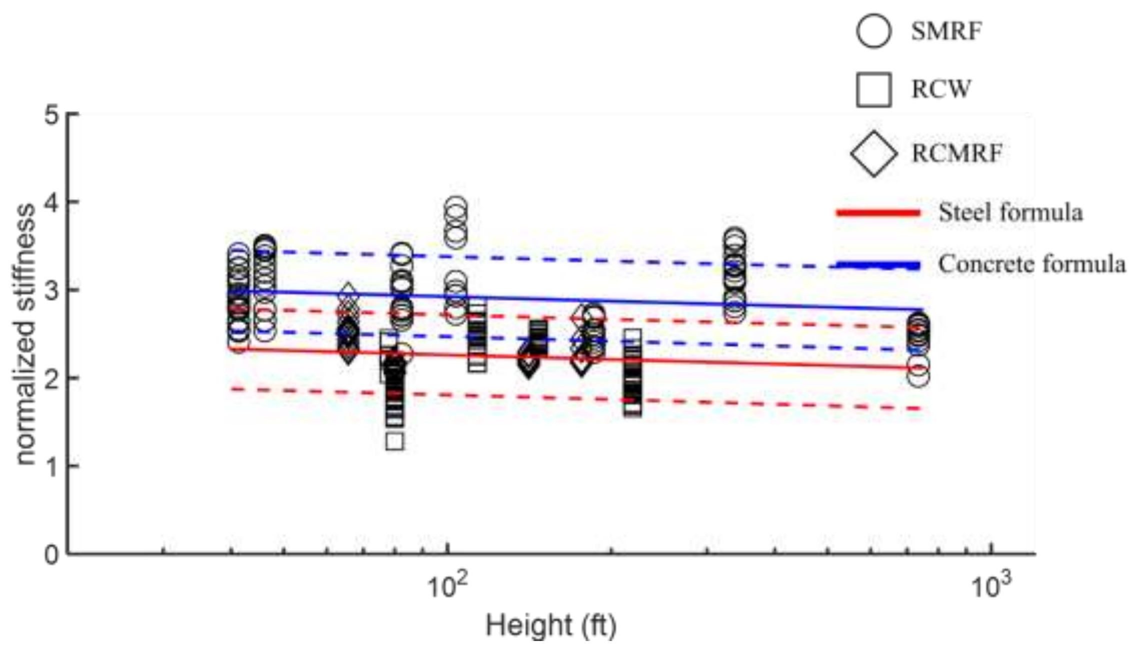

Figure 4-9. Stiffness of the frictional damper vs. Building height

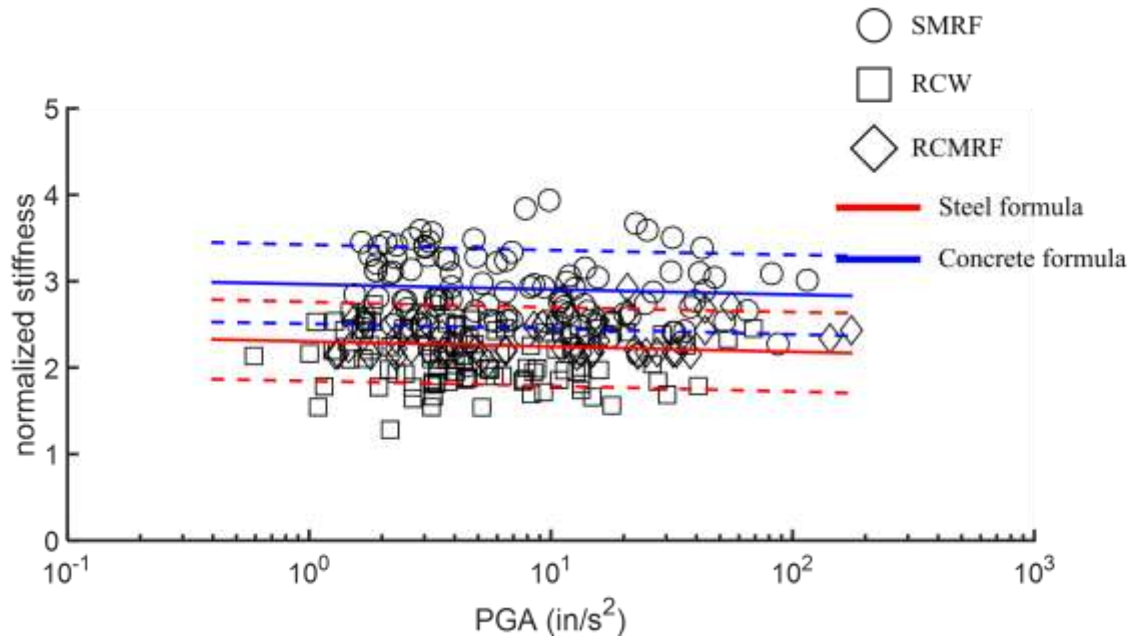

Figure 4-10. Stiffness of the frictional damper vs. PGA

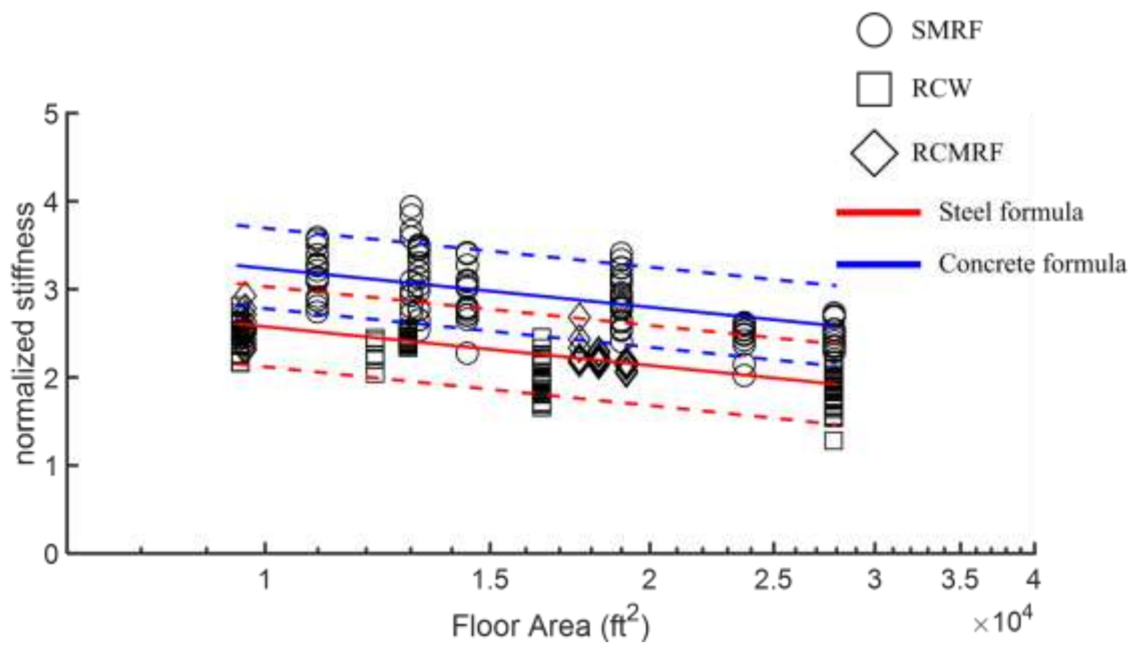

Figure 4-11. Stiffness of the frictional damper vs. Floor Area

4.7 VERIFICATION OF THE MODEL

The properties of the damping element can be computed from the mixed effect model. The model is trained from a large database with multiple buildings along with multiple ground motion excitations. However, a validation model is required to test the performance of the building structure with the implementation of the damping element computed from the statistical model. In this study, a model of UCI 8-story engineering tower is used for verification purposes. From the 3rd floor to the roof, the building comprises steel frames; therefore, a 6-story steel building mode is built in Etabs and the response at the 3rd floor is treated as the input to the system. The properties of the damping element are calculated using the steel mixed effect model equation. Links with the corresponding stiffness and the viscous damping coefficient is built between every two adjacent floors on the exterior steel frame.

Four different damping models are investigated in this verification study: 5% Rayleigh damping, 2.5% Rayleigh damping, 1% Rayleigh damping, and the damping element model. The response of the building subject to 12 distinct ground motions excitations is analyzed. For a combination of each damping model and each ground motion, the maximum displacement response from the most critical floor is compared to that of the recorded response, and the distribution of the displacement ratio is the metric used to measure the goodness of the damping element model. As shown in Figure 4-12, 5% and 2.5% Rayleigh damping models both yield biased estimations of displacement that are much smaller than the recorded displacement. The distributions of 1% Rayleigh damping model and the damping element model have comparable means and standard deviations, however, as the ratio ranging from 0 to infinite should be lognormally distributed, the damping element is superb to 1% damping model in terms of capturing a more practical distribution of displacement ratios subject to multiple ground motions.

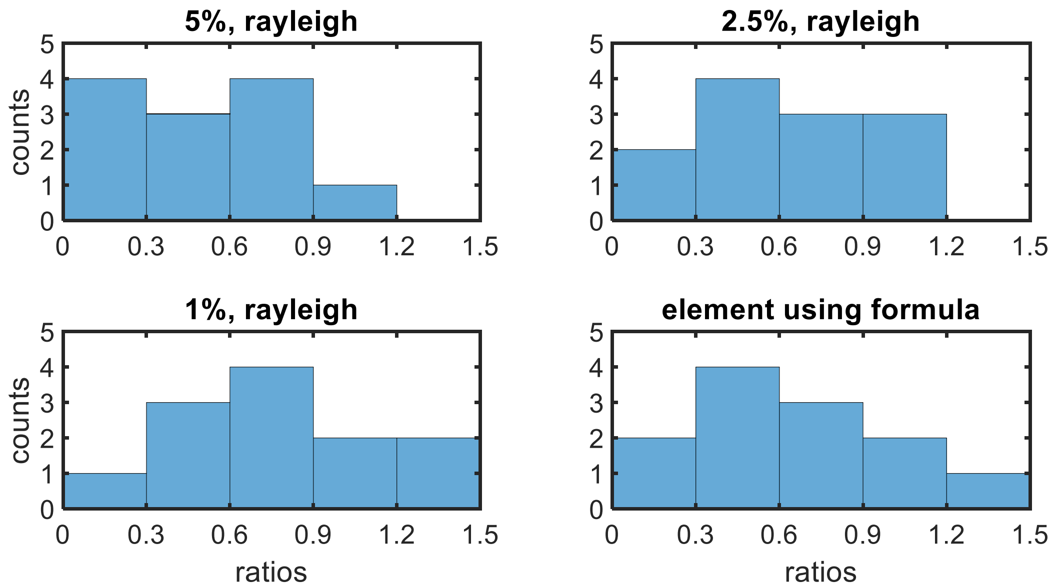

Figure 4-12. The distribution of the maximum displacement ratio for different damping models

4.8 CONCLUSION AND FURTHER STUDY

A damping element model is modified from the widely used continuum model. The model can simulate three energy dissipation sources, including linear viscous damping and displacement dependent frictional damping. More than 200 records are investigated in this study, each with PSO is utilized to identify key parameters of the damping element, including the normalized viscous damping coefficient c/m and the square root of the normalized frictional damper stiffness K_e/m. Mixed effect models are proposed to predict these targets given building information such as height, VLLR length, floor area, PGA and type of building structures.

As this study uses a relatively small dataset of buildings, the next step is to apply the damping element model and model updating technique to capture different energy dissipation mechanisms from a larger dataset. The data from the sixty-five buildings (400 distinct seismic events in total) from the California Strong Motion Instrumentation Program (CSMIP) database, is a natural starting point. It includes Steel Moment Resisting frames, Reinforced Concrete Moment Resisting frames and Reinforced Concrete Walls (i.e., SMRF, RCMRF, and RCW). A statistical model of the structural parameters will then be built according to ground motion excitation records for every single building and all ground motion records in the database. The study aims to develop a rational estimation of building energy dissipation based on building type, building height, building dimension, and ground motion intensity.

4.9 ACKNOWLEDGEMENT

I would like to show my gratitude to Dr. Omid Esmaili for sharing the Etabs model of UCI 8-story engineering tower for verification of the research.

4.10 REFERENCES

American Society of Civil Engineers (ASCE) (2017). Minimum Design Loads for Buildings and Other Structures (ASCE/SEI 7-17). Reston, VA: American Society of Civil Engineers.

Bernal, D., Kojidi, S., Kwan, K., Döhler, M. (2012). Damping Identification in Buildings from Earthquake Records. SMIP12 Seminar Proceedings, 2012.

Cruz, C., Miranda, E., 2016. Evaluations of damping ratios for the seismic analysis of tall buildings. ASCE Journal of Structural Engineering, 143(1).

Ebrahimian, H., Astroza, R., Conte, J.P.,de Callafon, R.A.(2017), Nonlinear Finite Element Model Updating for Damage Identification of Civil Structures using Batch Bayesian Estimation. Mechanical Systems and Signal Processing 84, 194-222.

Federal Emergency Management Agency (FEMA) (2012). Seismic performance assessment of buildings volume 1 – Methodology. Technical Report P-58-1, December. Washington, DC: FEMA.

Fritz, W. P, Jones, N.P., & Igusa, T., 2009. Predictive models for the median and variability of building period and damping. Journal of Structural Engineering, 135(5), 576-586.

Jeary, A. P. (1997). Damping in structures. Journal of Wind Engineering and Industrial Aerodynamics, 72: 345 – 355.

Lagaros, N.D., Papadrakakis, M., Kokossalakis, G. (2002), Structural Optimization using Evolutionary Algorithms. Computers and Structures, 80, 571-589.

LATBSDC (2018). An Alternative Procedure for Seismic Analysis and Design of Tall Buildings. Los Angeles: CA. Los Angeles Tall Buildings Structural Design Council.

McKenna, F., Scott, M. H., and Fenves, G. L. (2010), Nonlinear Finite Element Analysis Software Architecture using Object Composition. Journal of Computing in Civil Engineering, 24(3), 95-107.

Miranda, E., Taghavi, S. (2005). Approximate floor acceleration demands in multi-story buildings. I: Formulation. Journal of Structural Engineering, 131(2), 203-211.

Nasrellah, H.A., Manohar, C.S. (2011), Finite Element Method Based Monte Carlo Filters for Structural System Identification. Probabilistic Engineering Mechanics, 26, 294-307.

PEER (2017). Guidelines for performance-based seismic design of tall buildings (Version 2). PEER Report 2017/06, Berkeley, CA: TBI Guidelines Working Group.

Perez, R.E., Behdinan, K. (2007), Particle Swarm Approach for Structural Design Optimization. Computers and Structures, 85, 1579-1588.

Satake, N., Suda, K. I., Arakawa, T., Sasaki, A., & Tamura, Y., 2003. Damping evaluation using full-scale data of buildings in Japan. Journal of structural engineering, 129(4), 470-477.

Song, W., Dyke, S. (2014), Real-time Dynamic Model Updating of a Hysteretic Structural System. Journal of Structural Engineering, 140(3), 04013082.

Spence, S., Kareem, A. (2014). Tall Buildings and Damping: A Concept-Based Data-Driven Model. Journal of Structural Engineering, 140(5): 04014005.

Tamura, Y., & Yoshida, A. (2008). Amplitude dependency of damping in buildings. In Proceedings of the 18th Analysis and Computation Speciality Conference. Vancourver, BC, Canada, April 24-26, 2008.

Wyatt, T. A. (1977). Mechanisms of damping. In Proceeding of a Symposium of Dynamic Behavior of Bridges at the Transport and Road Research Laboratory, Crowthorne, Berkshire, England, May 19, 1977.

CHAPTER 5: CONCLUSION, LIMITATION AND FUTURE WORK

This dissertation's main goal is to develop a holistic damping element model to capture and represent the energy dissipation mechanisms in structures. The suggested damping element model is capable of modeling material damping (in the form of linear viscous damping), Coulomb friction between structural members, and the breakage of the members in the form of frictional damping. The effect of viscous damping and frictional damping is investigated through the element properties such as the linear viscous coefficient, the initial stiffness of the frictional damper and the yielding deformation of the frictional damper, as well as the energy dissipated through the dampers calculated from the area under the force-deformation curve throughout the time history. It was found that the ratio of energy dissipated by the viscous damper to the energy dissipated by the frictional damper decreases with the increase of ground motion intensity measures, which indicated that the percentage of energy dissipated by a frictional damper is higher at the beginning of seismic excitation. On the other hand, normalized element properties decrease with the increase of building scale, quantified by building height and dimension.

This dissertation arguably has certain limitations in terms of data sample size and the modeling technique. First, the sample size of the buildings in the database with regard to building type, building height, number of seismic events is skewed. More RCWs, SMRFs and RCMRFs are included in the database compared to other building types such as CBFs, EBFs and Wood Frame buildings, etc. Most buildings are of 3 to 6 stories, and the number of buildings taller than 20-story is especially limited. There is also an imbalance in the number of seismic events per building, given that the recorded seismic responses of most buildings are fewer than 10 and most seismic events are extremely benign as the spectral acceleration is less than 0.05g. The issue of lacking intense seismic events may lead to trivial optimal solutions and inaccuracy in the estimation of damping element properties, as nonlinear parameters such as the yielding deformation of the frictional damper can be insensitive to the seismic intensity in a low region and unidentifiable regardless of the optimization algorithm because the value will not be updated during the global search of the optimal results.

Second, to tailor to the real-life building structure with distinct construction materials and lateral force resisting systems, it requires the finite element building model to be as general as possible. As a trade-off, the accuracy of the building model is sacrificed, in other words, structural elements such as beams, columns, slabs are not physically modeled. Instead, a more conceptual and generic model incorporating both shear and flexural behavior of the buildings is adopted. Assumptions need to be made when generating the generic building model; for example, floor masses are lumped at each story and proportional to the size of the floor plan, the building is represented by two orthogonal frames with a fixed bay length, the damping element properties are kept as a constant value along with the building height, the generic model is linear by nature and the only nonlinearity is imposed through the frictional damper which utilizes the plastic-perfectly-elastic material, etc.

Based on the limitation of this dissertation, future work is suggested as the following:

1. Using a more exhaustive database that explores more CBFs, EBFs and Wood-Frames buildings guarantees that the results are not skewed towards RCWs and SMRFs. More intense seismic events are needed to have the data gathered in a zone of high-intensity measures.
2. Using a more sophisticated model which includes hysteretic materials to represent nonlinearity experienced in structural elements.

3. Soil-structure interaction should be studied by the modeling of soil material using springs and damper to capture the transfer function between free-field motion and foundation input motion. This could be helpful to directly implement radiation damping.
4. Three-dimensional modeling of building structures could be carried out to replace the modeling of two-dimensional frames.
5. A more comprehensive clustering method needs to be adopted to statistically assess the results obtained from building structures of different construction materials or different building types and provide more accurate predictions for designers.
6. Utilizing nonlinear time history recorded data with signal processing, system identification, optimization technique and other mathematical tools can be further explored. The characterization of energy dissipation mechanisms can be extended to a 3-dimensional building structure with torsional damping, as well as bridge structures with dampers that are physically modeled.